

High-Density Discrete Passive EMI Filter Design for Dc-Fed Motor Drives

Yoann Y. Maillet

Thesis submitted to the Faculty of the
Virginia Polytechnic Institute and State University
in partial fulfillment of the requirements for the degree of

Master of Science
In
Electrical Engineering

Fred Wang, Chairman
Dushan Boroyevich
Shuo Wang

August 29, 2008
Blacksburg, Virginia

Keywords: Electromagnetic Interference (EMI), Motor Drive

High-Density Discrete Passive EMI Filter Design for Dc-Fed Motor Drives

Yoann Y. Maillet

ABSTRACT

This work systematically presents various strategies to reduce both differential mode (DM) and common mode (CM) noise using a passive filter in a dc-fed motor drive. Following a standard approach a baseline filter is first designed to be used as reference to understand and compare the available filter topologies. Furthermore, it is used to analyze the grounding scheme of EMI filter and more specifically provide guidelines to ground single or multi stages filter. Finally, the baseline filter is investigated to recognize the possible solutions to minimize the size of the whole filter. It turns out that the CM choke and DM capacitors are the two main downsides to achieve a small EMI filter. Therefore, ideas are proposed to improve the CM choke by using other type of material such as nano crystalline core, different winding technique and new integrated method. A material comparison study is made between the common ferrite core and the nano crystalline core. Its advantages (high permeability and saturation flux density) and drawback (huge permeability drop) are analyzed through multitudes of small and large signals tests. A novel integrated filter structure is addressed that maximizes the window area of the ferrite core and increases its leakage inductance by integrating both CM and DM inductances on the same core. Small- and large-signal experiments are conducted to verify the validity of the structure showing an effective size reduction and a good improvement at low and high frequencies. To conclude, a final filter version is proposed that reduce the volume of the baseline filter by three improve the performances in power tests.

To the people I love the most,

My parents Nicole and Jean-Jacques

My sisters Leatitia, Valerie and Marion

My girlfriend Marie-Anne

Acknowledgments¹

I would like first of all to thank my advisor Dr. *Fred Wang*, who encouraged and gave me the opportunity to work for the Center for Power Electronics (CPES) for the past two years. I know it was a tough decision to take this French student coming directly from undergrad and place him on a project. It was a real challenge and I tried to do my best to fulfill the expectation you placed on me.

I would like also to recognize Dr. *Dushan Boroyevich*, who supervised me during my master's thesis, assisted me when I had questions, and lastly pretended to be me and presented during my first conference.

I would like to give my sincere gratitude to Dr. *Shuo Wang*, who helped me so much and spent so much time explaining me many aspects of EMI. It was a real pleasure to learn and work with him in this area.

I cannot forget Dr. *Rolando Burgos*, who supported me and continuously gave me advice. He spent a lot of time correcting and arranging my papers and helped me improve my writing skills.

I would like also to express my gratitude to the Group SAFRAN and Hispano-Suiza who supported the project on which I worked for two years, and especially Mr. *Régis Meuret*, Mr. *Nicolas Huttin*, Mr. *Alain Coutrot* and Mr. *Rémi Robutel*. It was a real pleasure to work with them.

I would also like to acknowledge the Center for Power Electronics and all the staff that make it run everyday, Mr. *Bob Martin*, Ms. *Marianne Hawthorne*, Mrs. *Trish Rose*, Mr. *Jamie Evans*, Mrs. *Theresa Shaw*, Mrs. *Linda Long*, Mr. *Dan Huff*, Ms *Beth Tranter* and Mrs. *Linda Gallagher*.

Now I would like to thank my colleagues that assisted me every day and from whom I learned a lot, not only technically but also culturally, as CPES are a group of people of a tremendous number of ethnicities. Thanks to Ms. Sara Ahmed who was an enjoyable classmate during all these years of undergrad and graduate classes and provided good

¹ This work was supported by SAFRAN Group. This work made use of ERC Shared facilities supported by the National Science Foundation under Award Number EEC-9731677.

support at CPES. Special gratitude to my friend, team member and mentor Mr. Rixin Lai who assisted during these two years and from whom I learned a lot about China. Lastly, I won't forget my other friends and colleagues Mr. *Tim Thacker*, Mr. *Fang Luo*, Mr. *Di Zang* and Mr. *Xibo Yuan*.

Finally and the most importantly, I would like to acknowledge my parents. Without them I would have never had the opportunity to leave France and had this chance to see a new culture and live this experience. I would like also to thank my girlfriend and the rest of my family for their love and continuous support over the years.

Thank you everyone,

Yoann

TABLE OF CONTENTS

CHAPTER 1 INTRODUCTION.....	1
I. Background.....	1
II. Literature Review and Motivations	3
III. Objectives & Scope of Work	6
IV. Thesis Outline and Summary of Contribution	6
CHAPTER 2 EMI ANALYSIS.....	8
I. EMI Definition and Noise Propagation.....	8
A. Common-Mode and Differential-Mode Noise Characterization.....	8
B. Noise Propagation.....	10
II. EMI Standards	11
A. Setup.....	11
B. Frequency Limit and Bandwidth	12
C. Restrictions	14
III. Experiment Setup	14
A. System characteristics	14
B. Running Conditions	17
C. Conducted EMI Noise Measurement Procedure	17
CHAPTER 3 BASELINE EMI FILTER DESIGN.....	24
I. Introduction.....	24
II. Design Procedure.....	25
III. Material Consideration for Baseline Filter.....	34
IV. Preliminary Design of CM choke.....	38
V. EMI Filter Modeling.....	41
A. Common Mode Choke.....	41
B. CM and DM Capacitor.....	46
C. Filter	48
D. Insertion Gain Comparison for Both CM & DM	50
VI. Baseline Filter Large Signal Measurement.....	51

VII. Baseline Filter Size	54
VIII. Summary	55
CHAPTER 4 FILTER TOPOLOGY AND GROUNDING CONSIDERATION	56
I. Introduction.....	56
II. Filter Topology Consideration.....	56
A. Basic Approach to Choose Filter Structure.....	56
B. Multi-Stage Filter Concerns	58
III. Grounding Effect	60
A. Ground Impedance.....	60
B. One Point vs. Multi-Point Ground for Multi-Stage Filter	65
IV. Summary.....	74
CHAPTER 5 APPROACHES TO MINIMIZING SIZE AND IMPROVING	
PERFORMANCE OF EMI FILTER	75
I. Introduction.....	75
II. CM Choke Core Material.....	75
III. CM Choke Parameters	81
A. Key Relations between CM Choke Parameters' Designs	81
B. Parameters Calculation and Concerns.....	82
C. Parameters Effect on Small and Large Signals Measurements	87
IV. Integrated CM and DM Inductor.....	97
A. Structure Analysis.....	98
B. Measurements Verification.....	101
C. Conclusion.....	105
V. Capacitor Impact on Size and Performance	105
VI. Final Design Approach and Latest Filter Version.....	109
CHAPTER 6 SUMMARY AND CONCLUSIONS	114
REFERENCES.....	115

LIST OF FIGURES

Fig. 1-1: Emissions and susceptibility tests for both conducted and radiated noise	2
Fig. 1-2: Power train of the complete system under analysis	3
Fig. 1-3: Conventional adjustable speed drive system	5
Fig. 2-1: CM and DM noise distribution	8
Fig. 2-2: CM and DM equivalent noise path with LISN	9
Fig. 2-3: Experiment setup of the Military Standard 461E	11
Fig. 2-4: LISN circuit characteristics	12
Fig. 2-5: EMI standard on voltage	13
Fig. 2-6: Experiment setup	15
Fig. 2-7: Measured impedance of LISN	15
Fig. 2-8: Impedance of LISN from Military Standard 461 E	16
Fig. 2-9: MD used for experiment.....	17
Fig. 2-10: Load used for experiment	17
Fig. 2-11: LISN equivalent circuit for noise and line frequency	18
Fig. 2-12: Correction factor for LISN capacitor	19
Fig. 2-13: Voltage measurement procedure.....	19
Fig. 2-14 CM (left) and DM (right) noise measurement with current probe.....	20
Fig. 2-15: Current measurement procedure	20
Fig. 2-16: Current probe transfer impedance.....	21
Fig. 2-17: CM noise measurement with noise separator and current probe	23
Fig. 2-18: DM noise measurement with noise separator and current probe.....	23
Fig. 3-1: Baseline EMI filter	25
Fig. 3-2: CM equivalent filter circuit	26
Fig. 3-3: DM equivalent filter circuit	26
Fig. 3-4: Equivalent circuit for the derivation of CM filter attenuation.....	27
Fig. 3-5: Common Mode noise filter theoretical attenuation	28
Fig. 3-6: Equivalent circuit for the derivation of DM filter attenuation.....	29
Fig. 3-7: Differential Mode noise filter theoretical attenuation.....	30
Fig. 3-8: Original CM noise.....	31
Fig. 3-9: Original DM noise	31

Fig. 3-10: High harmonics for the original CM noise.....	32
Fig. 3-11: High harmonics for the original DM noise.....	32
Fig. 3-12: Required CM attenuation and corner frequency.....	33
Fig. 3-13: Required DM attenuation and corner frequency.....	33
Fig. 3-14: Equivalent baseline filter.....	34
Fig. 3-15: Permeability of ferrite core.....	35
Fig. 3-16: Size representation of film (left) and ceramic (right) capacitors for CM filter	36
Fig. 3-17: Impedance of 100nF film and ceramic CM capacitor.....	36
Fig. 3-18: Phase of 100nF film and ceramic CM capacitor.....	37
Fig. 3-19: Impedance of 33 μ F electrolytic and ceramic DM capacitor	38
Fig. 3-20: Size representation of electrolytic (right) and ceramic (left) capacitors for DM filter	38
Fig. 3-21: Winding angle example.....	40
Fig. 3-22: Magnetics core size definition	40
Fig. 3-23: Equivalent circuit of CM inductor	42
Fig. 3-24: Equivalent circuit of measurement 1.....	42
Fig. 3-25: Impedance for measurement 1	43
Fig. 3-26: Equivalent circuit of measurement 2.....	44
Fig. 3-27: Impedance for measurement 2.....	44
Fig. 3-28: Equivalent circuit of measurement 3.....	45
Fig. 3-29: Impedance for measurement 3	45
Fig. 3-30: Equivalent circuit of CM inductor with parasitics value.....	46
Fig. 3-31: Equivalent model for the 100nF CM capacitor	46
Fig. 3-32: Impedance of the 100nF CM capacitor	47
Fig. 3-33: Equivalent model for the 150 μ F DM capacitor.....	47
Fig. 3-34: Impedance of the 150 μ F DM capacitor.....	48
Fig. 3-35: Insertion gain definition	49
Fig. 3-36: CM insertion gain equivalent circuit.....	49
Fig. 3-37: DM insertion gain equivalent circuit.....	50
Fig. 3-38: Simulated and measured CM insertion gain.....	50
Fig. 3-39: Simulated and measured DM insertion gain.....	51

Fig. 3-40: Large signal CM EMI noise	52
Fig. 3-41: Large signal DM EMI noise	52
Fig. 3-42: Small and large signal CM EMI noise	53
Fig. 3-43: Small and large signal DM EMI noise	54
Fig. 3-44: Baseline filter picture	54
Fig. 4-1: DM topology comparison.....	58
Fig. 4-2: Basic two stages EMI filter for the same frequency range.....	60
Fig. 4-3: One stage EMI filter “LC” type	61
Fig. 4-4: Filter interconnection with the drive	61
Fig. 4-5: Grounding impedance effect on CM noise.....	62
Fig. 4-6: Grounding impedance effect on DM noise	63
Fig. 4-7: Two points ground equivalent representation	63
Fig. 4-8: Two points ground setup	64
Fig. 4-9: Grounding impact when topology of DM filter is changed on CM noise.....	65
Fig. 4-10: Grounding impact when topology of DM filter is changed on DM noise	65
Fig. 4-11: Two stages EMI filter for separate frequency range.....	66
Fig. 4-12: Original CM equivalent model	67
Fig. 4-13: One point ground equivalent CM model.....	68
Fig. 4-14: Two point ground equivalent CM model	69
Fig. 4-15: One (top) and two (bottom) point ground CM filter used in simulation software (Saber)	70
Fig. 4-16: One and two point ground simulation results	70
Fig. 4-17: EMI filter PCP layout with one point ground.....	71
Fig. 4-18: EMI filter layout with one point ground	71
Fig. 4-19: EMI filter PCP layout with two points ground.....	71
Fig. 4-20: EMI filter layout with two point ground	72
Fig. 4-21: EMI measurement setup representation: one point ground.....	72
Fig. 4-22: EMI measurement setup representation: two point ground.....	72
Fig. 4-23: Picture of EMI measurement setup: two point ground	73
Fig. 4-24: Comparing effects of grounding methods on CM noise for a multi-stage filter	74

Fig. 4-25: Comparing effects of grounding methods on DM noise for a multi-stage filter	74
Fig. 5-1: Flux density in function of temperature for ferrite core.....	76
Fig. 5-2: Comparison between nano-crystalline and ferrite core.....	76
Fig. 5-3: CM choke representation using ferrite and nano-crystalline core	77
Fig. 5-4: Temperature (degree) dependence on permeability for nano-crystalline core ...	78
Fig. 5-5: Permeability behavior for ferrite core	78
Fig. 5-6: CM Choke inductance	79
Fig. 5-7: Leakage inductance of CM Choke	79
Fig. 5-8: CM comparison for 3 cores	80
Fig. 5-9: DM comparison for 3 cores	80
Fig. 5-10: Correlation between CM choke parameters	82
Fig. 5-11: Bifilar winding drawing	84
Fig. 5-12: CM choke using bifilar winding	84
Fig. 5-13: CM chokes comparison after multi-layers winding and higher current density	85
Fig. 5-14: Filter reduction when CM choke is improved	85
Fig. 5-15: 4 CM chokes used for experiment	88
Fig. 5-16: CM insertion gain for case 1 and 2	89
Fig. 5-17: CM noise comparison for case 1 & 4.....	90
Fig. 5-18: DM noise comparison for case 1 & 4.....	90
Fig. 5-19: EPC cancellation small signal measurement	91
Fig. 5-20: EPC cancellation large signal measurement.....	92
Fig. 5-21: Initial thermal measurement with a 6.6A line current.....	93
Fig. 5-22: Steady thermal measurement with a 6.6A line current	93
Fig. 5-23: Initial thermal measurement with a 8.3A line current.....	93
Fig. 5-24: Steady thermal measurement with a 8.3A line current	93
Fig. 5-25: Time domain representation of the CM output current (after filter) for 6.6A line current for ferrite core.....	94
Fig. 5-26: Time domain representation of the CM output current (after filter) for 6.6A line current for nano-crystalline core	94

Fig. 5-27: Time domain representation of the CM output current (after filter) for 8.3A line current for ferrite core.....	94
Fig. 5-28: Time domain representation of the CM output current (after filter) for 8.3A line current for nano-crystalline core	94
Fig. 5-29: Temperature effect on CM noise for 6.6A line current and ferrite core	95
Fig. 5-30: Temperature effect on CM noise for 8.3A line current and ferrite core	96
Fig. 5-31: Temperature effect on CM noise for 6.6A line current and nano-crystalline core	96
Fig. 5-32: Temperature effect on CM noise for 8.3A line current and nano-crystalline core	97
Fig. 5-33: Integrated EMI choke.....	99
Fig. 5-34: Discrete EMI choke.....	99
Fig. 5-35: Magnetic field intensity for CM current (left) and DM current (right) in integrated choke	100
Fig. 5-36: Equivalent circuit for the new structure	100
Fig. 5-37: Integrated EMI choke with nano crystalline core and Kool Mu.....	101
Fig. 5-38: DM inductance of both structures.....	102
Fig. 5-39: CM inductance of both structures	102
Fig. 5-40: Transfer gain from DM to CM for integrated structure	103
Fig. 5-41: Transfer gain from CM to DM for integrated structure	103
Fig. 5-42: DM noise measurement for both structures.....	104
Fig. 5-43: CM noise measurement for both structures.....	104
Fig. 5-44: Thermal measurement for the EMI filter with integrated choke	105
Fig. 5-45: Thermal measurement for the EMI filter with discrete chokes	105
Fig. 5-46: “X7R” capacitance behavior in function of DC voltage	106
Fig. 5-47: Impedance comparison for 100 nF ceramic capacitor and different voltage rating.....	107
Fig. 5-48: CM Insertion gain comparison of filter with 100 nF ceramic capacitor and different voltage rating	107
Fig. 5-49: CM noise measurement of filter with 100 nF ceramic capacitor and different voltage rating	107

Fig. 5-50: Impedance of 33 μ F electrolytic and ceramic DM capacitor	108
Fig. 5-51: DM Insertion gain comparison of filter with 33 μ F electrolytic and ceramic capacitor.....	108
Fig. 5-52: DM noise of EMI filter with electrolytic or ceramic capacitor	108
Fig. 5-53: Flow chart of the design procedure of an EMI filter.....	110
Fig. 5-54: Picture of final version of filter.....	111
Fig. 5-55: CM insertion gain for baseline and final version of filter	112
Fig. 5-56: DM insertion gain for baseline and final version of filter	112
Fig. 5-57: CM noise for baseline and final version of filter	113
Fig. 5-58: DM noise for baseline and final version of filter	113

LIST OF TABLES

Table 2-1: Bandwidth dependency on frequency	13
Table 2-2: Current probe transfer impedance	22
Table 2-3: Current probe amplitude example	22
Table 2-4: Noise separator and current probe amplitude Comparison.....	22
Table 3-1: Table of AWG wire sizes.....	39
Table 3-2: Magnetic core size.....	40
Table 4-1: Common cells topologies for EMI filter.....	57
Table 4-2: Components comparison between single and two stages filter	59
Table 5-1: CM choke's design parameters	77
Table 5-2: CM choke's parameters	86
Table 5-3: Choke parameters for 4 Cases.....	88
Table 5-4: DM flux density for two line current cases.....	95
Table 5-5: Core saturation flux density in function of temperature.....	95
Table 5-6: Structures specification at 10 kHz.....	102
Table 5-7: Baseline and final filter specifications.....	111

NOMENCLATURE

Symbol

<i>EMI</i>	ElectroMagnetic Interference
<i>ASD</i>	Adjustable Speed Drive
<i>DUT</i>	Device Under Test
<i>FCC</i>	Federal Communications Commission
<i>CM</i>	Common Mode
<i>DM</i>	Differential Mode
<i>LISN</i>	Line Impedance Stabilization Network
<i>GND</i>	Ground
<i>IGBT</i>	Insulated Gate Bipolar Transistor
<i>PWM</i>	Pulse Width Modulation
i_{CM}	Common mode current (A)
i_{DM}	Differential mode current (A)
v_{CM}	Common mode voltage (V)
v_{DM}	Differential mode voltage (V)
f_s	Switching Frequency (Hz)
C_H	Stray Capacitance between IGBT and heat sink (ground) (pF)
C_g	Stray Capacitance between motor frame and ground (pF)
$dB\mu V$	Decibel microvolts
di/dt	Change in current with time
dv/dt	Change in voltage with time
<i>ESL</i>	Equivalent series inductor
<i>ESR</i>	Equivalent series resistor
<i>EPC</i>	Equivalent parallel capacitor

Chapter 1 Introduction

This chapter starts with the background of conducted electromagnetic interference (EMI) issues in power electronics. It then provides a literature review and a summary of the motivations behind the existing work in related areas. Finally, the objectives of the research are stated and the outline of the thesis is given.

I. Background

Electromagnetic interference (EMI) is defined as undesirable electromagnetic noise that corrupts, limits or interferes with the performance of electronics or an electrical system. These EMI interferences are even more prevalent nowadays with the constant size reduction of electronic circuits and the use of integrated circuits. It is common to define EMI study into four different groups: conducted susceptibility, radiated susceptibility, conducted emissions and radiated emissions [1]. The susceptibility or immunity issues represent the ability of electrical equipment to reject the noise in the presence of external electromagnetic disturbance. The studies of conducted and radiated emissions deal with the undesirable generation of electromagnetic noise from a piece of equipment and the countermeasures that can be taken to reduce it. These emissions are regulated and need to comply with the rule of electromagnetic compatibility (EMC), which is defined as “the ability of a device, unit of equipment or system to function satisfactorily in its electromagnetic environment without introducing intolerable electromagnetic disturbance to anything in that environment” [2]. A good representation of these emission and susceptibility tests is shown in Fig. 1-1, which is taken from [3]. This research is focused on conducted EMI emissions which is generally defined as undesirable electromagnetic energy coupled out of an emitter or into a receptor via any of its respective connecting wires or cables [4]-[5]. Conducted EMI could be analyzed in a wide variety of applications; however this research targets motor drives.

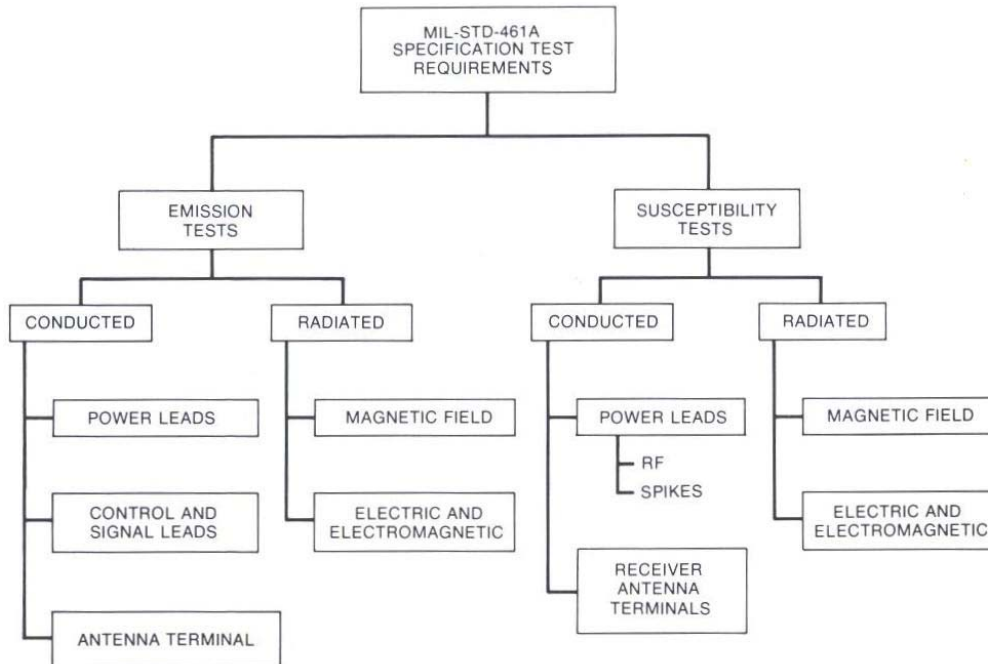


Fig. 1-1: Emissions and susceptibility tests for both conducted and radiated noise

The goal of studying conducted EMI is to understand how the noise is generated and to find the best solution to reduce or eliminate it in order to meet the EMC requirement for the device or system. Two main approaches to dealing with the EMC issue have been used in the industry in the past decade. The first approach is to consider the EMC during the design stage of the equipment by taking into account all the problems from the start. These might include the EMI noise source, noise propagation, or different topologies available that could be used to reduce the EMI generation such as a fourth leg inverter for a motor drive as described in [6], for example. The other approach is to wait until the product is built and tested and then add extra components such as an EMI filter or metal shield. The first method is generally cost effective, shorter and leads to a final version that easily complies with the EMC requirement. In addition, the second approach may add other interference and might, in the worst case, require the redesign of the entire system. However, current research is focused on the second approach, with the design of a high-density EMI filter to reduce the noise of a given motor drive and meet a given EMC standard.

The system under analysis is shown in Fig. 1-2 and represents a typical three-phase motor drive system. The power is fed to a line impedance stabilization network (LISN), EMI filter, DC link cap and an inverter a DC to AC inverter. The inverter is represented by six IGBT switches and linked to a motor via a 10-meter, shielded cable. The LISN is a device defined for each EMI standard that protects the circuit from outside disturbances, creates known impedance on power lines, and is used as a tool when connecting to a spectrum analyzer to measure the noise of the system. Simulations® software are used in this study to confirm behaviors in the time and frequency domain. Furthermore, to verify the integrity of EMI filters, many tests are performed using both small signals and large signals.

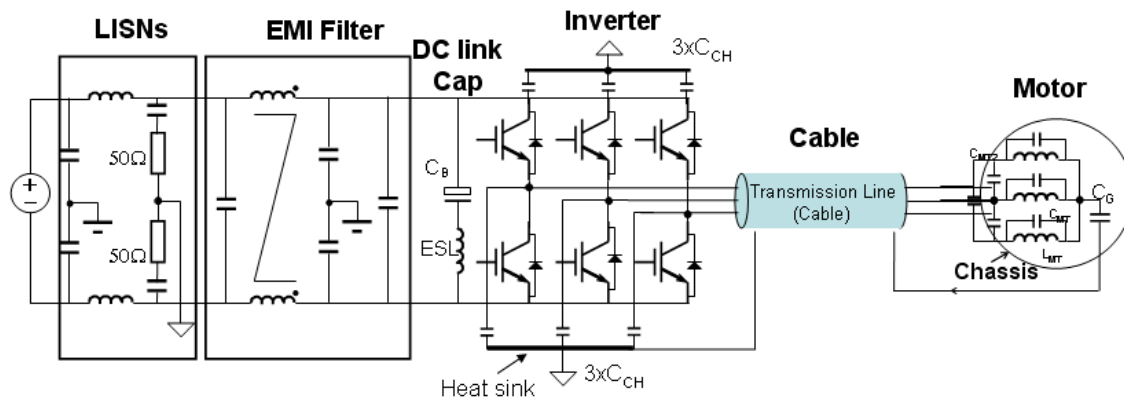


Fig. 1-2: Power train of the complete system under analysis

II. Literature Review and Motivations

The PWM power converter and inverter found in motor drive systems have been extensively used in tremendous numbers of applications, such as transportation systems (in both aerospace and ground industries) and industrial machinery. With the constant progress of high-switching devices, like the insulated gate bipolar transistor (IGBTs), the high dv/dt voltages produced by the inverter have been found to cause many problems, including conducting and radiating EMI noise generation [7] as well as propagating the leakage current in the ground due to stray capacitors inside the motors or the inverter [8]. One of the main issues is that EMI noise interferes not only with power the transmission line of the power converter but also with other electronic equipment. Above all, it is important to understand the EMI noise propagation across the power lines (normal mode

or differential mode) and through the ground (common mode) [9]-[11]. When the path is known and understood the basic method to suppress EMI noise is to implement a discrete passive EMI filter, because of its good performance, reliability, cost and ease of design while maintaining a reasonable size.

Much research has been done in the last decade to suggest other types of filters, such as the integrated passive EMI filter [12] or active filter cancellation [13]-[18]. Past studies have shown that the integrated EMI filter reduces the total volume and profile which increases the power density of the converter. These techniques, like those shown in [12], aim to integrate the entire EMI filter into one package. The viability of the methodology and size reduction have been verified for small power applications. However, when the power is increased, the size gain factor is decreased, and the size becomes undesirable. Other integration techniques have been analyzed, as discussed in [25]-[26]. Their goal is to integrate common mode and differential mode inductance on the same toroidal core in order to reduce the total size of the choke and the size of the differential-mode capacitor. Active filter cancellation has begun to be more popular; however, most of these strategies target only CM cancellation and their reliability hasn't been studied yet. Moreover, active filter cancellation generally requires the use of a hybrid approach that combines using both an active and a passive filter in order to reduce the CM current to a certain level, and then using the active filter to reduce the low-frequency noise. Even with this added complexity, the noise could be attenuated by almost 20dB at low frequency, the total size may not be reduced, and the high frequency could be worse due to the noise generated by the power supply of the active filter.

A conventional adjustable speed drive (ASD) system is shown in Fig. 1-3, which is composed of a three-phase input, rectifier, DC link cap, inverter and load. It is very common to add an EMI filter at the output to the motor drive between the inverter and the motor which is meant to improve the lifetime of the motor and to improve the power quality by reducing overvoltage, ringing, dv/dt and di/dt [19]. Many output filter topologies are available that eliminate one or more of these drawbacks.

An available survey [20] regroups more than 21 topologies and summarizes their advantages and drawbacks. From this survey it can be seen that there is a limited number of filters that help to reduce EMI noise. One of these filters is shown in [21] and

evaluates the use of an unshielded motor cable in an AC ASD application. It is important to mention that implementing some of these filters might be difficult for an existing motor drive due to the DC link feedback. On the other hand, the process could become easier if the DC link feedback is accounted for during the design process. This research focuses on size reduction and performance. Therefore the filter is placed just before the inverter on the DC side to avoid dealing with a three-phase system. The design of the DC passive filter is common, and the method used in [22]-[23] is implemented to build a baseline design. These procedures give an approximate value of the components used in the filter, such as the required inductance and capacitance. When the inductance is known, the common-mode choke can be designed appropriately. The design taken from [24] gives a general idea; however, it over designs the core.

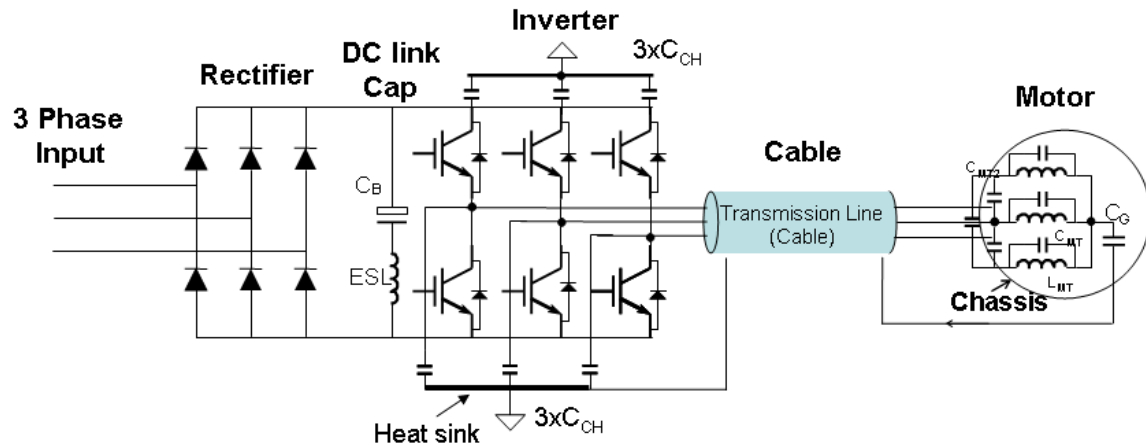


Fig. 1-3: Conventional adjustable speed drive system

Much research has covered EMI issues: however, only a few studies deal with the techniques available to reduce the total filter size. The main goal of this research is to go through the methods available to achieve a high-density discrete passive EMI filter and study the feasibility of using them in combination. Shrinking the size of the filter, thereby pushing components to their limits, leads to many new constraints such as a possible saturation of the CM core and temperature increase. To get around some of these constraints new material technology, grounding practice and CM integrated structure have been revised. For instance, the concept explained in [26] has been upgraded to reduce its size and improve its performance. Its integrity is verified through theoretical analysis and use with small and large signal.

III. Objectives & Scope of Work

The basic way to limit EMI emissions is to use filters to attenuate the noise level in the desired frequency range specified in the EMI standard. The design of these filters is very complex. Trial and error is often needed to achieve a filter that can meet the specifications. For the same reason, an inadequate filter design can result in poor performance, high cost and larger-than-required size. Consequently, for high-density applications, the reduction of the EMI filter size is one of the key goals when designing power electronics equipment.

One of the main objectives of this research is to provide strategies to design and minimize a discrete EMI filter. The correlation between size and performance is studied and some guidelines are given to avoid many common mistakes that can occur in the design and implementation, such as the grounding scheme and its impact on noise. In addition, a novel integrated common-mode choke is investigated and proposed to achieve size reduction.

IV. Thesis Outline and Summary of Contribution

Chapter 2 of this thesis discusses the characterization of the EMI noise, such as the difference between the common-mode and differential-mode noise in a motor drive, and the procedure and recommendations for measurement in these two modes. Later on, the limitations (frequency limit, noise level) and setup of EMI standards are considered. Finally, the experiment setup, including system characteristics and running conditions, that is used to measure the large signal noise is defined.

Chapter 3 is dedicated to the baseline design of an EMI filter. In the first steps, the design procedure, filter materials consideration and preliminary design of the CM choke are specified. Then, the modeling of the CM choke and capacitors is determined to model the entire filter and compared with its insertion gain. Finally, the large-signal tests are measured and the size of the baseline filter is recorded.

Chapter 4 is committed to consideration of the filter topology and the grounding effect. In the first section the approach to choosing the filter structure is studied and the best solution for this application is proved for both the CM and DM single-stage filter. In

addition, some concerns about multi-stage filters are given. In the last section, the grounding scheme is analyzed and tested to provide guidelines during experimental tests and design.

Chapter 5 is devoted to the possible approaches to minimizing the size and improving performance of the EMI filter. In the first part, the typical “ferrite” CM choke core material is compared with the “nano-crystalline” technology. Later on, the CM choke parameters are identified while their effects are studied in large-signal tests. To conclude a new integrated structure combining both common-mode and differential-mode inductance is considered and implemented.

Finally, Chapter 6 affirms the main conclusions of this thesis, and suggests some future work. A strategy for designing and minimizing a discrete EMI filter is proposed based on experimental measurements and trial and error. It is important to model the system completely, including analyzing and measuring the input impedance of the motor drive, in order to design the input filter appropriately, while respecting the impedance mismatch as well as to understand high-frequency behavior.

Chapter 2 EMI Analysis

I. EMI Definition and Noise Propagation

A. Common-Mode and Differential-Mode Noise Characterization

The conducted EMI noise is usually decoupled and characterized as common-mode (CM) and differential-mode (DM) noise. CM noise is defined as the noise flowing between the power circuit and the ground, while DM noise is defined as the current following the same path as the power delivery as shown in Fig. 2-1. The same analysis applies to the power converter in Fig. 1-2. As explained in [27], it is common to separate the CM and DM noise from the measured noise with a noise separator. Many benefits are gained from this, including simplicity of the filter design, as each mode could be designed independently; and troubleshooting with the possibility to know directly which mode is not meeting the standard and therefore reduces the number of tries and errors during the design stage.

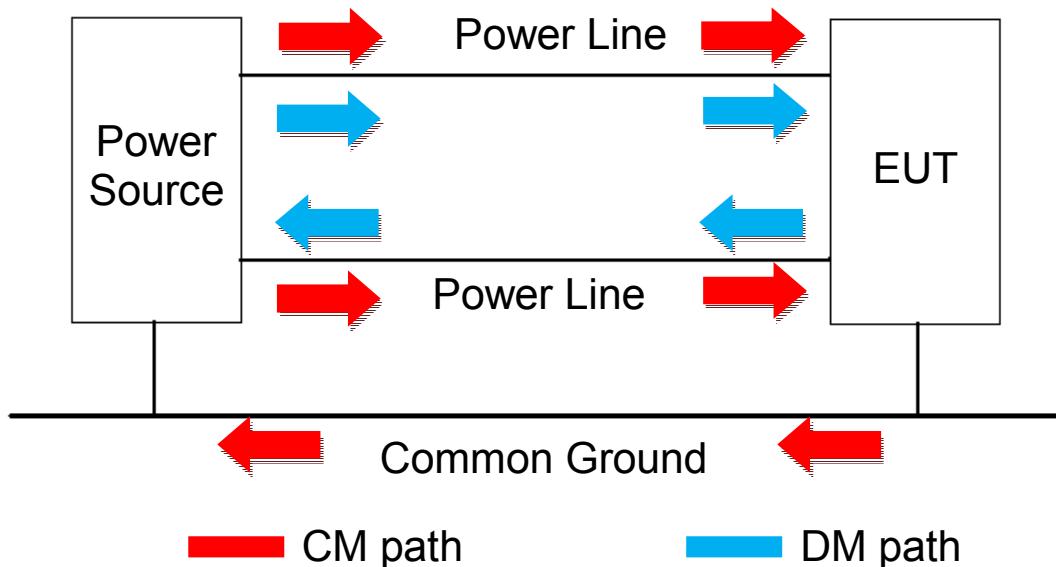


Fig. 2-1: CM and DM noise distribution

A simple model is used in Fig. 2-2 to understand the relationship between the CM and DM current. The noise source of the motor drive can be represented by voltage source V_N , while Z_g represents the impedance from the motor drive to the ground, and Z_1 and Z_2 represent the line impedance. As mentioned earlier, a LISN must be used to measure the EMI noise, and it is represented by its equivalent output impedance of $50\ \Omega$ per line [28].

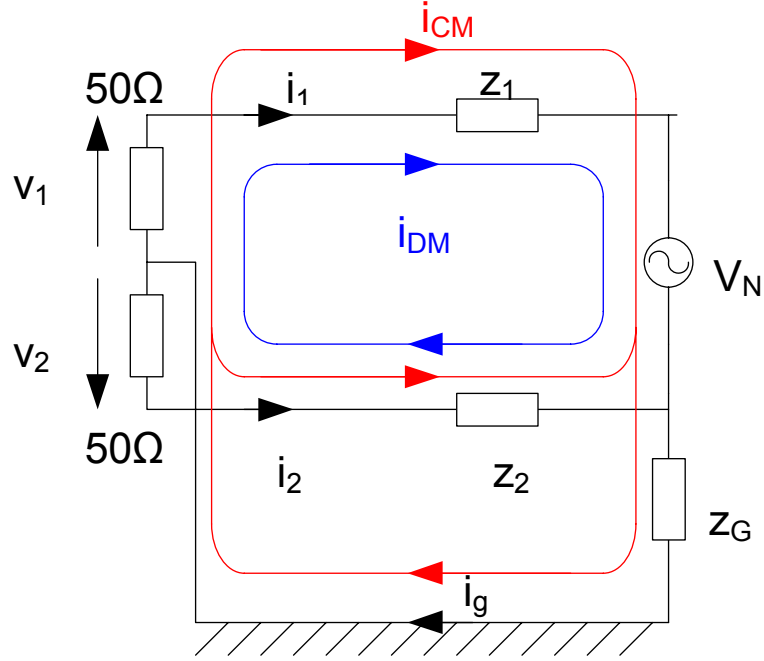


Fig. 2-2: CM and DM equivalent noise path with LISN

Knowing that the currents through Z_1 and Z_2 are denoted i_1 and i_2 , respectively, and the ground current i_g is through the impedance Z_g , we can derive the following equations (2-1).

$$\begin{aligned}
 i_1 &= i_{CM} + i_{DM} \\
 i_2 &= i_{CM} - i_{DM} \\
 i_{CM} &= \frac{i_1 + i_2}{2} \\
 i_{DM} &= \frac{i_1 - i_2}{2} \\
 i_g &= 2i_{CM} \\
 v_1 &= -50i_1 = -50(i_{CM} + i_{DM}) \\
 v_2 &= -50i_2 = -50(i_{CM} - i_{DM})
 \end{aligned} \tag{2-1}$$

Finally, using equations in (2-2), we can derive the equivalent common-mode noise and differential-mode noise across the theoretical $50\ \Omega$ impedance of the LISN.

$$\begin{aligned}
v_{CM} &= -50i_{CM} = -50\left(\frac{i_1+i_2}{2}\right) = \frac{v_1+v_2}{2} \\
v_{DM} &= -50i_{DM} = -50\left(\frac{i_1-i_2}{2}\right) = \frac{v_1-v_2}{2} \\
v_1 &= v_{CM} + v_{DM} \\
v_2 &= v_{CM} - v_{DM}
\end{aligned} \tag{2-2}$$

A noise separator [29] is used in the research experiments to extract both CM and DM noise components, from the measure total voltage v_1 and v_2 . The integrity of the noise separator is verified in a later section. It is essential to note that the EMI standard is dealing with the voltage v_1 and v_2 which imply that a margin of 6 dB below the limit is needed when looking at v_{CM} and v_{DM} to make sure that the total noise meets the standard.

B. Noise Propagation

For a typical motor drive system like the one shown in Fig. 1-2, the DM and CM noise are produced by the switching operations of the inverter, which is controlled by a PWM modulation scheme. While they have the same noise origin, the propagation path for these two modes is different. The DM noise transmitted through the power transmission line to the power source and motor. Conversely, the CM noise flows through the power lines to the ground via stray capacitances. In Fig. 1-2 C_H represents the stray capacitances between the IGBTs and the heat sink, while C_G is the equivalent capacitor between the motor frame and the ground. It is also important to take into account the stray capacitances of cables (not shown in the figure) between the inner conductors and the shield and ground. Experimentation shows that the stray capacitance of the motor is dominant, and is measured to be around 4-5 nF. On the other hand, the total stray capacitance of the IGBT module and heat sink are about 50 pF and the stray capacitance of the wire is 45 pF/m. This capacitance could be quite significant and become predominant for long cable applications such as those in aerospace where dozens of meters of cable are used [35]-[36]. From this analysis, it is clear that the EMI filter needs to be placed in a position where it will eliminate the three CM paths, even though the path from the IGBT to the heat sink is small. Therefore, placing the filter at the input on the DC link side is the best solution and should lead to a smaller design.

II. EMI Standards

Many standards exist to accommodate the wide variety of applications where EMI is an issue. Most of the standards differ either by their frequency range of application or the amplitude of the noise and whether the type of noise measured is voltage or current. They also have their own experimental and noise measurement setup as well as their own LISN circuit. It is common to see EMI standards beginning at 150 kHz and ending in the mega hertz range around 30 MHz, like the DO160 standard [30]. However this research is based on the Military Standard 461E described in [31] which starts at 10 kHz and end at 10 MHz.

A. Setup

Many experimental setups are defined by the Military Standard 461 E. However, for this research, the general setup shown in Fig. 2-3 is used. It is composed of a table covered with a ground plane where the LISN and the equipment under test (EUT) are placed. These two pieces of equipments need to be connected through a two-meter power line wire positioned on a non-conductive standoff of 5 cm height to avoid any disturbances from the ground.

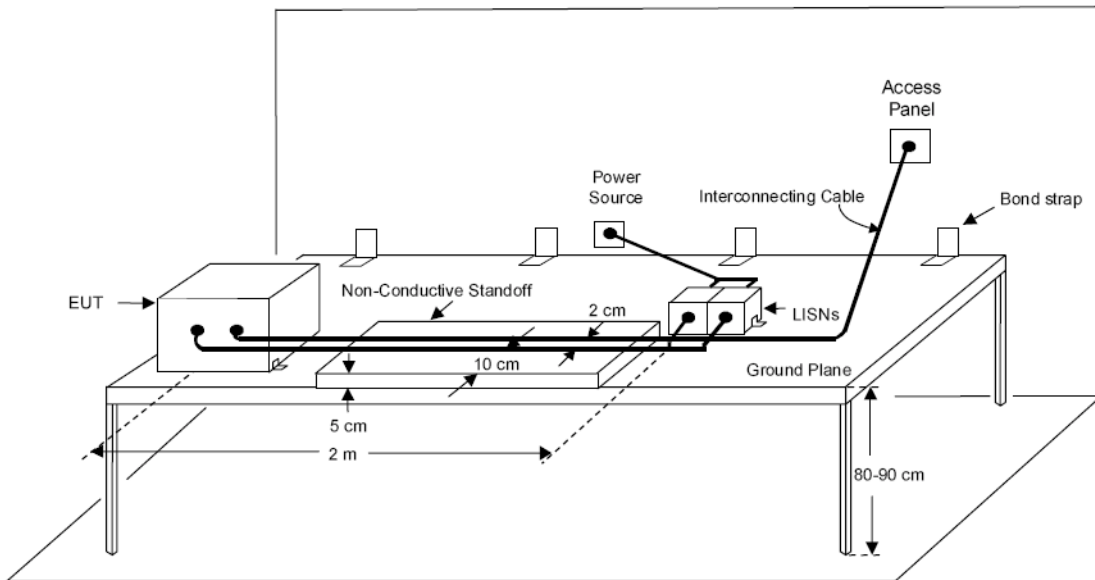


Fig. 2-3: Experiment setup of the Military Standard 461E

The LISN is defined in accordance with Fig. 2-4, and the main difference between this LISN and the other LISN is the inductance of $50\ \mu\text{H}$ per line while [30] has only $5\ \mu\text{H}$ per line.

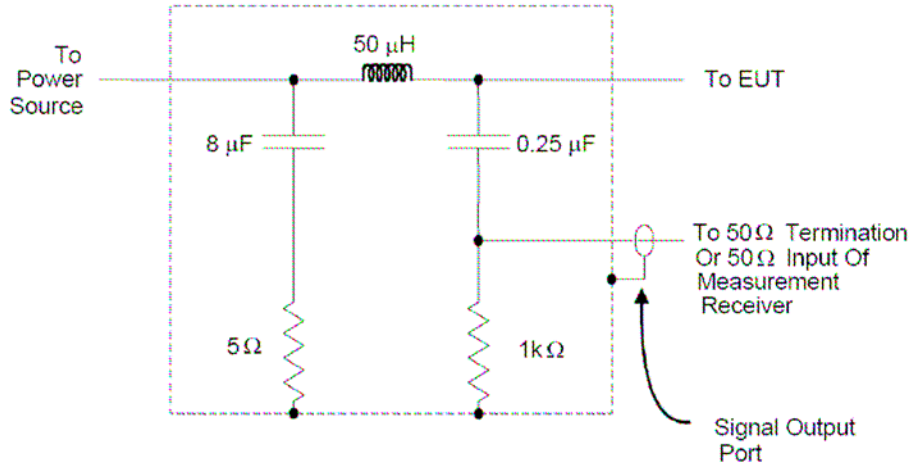


Fig. 2-4: LISN circuit characteristics

B. Frequency Limit and Bandwidth

In contrast with other standards, the Military 461 E has a frequency range, limited from 10 kHz to 30 MHz. Fig. 2-5 defines the maximum noise limit for the conducted EMI noise. It is important to mention that this norm is given for a voltage of 28 V, and as the voltage increases some relaxation of this limit is permitted. For this research, the input voltage is set to 300 V, so another 10 dB of noise is allowed. On the other hand, this limit relaxation will be served as margin to compensate for the CM and DM voltage measurements via the noise separator. The amplitude boundary drops from 94 dB μV at 10 kHz to 60 dB μV at 500 kHz with a negative slope of 20dB/dec and then stays at 60 dB μV until 10 MHz.

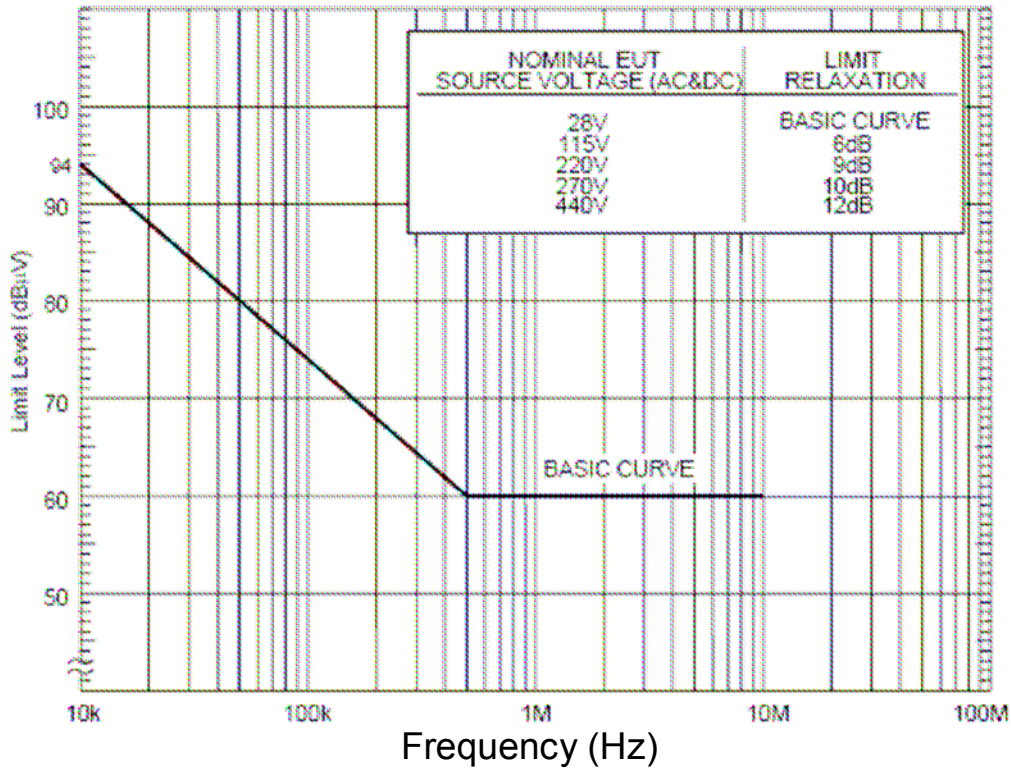


Fig. 2-5: EMI standard on voltage

Moreover, the spectrum analyzer connected to the LISN needs to be set with a certain bandwidth that is dependent on the frequency. As shown in Table 2-1, for a frequency range of 10 kHz to 150 kHz, the bandwidth set on the spectrum analyzer is 1 kHz while from 150 kHz to 30 MHz the bandwidth is 10 kHz. This helps to explain the discontinuity that will be observed in the future large signal results in the frequency domain.

Table 2-1: Bandwidth dependency on frequency

Frequency Range	6 dB bandwidth
30 Hz – 1 kHz	10 Hz
1 kHz – 10 kHz	100 Hz
10 kHz – 150 kHz	1 kHz
150 kHz – 30 MHz	10 kHz
30 MHz – 1GHz	100 kHz
Above 1GHz	1 MHz

C. Restrictions

Other restrictions and standards exist, such as the power characteristic given by the Military Standard 704 F [32], but this research focuses on the subject of EMI and does not consider other power standards. On the other hand, some constraints apply to the maximum common mode capacitance allowed in the EMI filter due to the grounding current safety standard. According to the SAE AS 1831 standards [33], the maximum capacitance value is set to 100 nF per line to ground “6.1.6 User Equipment AC Ground Isolation: The leakage capacitance to ground at the user interface shall not exceed the lower of 0.005 $\mu\text{F}/\text{kW}$ of connected load or 0.1 μF measured at 1 kHz for each user equipment DC power and return line.” The filter design follows this standard to limit the CM current going through the ground as well as setting a baseline for comparison between the different versions of version.

III. Experiment Setup

A. System characteristics

The experiment setup shown in Fig. 2-6 was built to be similar to the experiment setup stated in the military standard. A table with a copper ground plane is used, and the LISN and EUT are screwed to the table. For convenience, the motor is placed on the ground floor and connected to the motor drive via a 10-meter shielded cable. The ground and shield wires are connected on one end to the motor frame and on the other end to the MD and ground plane. A non-conductive standoff is used to place the two-meter-long power line connecting the LISN and MD. The EMI filter is placed close to the MD, and its ground connection will be studied in a later chapter. Finally, the input side of the LISN is connected to a DC generator providing 300 Vdc (± 150 Vdc), while the measurement output is connected to the 20 dB attenuator and the spectrum analyzer.

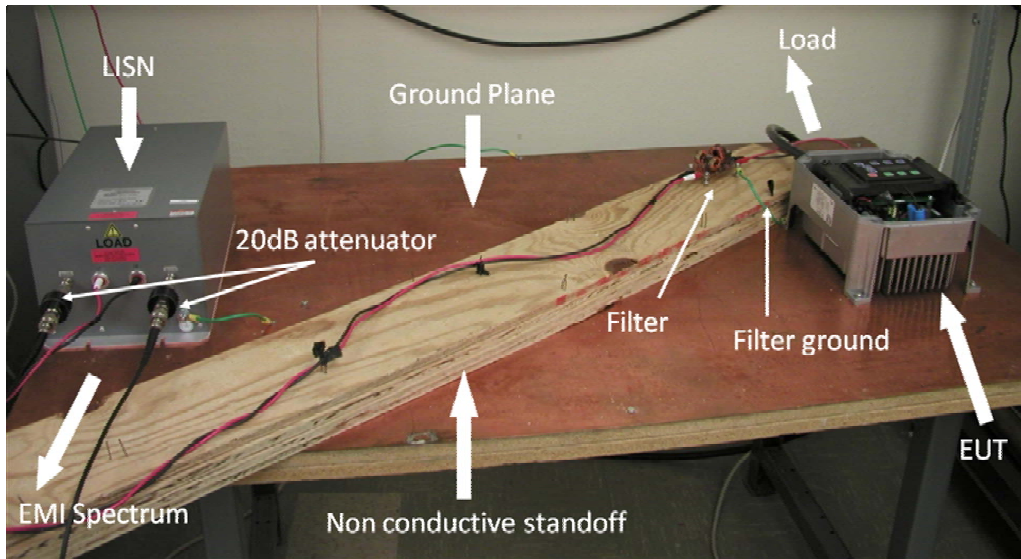


Fig. 2-6: Experiment setup

The LISN box shown on the left has been chosen to meet the criteria of the EMI standard and integrate on the same LISN package for each line. It has two inputs and outputs line voltage and two measured BNC connectors across 1000Ω . The impedance of one LISN is measured with the impedance analyzer Agilent 4294A (40 Hz – 110 MHz), and its impedance when the other output is terminated by a 50Ω resistor is given by Fig. 2-7. It is very similar to the impedance of the standard shown in Fig. 2-8.

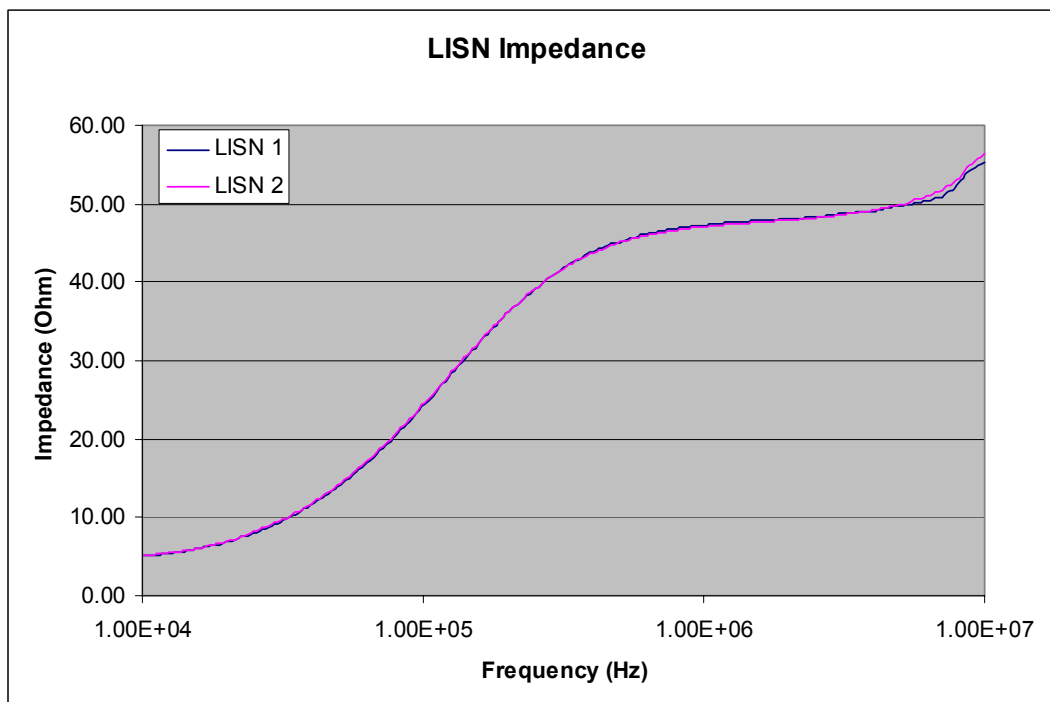


Fig. 2-7: Measured impedance of LISN

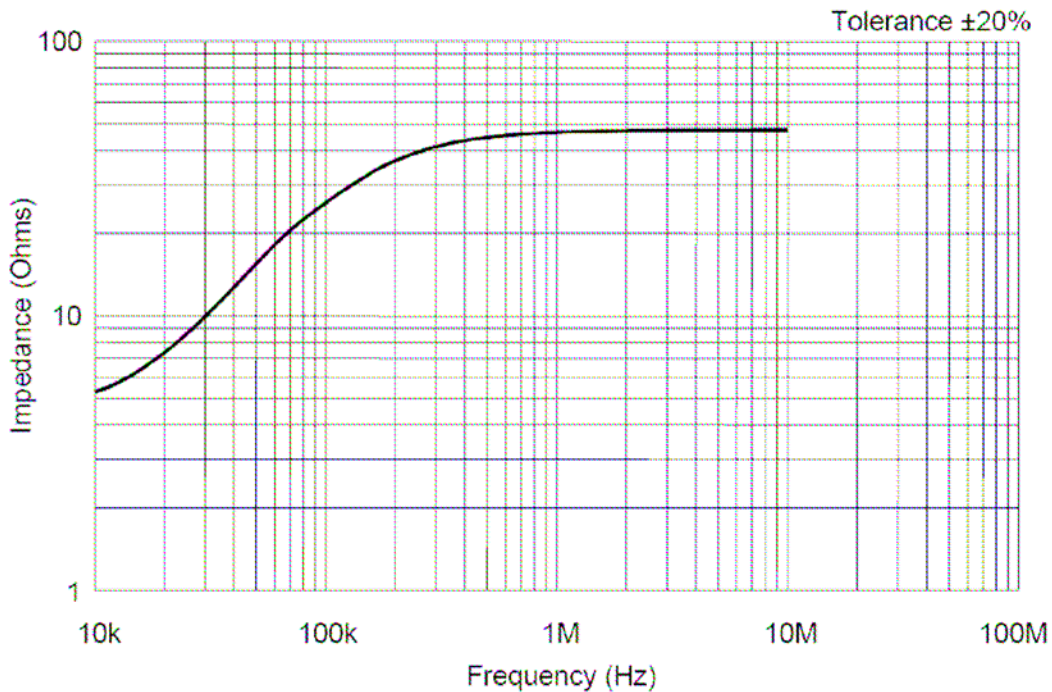


Fig. 2-8: Impedance of LISN from Military Standard 461 E

The standard specifies to use external attenuation of 20 dB. However, in certain cases, the external attenuation had to be increased to protect the spectrum analyzer from the large voltage noise. The EMI spectrum analyzer used for all measurement is the Hewlett Packard 4195A (10 Hz – 500 MHz) set to the correct bandwidth, while varying the internal attenuation to avoid overload without changing the external attenuator. Changing the internal attenuation doesn't change the amplitude of the noise when recorded. Only the background noise is affected, and therefore adding too much internal attenuation would make it impossible to see low level changes.

The MD used for the experiment is shown in Fig. 2-9, and is a three-phase commercial back-to-back MD of 7.5 HP (5.5 kW). The switching frequency and running frequency could be set from 3 to 16 kHz and 0.1 to 400 Hz (motor rated speed is 60 Hz), respectively. However, since the goal of this research is to design a DC EMI filter, the drive is used only for DC to AC by injecting the DC voltage across two lines. The internal DC link capacitor is composed of two series capacitors of 47 μ F to create a neutral point.

Finally, the load is composed of a synchronous motor of 5 HP wired in a low voltage configuration (208-230 V) with a maximum frequency of 60 Hz, and is connected to a fan as shown in Fig. 2-10.



Fig. 2-9: MD used for experiment



Fig. 2-10: Load used for experiment

B. Running Conditions

The input generator provides an input voltage of 300 Vdc (± 150 Vdc per line). The switching frequency of the MD is set to 12 kHz while the line frequency is varied, depending on line current and power desired. When the line frequency is increased, the line current will also augment and a bigger power is achieved which will impact the EMI filter.

C. Conducted EMI Noise Measurement Procedure

The use of the LISN is necessary to measure the noise under constant power condition. The internal circuit of the LISN was shown in Fig. 2-4; however, it needs to be studied in detail. At low frequency (line frequency), the LISN can be considered to be short and won't interfere with rest of the system. However, at high frequency, the high impedance of the inductor blocks the current noise and the path is provided via the 0.1 μ F capacitor to the 50 Ω termination of the spectrum analyzer connected in parallel to the 1 k Ω , as shown in Fig. 2-11.

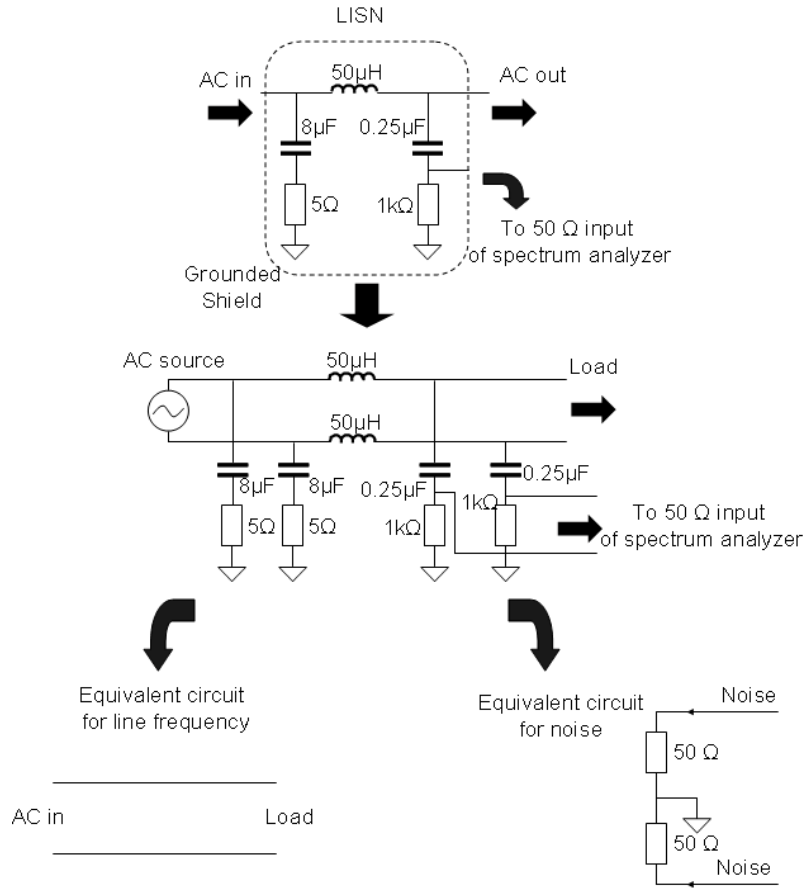


Fig. 2-11: LISN equivalent circuit for noise and line frequency

The noise voltage is therefore extracted by following the measurement setup given by the military standard, which is illustrated in Fig. 2-13. As shown earlier, the LISN is placed between the power input and the equipment being tested. The noise is directly measured at the signal output of the LISN with the introduction of an attenuator to protect the measurement receiver and to prevent overload. Finally, a correction factor needs to be applied to the raw data to compensate for the 20dB attenuator and the voltage drop across the coupling capacitor (0.25 μF). This capacitor is in series with a combination of the 1 kΩ LISN resistor and the 50 Ω measurement receiver. The correction factor is equal to (2-3) and is represented in Fig. 2-12.

$$(Correction\ Factor)_{dB} = 20 \log_{10} \left[\frac{(1 + 5.60 \times 10^{-9} f^2)^{1/2}}{(7.48 \times 10^{-5} f)} \right] = CF \quad (2-3)$$

Where f is the frequency of interest in Hz.

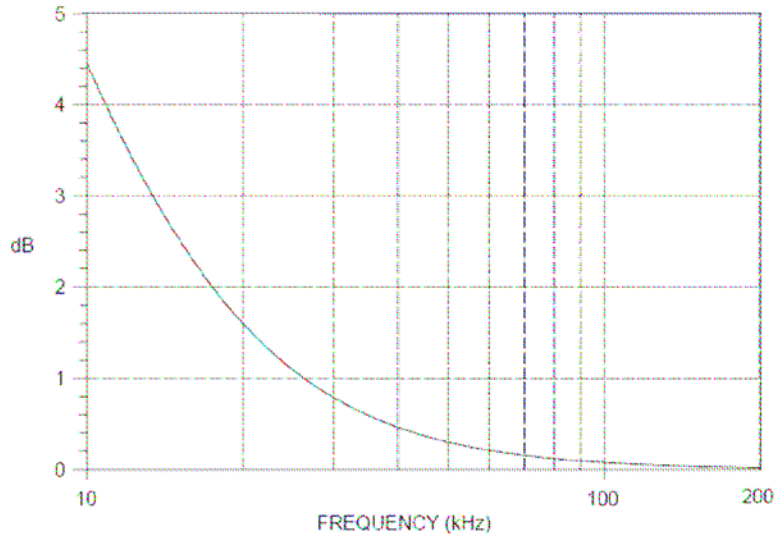


Fig. 2-12: Correction factor for LISN capacitor

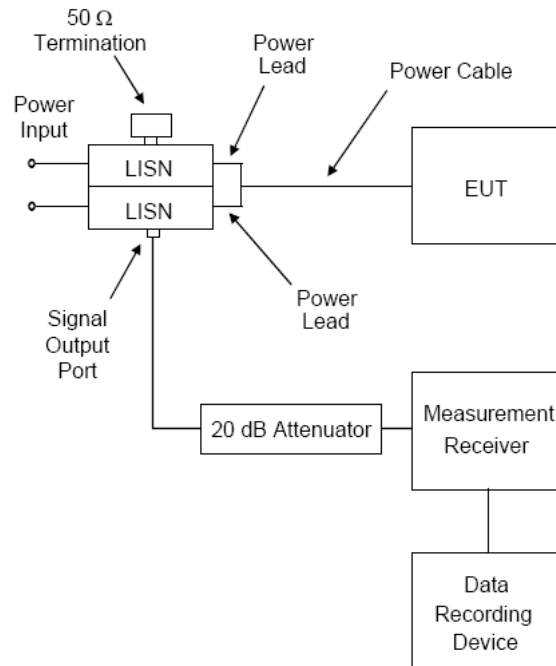


Fig. 2-13: Voltage measurement procedure

For convenience the noise separator introduced in [29] has been built and its integrity has been verified by comparing its result to the noise measured with a current probe. The EMI current probe is ETS-LINDGREN model 91550 and its characteristics are given in [34]. The decoupling of the two modes is done simply by changing the wire direction, as shown in Fig. 2-14.

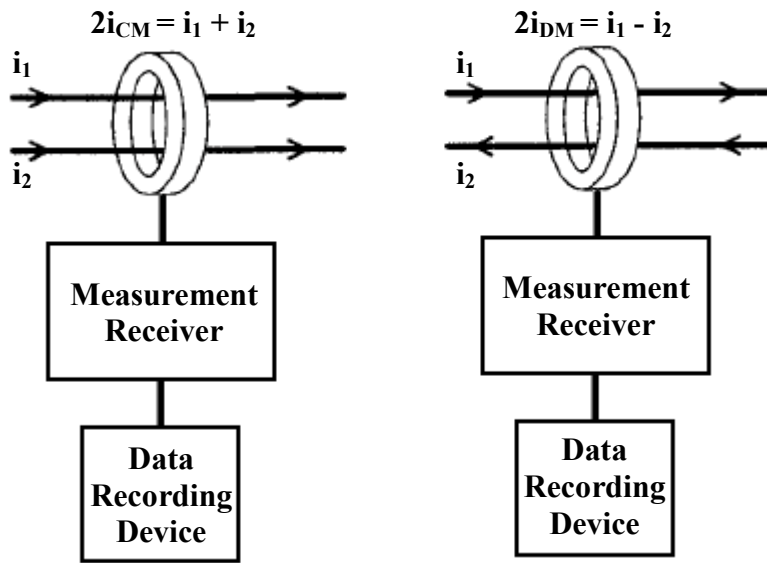


Fig. 2-14 CM (left) and DM (right) noise measurement with current probe

The current measurement process represented in Fig. 2-15 is slightly different from the voltage measurement process.

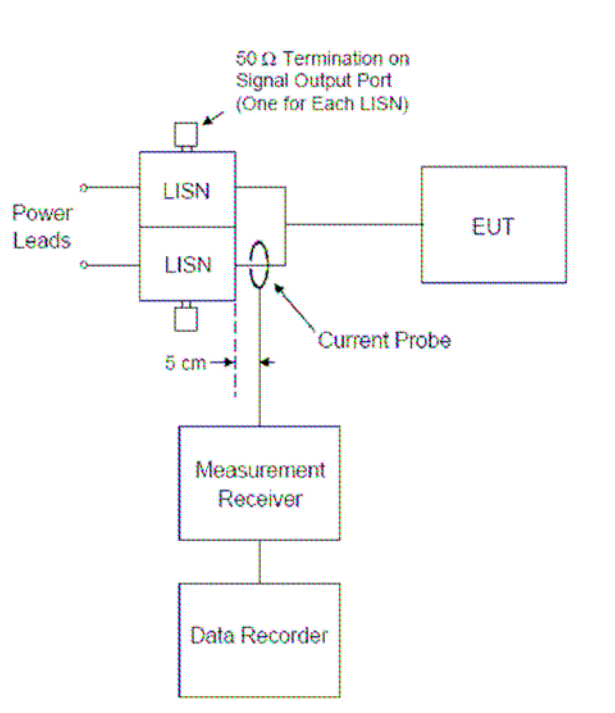


Fig. 2-15: Current measurement procedure

The measurement of both CM and DM noise with the noise separator and the current probe are shown in Fig. 2-17 and Fig. 2-18. The shapes of the two curves are almost identical and differ only by their amplitude due to a few factors. In order to determine the

current in the conductor (I_p), the reading of the current probe output in microvolts (E_s) need to be divided by current transfer impedance (Z_T) as shown in (2-4).

$$I_P = \frac{E_s}{Z_T} \quad (2-4)$$

The current probe transfer impedance is given in Fig. 2-16 and summarized in Table 2-2. When the current is known, it needs to be multiplied by the impedance of the LISN as shown in (2-5). The impedance of the LISN as a function of the frequency is given in Fig. 2-7. Finally, the correction factor (CF) shown in Fig. 2-12 needs to be taken into account for the comparison.

$$V_{CM_measured\ w/\ current\ probe} = \frac{2i_{CM}}{Z_{probe\ transfer}} \times \frac{Z_{LISN}}{2} = V_{CM_noise\ separator} + CF$$

$$20\log(V_{CM_measured\ w/\ current\ probe}) = 20\log\left(\frac{2i_{CM}}{Z_{probe\ transfer}} \times \frac{Z_{LISN}}{2}\right) = 20\log(V_{CM_noise\ separator}) + CF$$

$$(V_{CM_noise\ separator})_{dB} = (2i_{CM})_{dB} - (Z_{probe\ transfer})_{dB} + \left(\frac{Z_{LISN}}{2}\right)_{dB} - CF \quad (2-5)$$

$$V_{DM_measured\ w/\ current\ probe} = \frac{2i_{DM}}{Z_{probe\ transfer}} \times \frac{Z_{LISN}}{2} = V_{DM_noise\ separator} + CF$$

$$20\log(V_{DM_measured\ w/\ current\ probe}) = 20\log\left(\frac{2i_{DM}}{Z_{probe\ transfer}} \times \frac{Z_{LISN}}{2}\right) = 20\log(V_{DM_noise\ separator}) - CF$$

$$(V_{DM_noise\ separator})_{dB} = (2i_{DM})_{dB} - (Z_{probe\ transfer})_{dB} + \left(\frac{Z_{LISN}}{2}\right)_{dB} - CF$$

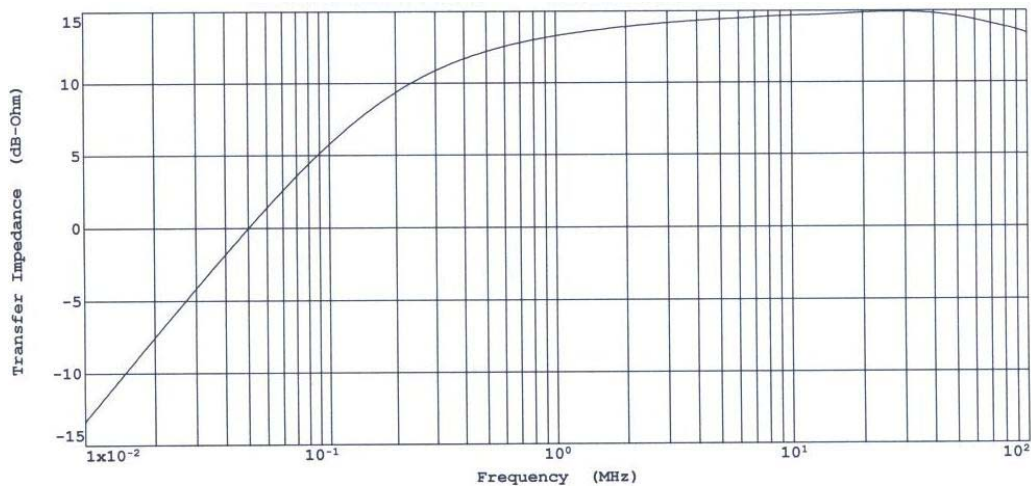


Fig. 2-16: Current probe transfer impedance

Table 2-2: Current probe transfer impedance

Frequency (MHz)	Transfer Impedance (dB Ohms)	Transfer Impedance (Ohms)
0.010	-13.39	0.214
0.020	-7.53	0.420
0.100	5.15	1.809
0.500	12.18	4.064
1.000	13.28	4.616
2.000	13.92	4.966
3.000	14.18	5.117
10.000	14.66	5.408

To verify the reliability of these equations, different frequencies are taken below.

Table 2-3: Current probe amplitude example

Noise Type	Frequency	Current Probe Amplitude	LISN Impedance	Current Probe Transfer Impedance	CF
CM	12 kHz	68.6 dB μ A	$\frac{6}{2}\Omega \rightarrow 9.5_{dB}$	-10 dB Ω	4 dB
DM	12 kHz	76.2 dB μ A	$\frac{6}{2}\Omega \rightarrow 9.5_{dB}$	-10 dB Ω	4 dB
CM	≈ 3.5 MHz	65.4 dB μ A	$\frac{50}{2}\Omega \rightarrow 27.9_{dB}$	14.3 dB Ω	0 dB
DM	≈ 2.5 MHz	40.5 dB μ A	$\frac{50}{2}\Omega \rightarrow 27.9_{dB}$	14.0 dB Ω	0 dB

Table 2-4: Noise separator and current probe amplitude Comparison

Noise type	Frequency	Noise Separator Amplitude	Equivalent Current Probe Measurement	Error
CM	12 kHz	83.5 dB μ V	84.1 dB μ V	0.7%
DM	12 kHz	91.0 dB μ V	91.7 dB μ V	0.8%
CM	≈ 3.5 MHz	74.2 dB μ V	79.0 dB μ V	6.5%
DM	≈ 2.5 MHz	54.2 dB μ V	54.4 dB μ V	0.4%

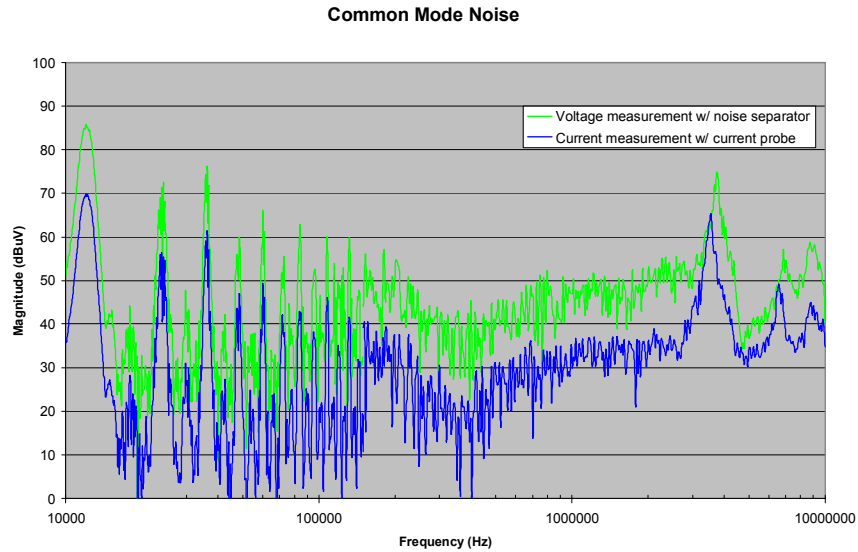


Fig. 2-17: CM noise measurement with noise separator and current probe

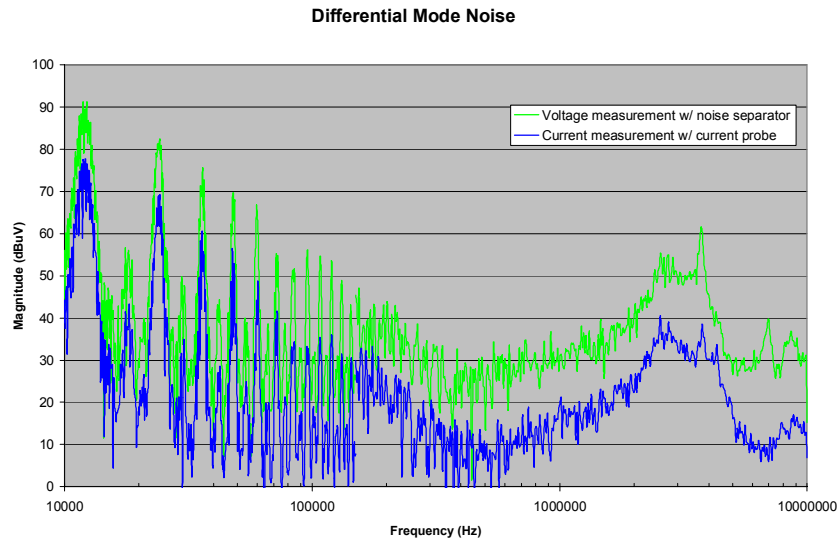


Fig. 2-18: DM noise measurement with noise separator and current probe

The difference between using a current probe and the noise separator is really small for the three cases, while the difference is around 7% for the fourth case. This might be due to the approximation when reading the LISN impedance, probe transfer impedance or during the measurement setup. It happens quite often that the high-frequency noise differs from one measurement to the other. To facilitate the measurement process and to keep the experiment analogous, the noise separator will be used for the remainder of the research.

Now that the experiment and measurement process have been described, the design of an EMI filter will be studied in details.

Chapter 3 Baseline EMI Filter Design

I. Introduction

The design of a passive EMI filter is not new and numerous amount of research on this topic has been done in the past. Many of these publications suggest a design process that meets the low-frequency requirement but does not take into account the high-frequency. Therefore, the industry practice is often based on a trial-and-error method to design and optimize the EMI filter to meet EMC standards. Even though the norm is to only consider the total noise of the system, both CM and DM noise need to be attenuated. Moreover, this chapter shows that these two modes interfere with each other. An increase in CM noise generally leads to an augmentation of the DM noise due to the asymmetry of the system.

Since the effective range of EMI is between 10 kHz and 10 MHz, it is important to consider the components' parasitics and behavior at high frequencies during the design process. The filter parasitics such as the equivalent parallel capacitance of the winding (EPC), equivalent series inductors (ESL) and resistors (ESR) of the capacitors alter the attenuation performance of the EMI filter and need to be considered carefully. Moreover, the effectiveness of an EMI filter also depends on the noise source impedance of the power converter. Even though the design of the EMI filter could be simplified by knowing the input impedance of the converter, it is quite complex and time-consuming to analyze and measure this impedance. This research did not measure the noise source impedance, however, as mentioned in the suggested future work, knowing the noise source impedance could answer some questions especially some behavior at high frequency.

The beginning of this chapter presents an initial baseline filter based on these approaches and comments on its performance. This baseline filter is afterward used for experimenting with some filter topologies and grounding issues. It was shown earlier that the ground path is tremendously important for CM noise and a bad grounding practice may reduce the attenuation of the filter. Later on, a new design approach that considers many more parameters; such as the temperature of the core, saturation, and core material;

will be used to improve the common-mode choke of the filter and reduce its total volume. Furthermore, a new integrated structure is studied that allows the combination of both the CM and DM inductor with the same winding inductance. Finally, the impact of capacitor voltage rating on EMI noise is studied.

II. Design Procedure

The typical approach used in [22]-[23] was used to design a baseline EMI filter for the experiment shown previously. A basic network filter topology shown in Fig. 3-1, is used to attenuate both CM and DM noise. It is composed of elements that affect CM noise or DM noise only, and others that affect both CM and DM noise. The capacitors C_y which is generally in the nano farad range, in theory attenuates both CM and DM noise; however, its value is very small compared to C_{x1} and C_{x2} which are in the micro farad range, so its effect on the DM noise is almost negligible. On the other hand, the capacitor C_x between the power lines attenuates the DM noise only. The main component of the filter is the common-mode choke L_{CM} which ideally suppresses only the CM noise; nevertheless its leakage inductance between the two windings ($L_{leakage}$) is used to eliminate the DM noise. It could be helpful in some cases to add an extra inductor in series with the choke to increase the total DM inductance if the leakage provided by the CM choke is too small.

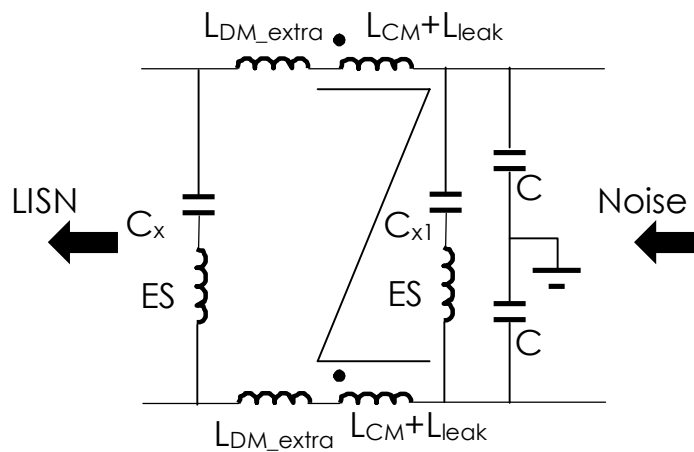


Fig. 3-1: Baseline EMI filter

The equivalent circuit of the filter for each mode is represented in Fig. 3-2 and Fig. 3-3 for the CM and DM sections, respectively. The network topology for the CM filter is

an “LC” type filter while the topology for the DM is a “ π ” type with two C_x capacitors. The common rule is to obtain the maximum impedance mismatch between the filter and the outside system. The analysis below illustrates the concept with a specific example. Note that the LISN is characterized for each line by a 50Ω resistor and is approximated by a 25Ω or 100Ω resistor for CM and DM correspondingly, using two resistors in parallel or in series.

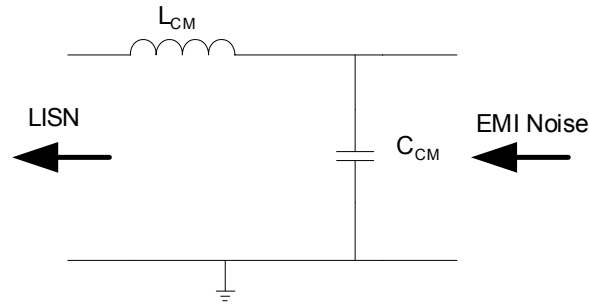


Fig. 3-2: CM equivalent filter circuit

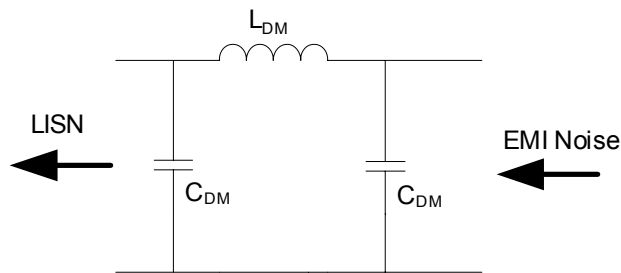


Fig. 3-3: DM equivalent filter circuit

The equivalent CM noise source of the system could be represented by the average collector voltage of the IGBT device in series with equivalent impedance Z_g . Therefore when following the approximated process shown in Fig. 3-4 the common mode attenuation could be derived in (3-1).

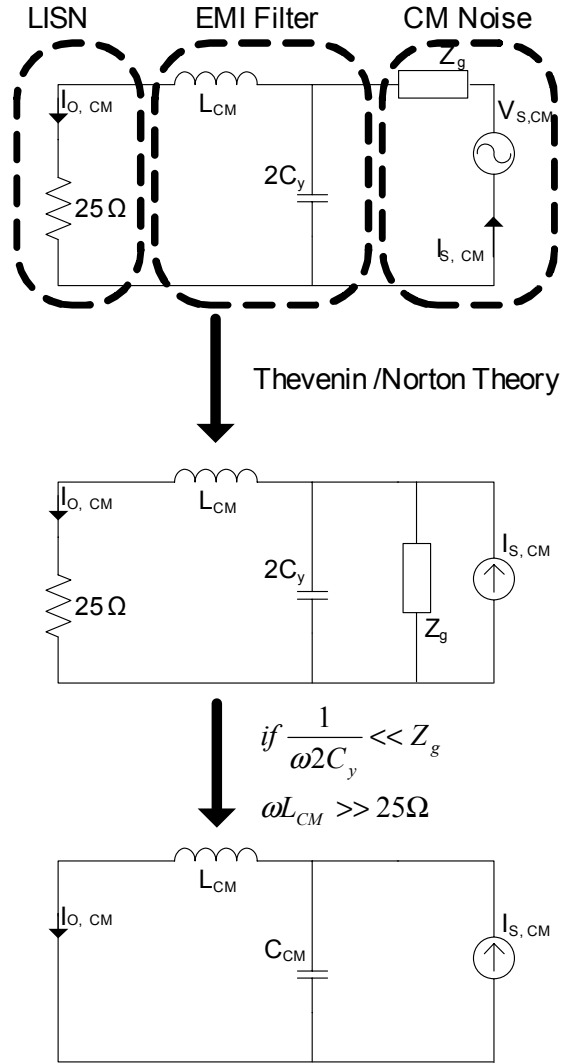


Fig. 3-4: Equivalent circuit for the derivation of CM filter attenuation

$$CM \text{ attenuation} \approx \frac{v_{LISN(\text{without filter})}}{v_{LISN(\text{with filter})}} \approx \frac{I_{S_CM(25\Omega)}}{I_{O_CM(25\Omega)}}$$

$$\frac{I_{S_CM(25\Omega)}}{I_{O_CM(25\Omega)}} = \frac{Z_{L_{CM}} + Z_{C_{CM}}}{Z_{C_{CM}}} = \frac{j\omega L_{CM} + \frac{1}{j\omega C_{CM}}}{\frac{1}{j\omega C_{CM}}} = 1 + j^2 \omega^2 L_{CM} C_{CM} \quad (3-1)$$

$$\frac{I_{S_CM(25\Omega)}}{I_{O_CM(25\Omega)}} = 0 = 1 - (2\pi f_{CM})^2 L_{CM} C_{CM}$$

$$f_{CM} \approx \frac{1}{2\pi \sqrt{L_{CM} C_{CM}}} \text{ with } C_{CM} = 2C_y$$

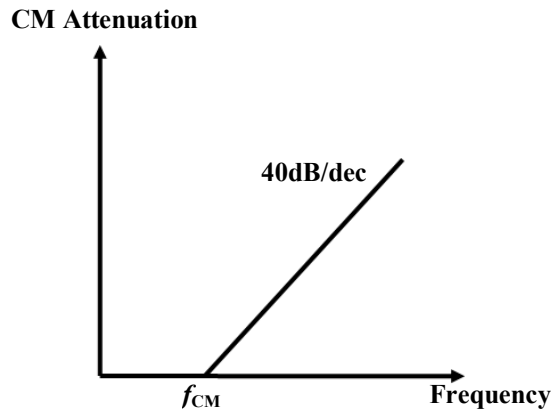


Fig. 3-5: Common Mode noise filter theoretical attenuation

The theoretical CM noise attenuation is therefore approximated by a 40dB/dec slope passing through the resonance of L_{CM} and C_{CM} as shown in Fig. 3-5.

The same analysis could be done for the DM noise; however, the noise source characterization for DM noise is more complex to define due to the DM input impedance of the motor drive. For the sake of simplicity and to understand the design process for a particular case, the equivalent noise source is assumed to be a voltage source in series with low impedance Z_T .

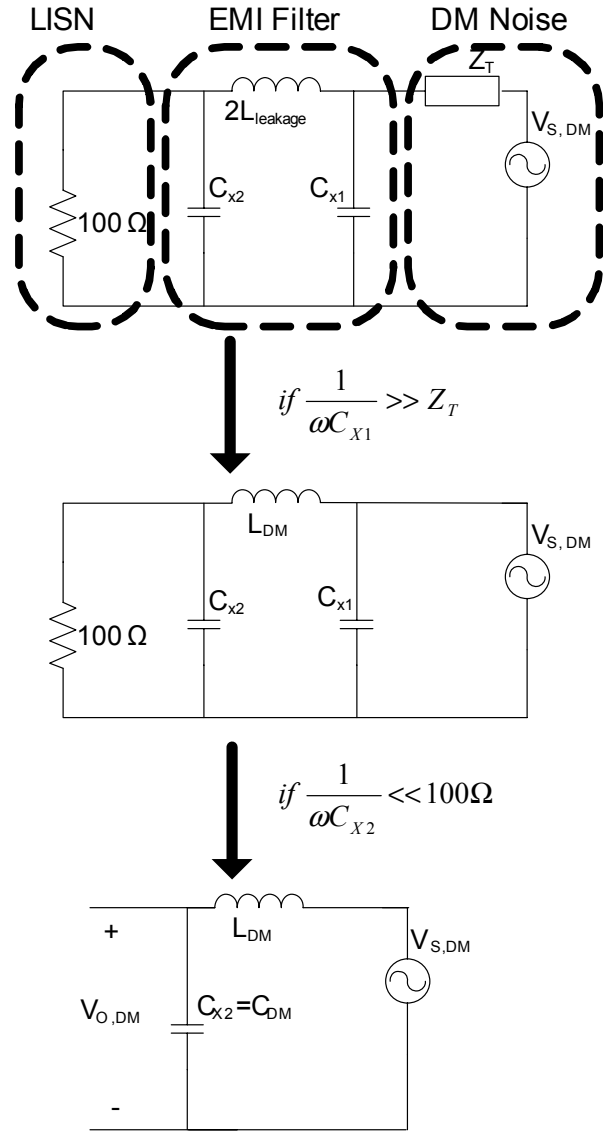


Fig. 3-6: Equivalent circuit for the derivation of DM filter attenuation

From this example the differential mode attenuation is given by:

$$DM \text{ attenuation} \approx \frac{v_{LISN(\text{without filter})}}{v_{LISN(\text{with filter})}} \approx \frac{V_{S_DM(100\Omega)}}{V_{O_DM(100\Omega)}}$$

$$\frac{V_{S_DM(100\Omega)}}{V_{O_DM(100\Omega)}} = \frac{Z_{C_{DM}} + Z_{L_{DM}}}{Z_{C_{DM}}} = 1 + j^2 \omega^2 L_{DM} C_{DM} \quad (3-2)$$

$$f_{DM} \approx \frac{1}{2\pi\sqrt{L_{DM} C_{DM}}} \text{ with } C_{DM} = C_{x1} = C_{x2} \text{ and } L_{DM} = 2L_{leakage}$$

It is important to mention that in this case the theoretical attenuation from capacitor C_{x1} is insignificant however since the real noise source impedance is not known, it is preferable to keep it. For the design process the DM attenuation is assumed to be 40dB/dec to meet the low-frequency standard. However, a higher attenuation could be expected (up to 60dB/dec) and consequently the value of the DM capacitors will be adjusted to decrease the filter size.

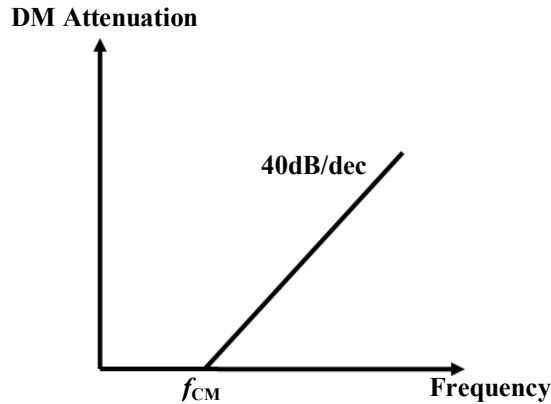


Fig. 3-7: Differential Mode noise filter theoretical attenuation

In the previous case the impedance Z_T is assumed low, however if it is considered high, the same procedure could be made and the corner frequency is finally found to be (3-3). However, since the real impedance it is not know, the first case is kept for the baseline filter and the capacitance value will be adjusted

$$f_{DM} \approx \frac{1}{2\pi\sqrt{L_{DM}\frac{C_{DM}}{2}}} \text{ with } C_{DM} = C_{x1} = C_{x2} \text{ and } L_{DM} = 2L_{leakage} \quad (3-3)$$

Now that the relations have been defined, the next step is to find the corner frequency for both CM and DM noise. When these frequencies are known, the components' value can be determined and the filter can be designed. Note that this procedure is used to meet the low-frequency specification while, if needed, it could be modified to meet the high-frequency specification after the design is built and tested.

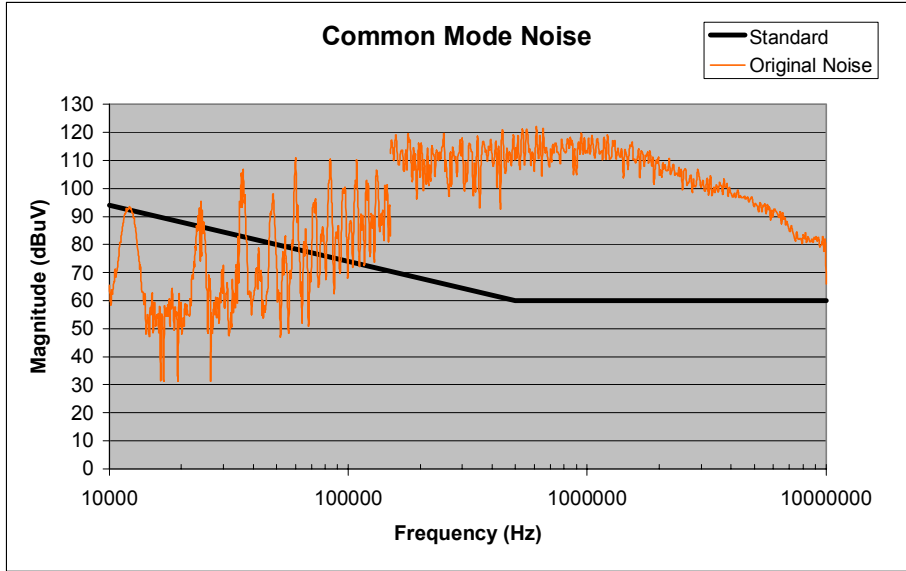


Fig. 3-8: Original CM noise

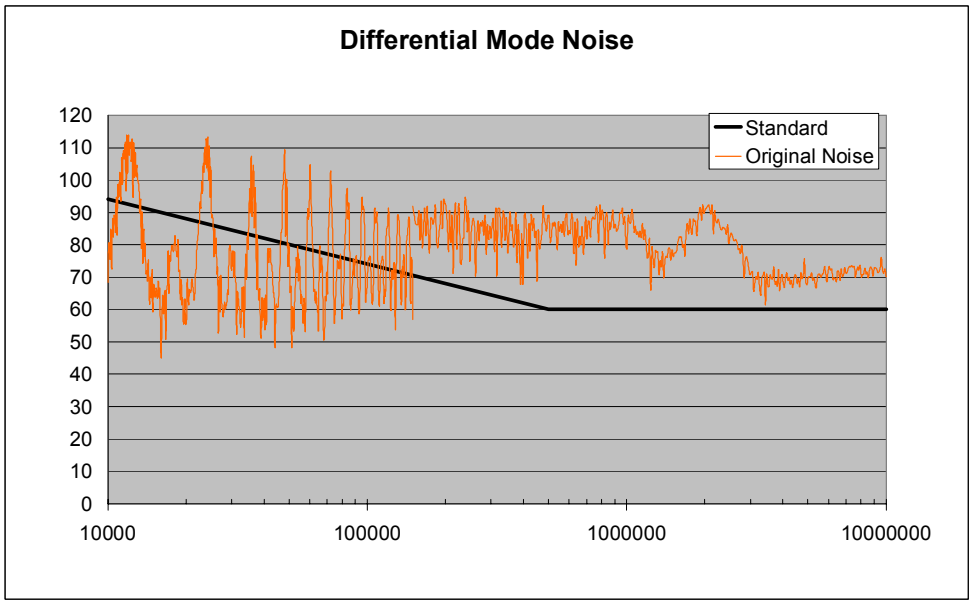


Fig. 3-9: Original DM noise

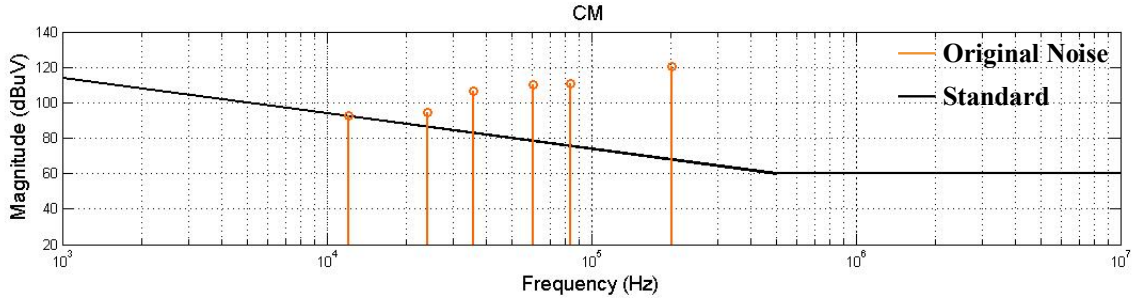


Fig. 3-10: High harmonics for the original CM noise

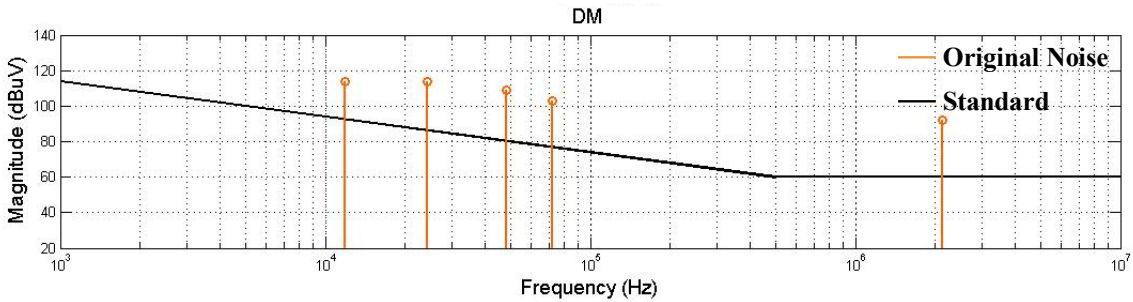


Fig. 3-11: High harmonics for the original DM noise

From the original CM and DM noise (cf Fig. 3-8 & Fig. 3-9) measured with the noise separator and following Fig. 2-6 and Fig. 2-13, the highest peak harmonics are plotted separately with the EMI standard as shown in Fig. 3-10 and Fig. 3-11. The required attenuation for the CM and DM filter is therefore calculated from (3-4) for the main harmonics. Some margin is added to compensate for the measurement from the noise separator (cf. Fig. 3-12 & Fig. 3-13).

$$\begin{aligned}
 (V_{attenuation_required_CM})_{dB} &= (V_{original_CM})_{dB} - (V_{standard})_{dB} + 6dB \\
 (V_{attenuation_required_DM})_{dB} &= (V_{original_DM})_{dB} - (V_{standard})_{dB} + 6dB
 \end{aligned}
 \tag{3-4}$$

Fig. 3-12 and Fig. 3-13 summarize the process. The green curve represents the difference between the noise and the standard, while the pink dots are the final required attenuation when the margin is applied. Finally, the corner frequency is simply found by drawing a 40 dB/dec slope line that is tangent to the required CM or DM attenuation and crosses the 0 dB axis or using the formula given in (3-5). It is important to mention that the first switching harmonic (here 12 kHz) might not be the more stringent to attenuate. For example, in the case of the CM, it is clear that the third switching harmonics is the

highest and will determine the corner frequency while for the DM the most severe is the first one.

$$f_{CM \text{ or } DM} = \frac{f_{\text{at max harmonic amplitude}}}{10 \frac{\text{max amplitude}}{\text{attenuation}}} \quad (3-5)$$

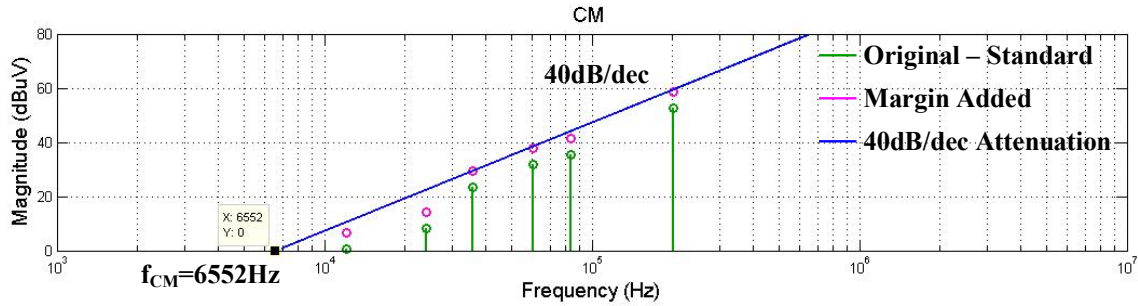


Fig. 3-12: Required CM attenuation and corner frequency

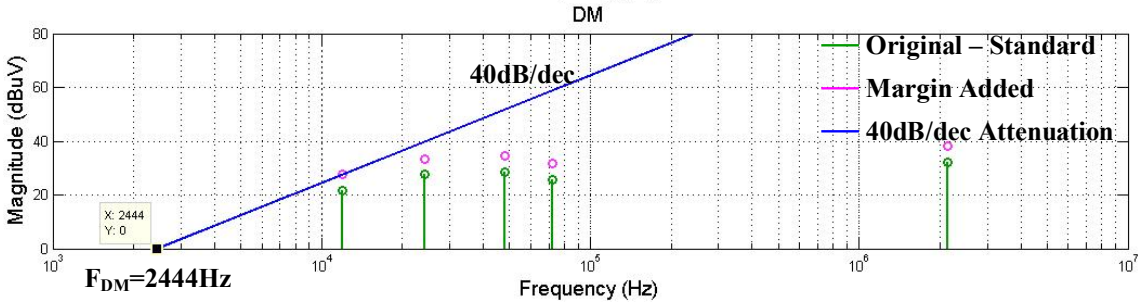


Fig. 3-13: Required DM attenuation and corner frequency

When both corner frequencies are known, the inductor and capacitor parameter values are determined. By taking a close look at (3-1) and (3-2), we see that we must determine one value to get the other value. It is preferable to design the CM parameters first by simply picking the maximum capacitance allowed by the standard to reduce total size; in this case 100nF per line as stated above. Therefore, the necessary CM choke inductance is calculated. As far as the DM parameters are concerned, some freedom exists between the DM capacitor (C_{X1} & C_{X2}) and the value of L_{DM} . Increasing L_{DM} will obviously reduce the size of the DM capacitors and vice versa. Moreover, the DM inductance generally uses the leakage from the CM choke which can be roughly approximated to be between 0.1 to 2% of the CM choke value depending on the core material. If it is preferable to increase the value of the DM inductance to reduce the size of the DM capacitors, separate DM inductance could be added in the design.

If the same procedure is applied to our design, the following parameters can be calculated.

$$f_{CM} \approx \frac{1}{2\pi\sqrt{L_{CM}C_{CM}}} = 6552Hz$$

with $C_{CM} = 2C_y = 200nF \rightarrow L_{CM} \approx 3mH$

(3-6)

$$L_{DM} = 1\%L_{CM} \approx 30\mu H$$

$$f_{DM} \approx \frac{1}{2\pi\sqrt{L_{DM}C_{DM}}} = 2444Hz \rightarrow C_{DM} = C_{X1} = C_{X2} = 141\mu F$$

The equivalent baseline filter with the corresponding parameters is given in Fig. 3-14.

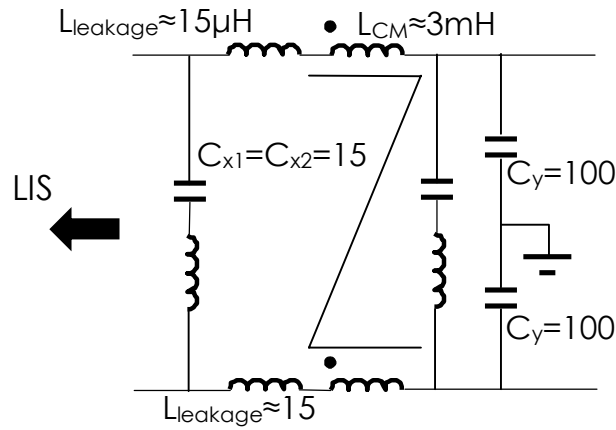


Fig. 3-14: Equivalent baseline filter

III. Material Consideration for Baseline Filter

The common choke is generally made with a toroidal core with a ferrite type of magnetic structure. This gives good results for the frequency desired for EMI and it is pretty inexpensive. It's common for the line inductor to wind the toroidal core with only one layer to reduce the EPC which is the case for the first version of the baseline filter. Later on, other versions will increase the number of winding layer to utilize the window of the core. The ferrite cores used in this research have been provided by Magnetics, which offers a large range of ferrite materials with varying permeability, as shown in Fig. 3-15 as reported in [38].

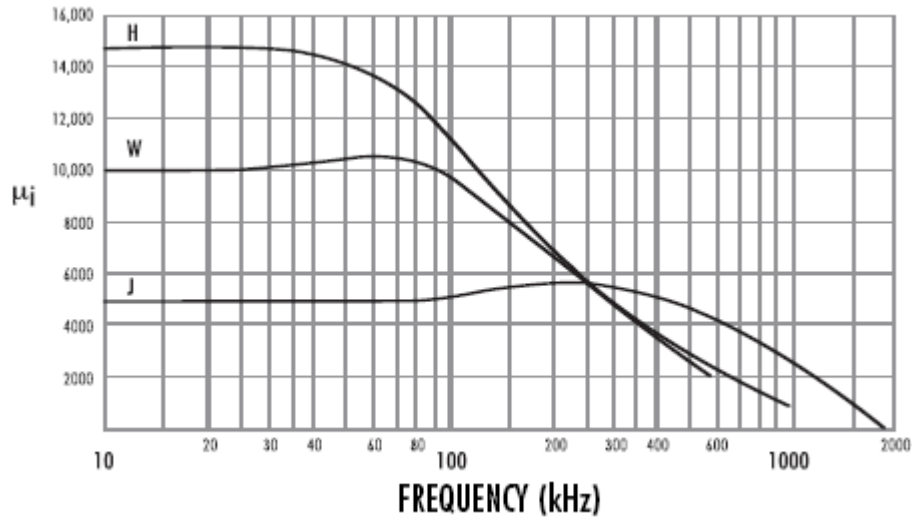


Fig. 3-15: Permeability of ferrite core

For EMI applications, the “J” type material is often used as a compromise between a high permeability at low frequency and a possible saturation of the core. At the end of this chapter, another technology, the nano-crystalline magnetic material is tested and compared to ferrite. It provides a much higher permeability at low frequency which helps to reduce the total volume of the choke while the saturation flux density is increased threefold. The material used generally for the DM inductor is either iron powder or Kool M μ [39]. Both of them have a small permeability to avoid saturation and tend to have a large amount of loss at high frequency to reduce the noise.

A tremendous number of capacitors are available on the market and mainly differ by their performance over different frequencies and their different maximum rating voltages. For the CM capacitor, as stated in the standard, the maximum value is 100nF per line and the voltage rating should be higher than 200V. The capacitor’s behavior is generally capacitive until the resonance point, and then it becomes inductive due to the equivalent series inductor (ESL). It is important to push this resonance point as high as possible to increase the performance of the filter. From that point of view, film or ceramic capacitors are generally preferred, with the favorite being “X7R” ceramic capacitor, which has a much smaller volume than film capacitors, as shown in Fig. 3-16, and slightly better behavior at high frequencies as shown in Fig. 3-17 and Fig. 3-18. These last two figures

represent the Agilent impedance analyzer's impedance measurement of the TDK 100nF (630V) ceramic capacitor and Philips 100nF film capacitor (630V).

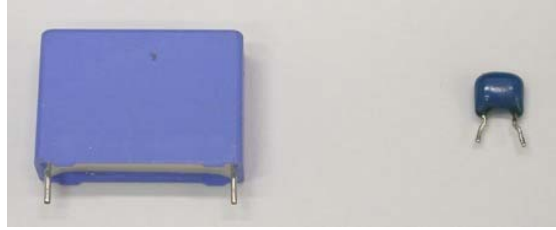


Fig. 3-16: Size representation of film (left) and ceramic (right) capacitors for CM filter

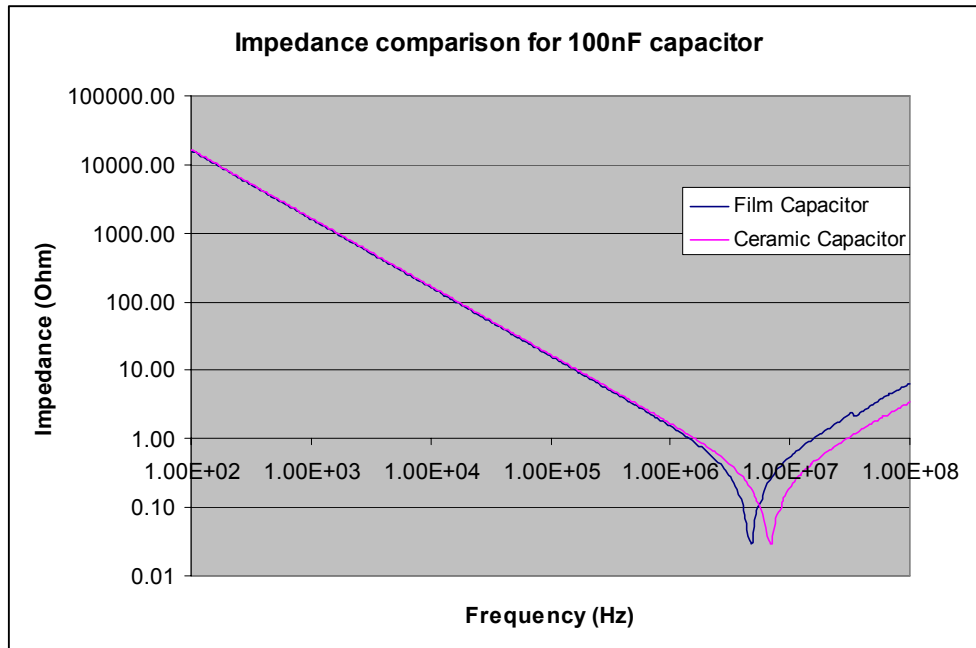


Fig. 3-17: Impedance of 100nF film and ceramic CM capacitor

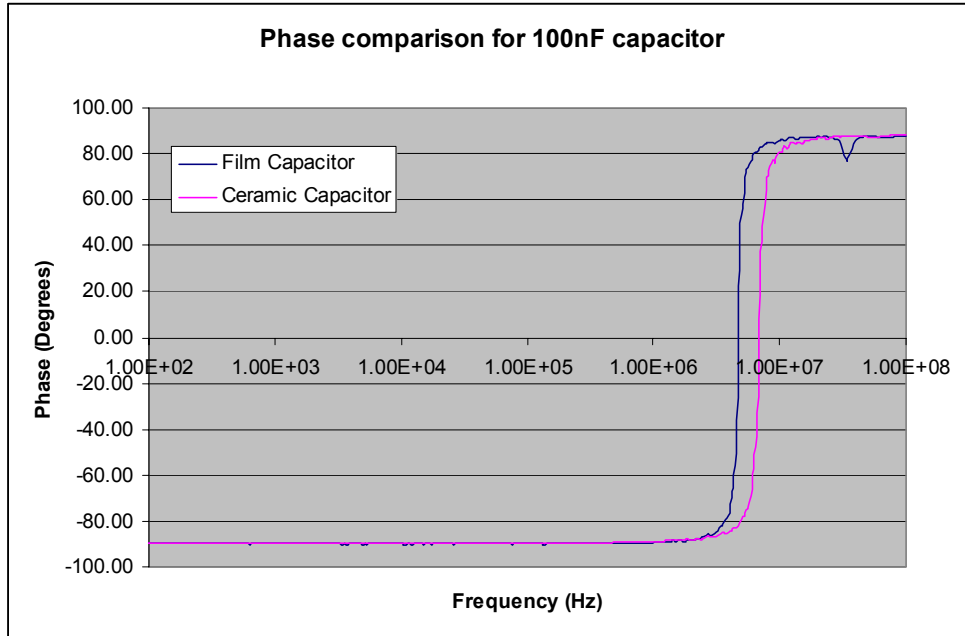


Fig. 3-18: Phase of 100nF film and ceramic CM capacitor

The filter uses electrolytic DM capacitor even though its performance is not good for high frequency, as illustrated in Fig. 3-19. The capacitor behavior is generally capacitive until the tens of kilohertz range, and then become resistive and finally inductive after one or two megahertz. The DM capacitance is generally high, approaching 33 μF in the last filter version which is difficult to find in film or ceramic capacitor especially for a high rating voltage. Some multilayer ceramic capacitors which have better performance (cf. Fig. 3-19) however exist [40] but their size is much bigger compared to the electrolytic type. Moreover as shown on the last chapter their capacitance is in function of the voltage which is not appropriate for this application. Fig. 3-20 shows a representation of the 33 μF capacitor for both electrolytic and ceramic capacitors. The cost is also another factor to take into consideration, since the price for multilayer ceramic capacitor is more than 240 times the price for an electrolytic capacitor, at \$1 for an electrolytic and \$240 for a multilayer capacitor.

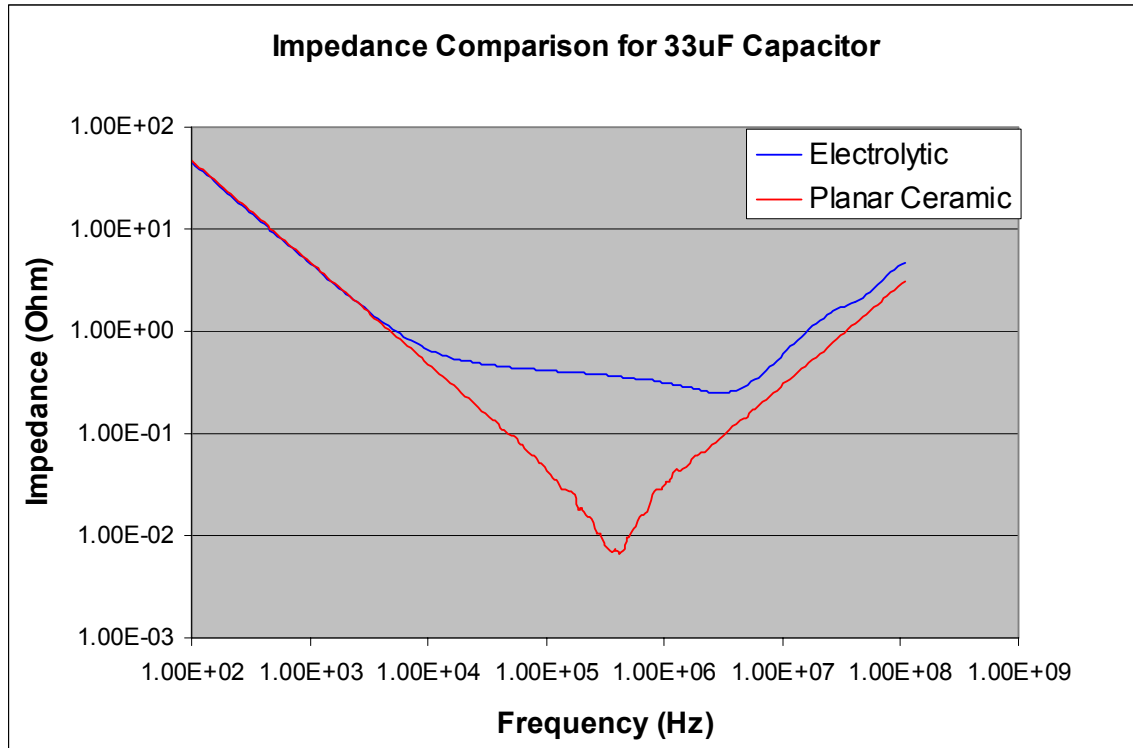


Fig. 3-19: Impedance of 33μF electrolytic and ceramic DM capacitor

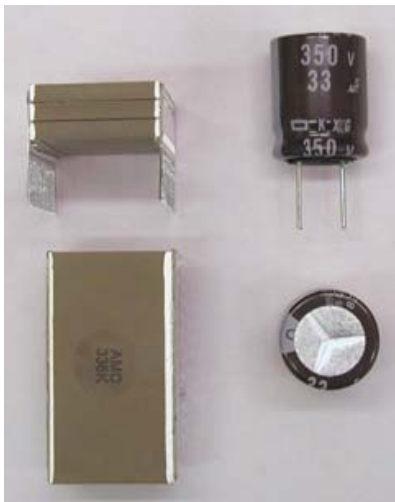


Fig. 3-20: Size representation of electrolytic (right) and ceramic (left) capacitors for DM filter

IV. Preliminary Design of CM choke

The baseline design of the CM choke has been made by following the design example in [24]; later on some improvements will be made to take more parameters into account and to reduce its size. The first parameter that needs to be set is the wire size. If the

current is supposed to be 8 A, the wire area and therefore the gauge of the wire could be found by assuming a current density and reading Table 3-1. If we follow (3-7) and assume the current density to be 4 A/mm², then the gauge of wire required is AWG#14.

$$A(\text{cm}^2) = \frac{I(\text{A})}{J(\text{A/cm}^2)} = \frac{8}{4} = 2\text{mm}^2 \quad (3-7)$$

Table 3-1: Table of AWG wire sizes

AWG Gauge	Conductor Diameter (mm)	Conductor Area (mm ²)
14	1.628	2.08
15	1.450	1.65
16	1.291	1.31
17	1.150	1.04
18	1.024	0.823
19	0.912	0.653
20	0.812	0.518
21	0.723	0.410
22	0.644	0.326

The next step is to choose a core size and material depending on the number of turns needed. This part is an iterative process, since the chosen core may not allow enough space to wind the total number of turns. The “J” type of ferrite core, number J-44916TC, is used for the baseline design to achieve the number of turns required to get an inductance of 3mH. The winding used for the baseline CM choke is a single-layer structure. The main equations used to determine all the parameters are given below, and they provide a method for determining the inner circumference of the core (I.C), the maximum number of turns possible (N_{\max}), and the required number of turns for the design (N_{required}). σ_{winding} represents the maximum angle that the winding subtends on half of the core. It is common to assume 160° to allow some margin, as shown in Fig. 3-21.

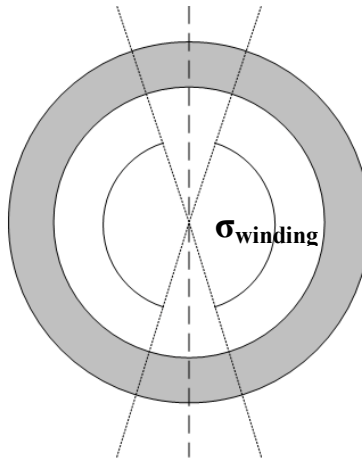


Fig. 3-21: Winding angle example

$$I.C = \pi(D_{core} - D_{wire})$$

$$N_{max} = \frac{\sigma_{winding}}{360^\circ} \frac{I.C}{D_{wire}}$$

$$N_{required} = 1000 \sqrt{\frac{L_{CM}}{A_L}}$$

(3-8)

$$N_{required} \leq N_{max}$$

With :

A_L : inductance factor (mH/1000 turns)

L_{CM} : CM inductance (mH)

If the formulas in (3-8) are applied to the previous design, then the required number of turn is 23 turns for each side.

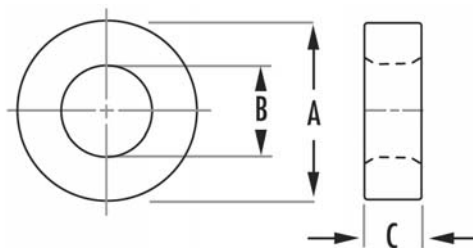


Fig. 3-22: Magnetics core size definition

Table 3-2: Magnetic core size

Core Type	A (O.D.) mm	B (I.D.) mm	C (Height) mm	A_L ($\pm 20\%$) mH/100T
-----------	-------------	-------------	---------------	------------------------------

J-44916TC	50.2	32.7	16.6	5900
-----------	------	------	------	------

$$I.C = \pi(D_{inner\ core} - D_{wire}) = \pi(32.7 - 1.628) = 97.6\text{mm}$$

$$N_{\max} = \frac{\sigma_{winding}}{360^\circ} \frac{I.C}{D_{wire}} = \frac{160^\circ}{360^\circ} \frac{97.6}{1.628} = 26.6 \Rightarrow 26\text{Turns}$$

$$N_{required} = 1000 \sqrt{\frac{L_{CM}}{A_L}} = 1000 \sqrt{\frac{3}{5900}} = 22.54 \Rightarrow 23\text{Turns}$$

(3-9)

$N_{required} \leq N_{\max}$ is verified

V. EMI Filter Modeling

Even though the complete circuit's characteristics and impedance are not known, it is important to have a basic representation of the filter that could be used in any simulation model. The goal is not to predict the behavior of the choke or filter before designing it, but to verify the comportment and help to evaluate the high-frequency parasitic after the filter is built. The CM choke modeling follows the technique used in [41] where a high-frequency model is analyzed based on measurements.

A. Common Mode Choke

The equivalent circuit used to model the CM choke represented in Fig. 3-23 takes into account the CM and leakage inductances and the parasitic capacitances that will impact the high-frequency characteristics. The parameter C_1 defines the capacitance in the windings and is generally called EPC, while C_2 is the capacitance between windings. Finally, the core resistance R_m replicates the energy loss of the ferrite core due to hysteresis and eddy current. The model is assumed to be slightly different than it is represented on paper, and the comportment is approximated until 10 MHz.

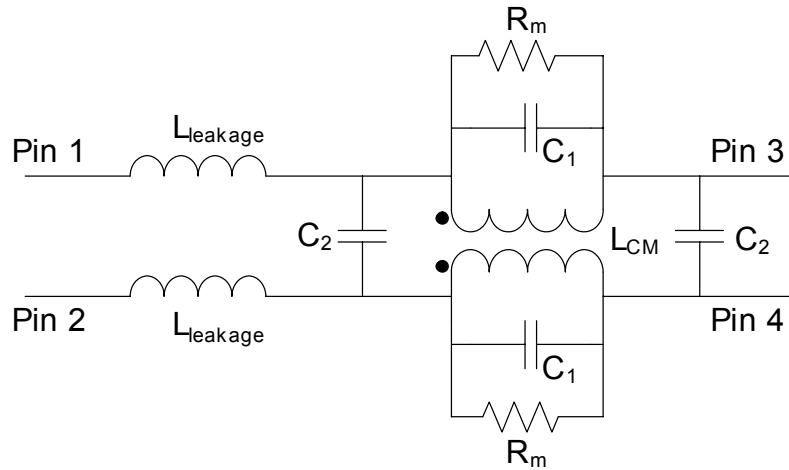


Fig. 3-23: Equivalent circuit of CM inductor

The first measurement used to help to determine the value of parameters L_{CM} , C_1 and R_m consists of shorting pins 1 and 2 together and shorting pins 3 and 4 and measuring across them. By doing so, the equivalent circuit shown in Fig. 3-24 could be derived. The impedance measurement is shown in Fig. 3-25 and represents low-frequency inductance behavior, while its behavior during high frequencies is more capacitive.

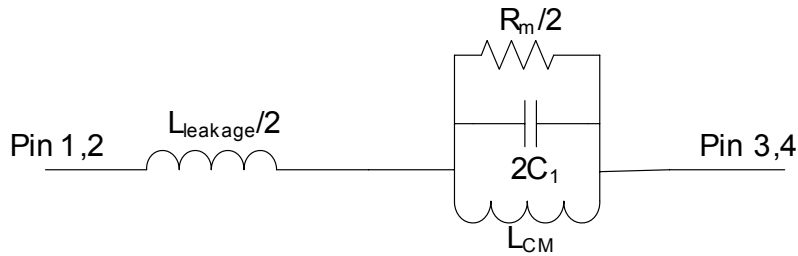


Fig. 3-24: Equivalent circuit of measurement 1

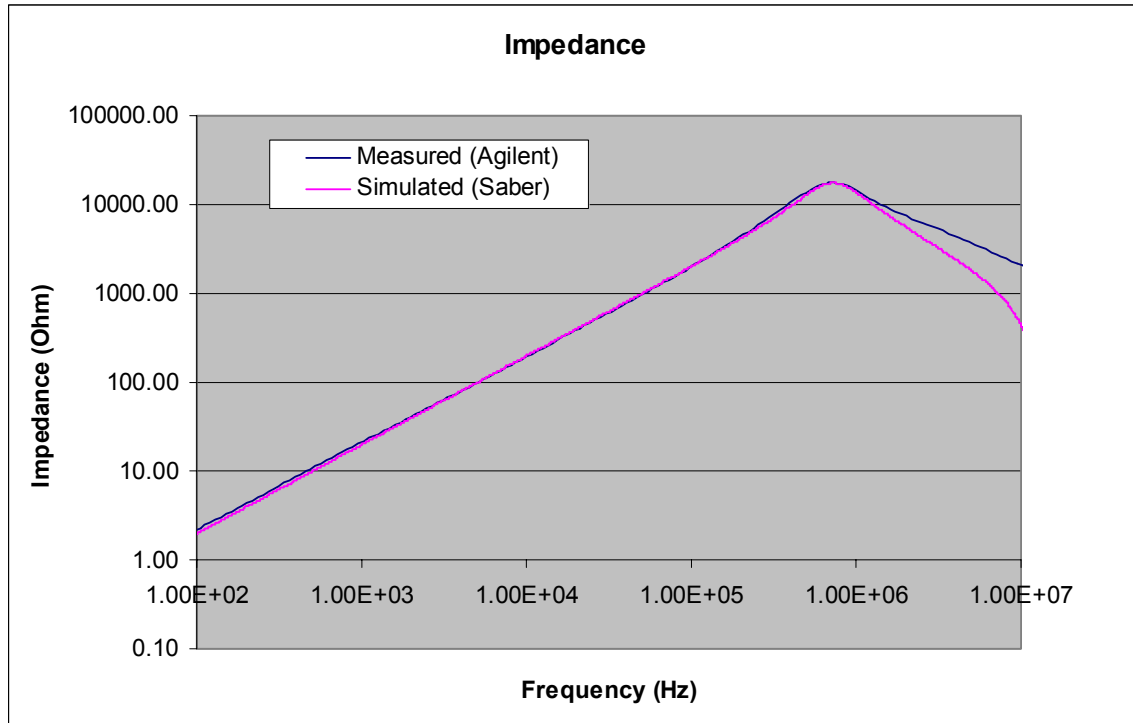


Fig. 3-25: Impedance for measurement 1

Since the leakage inductance is much smaller than the CM inductance, it can be neglected and the equivalent CM choke inductance is derived according the impedance at low frequency.

$$L_{CM} \approx \frac{|Z|}{2\pi f} \Bigg|_{f=low\ frequency} = \frac{|100.6|}{2\pi 5000} \Bigg|_{f=5kHz} \approx 3.2mH \quad (3-10)$$

The parameter C_1 is extracted at the resonance.

$$2C_1 \approx \frac{1}{4\pi^2 L_{CM} f^2} \Bigg|_{f=resonance} \leftrightarrow C_1 \approx \frac{1}{2 \cdot 4\pi^2 L_{CM} f^2} \Bigg|_{f=resonance} = 7.65 pF \quad (3-11)$$

The core resistance is found by a curve fitting method at different frequency range and could be approximated at the resonance frequency between $2C_1$ and L_{CM} .

The second measurement approximates the leakage inductance. The measurement is made by shorting pins 1 and 3 and measuring across pins 2 and 4. The equivalent circuit

Show Desktop.scf and impedance measurement are shown in Fig. 3-26 and Fig. 3-27, respectively.

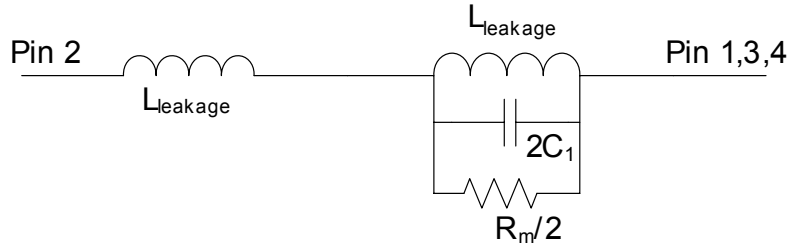


Fig. 3-26: Equivalent circuit of measurement 2

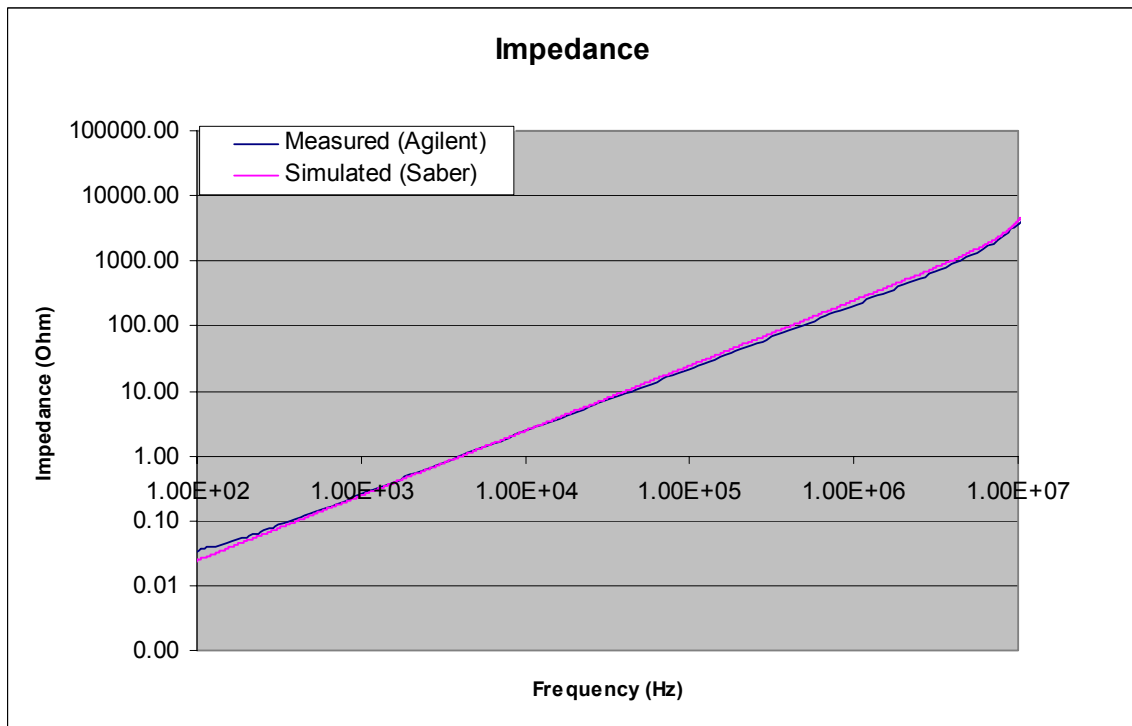


Fig. 3-27: Impedance for measurement 2

The impedance measurement demonstrates an inductive comportment until 10MHz, where the leakage inductance can be calculated.

$$L_{leakage} \approx \frac{1}{2} \frac{|Z|}{2\pi f} \Bigg|_{f=low\ frequency} = \frac{|1.22|}{4\pi 5000} \Bigg|_{f=5kHz} = 19.4\mu H \quad (3-12)$$

The final measurement allows the characterization of parameter C_2 and concludes on the model analysis. The measurement is taken by letting pins 3 and 4 open while measuring the impedance between pins 1 and 2. The equivalent circuit and impedance measurement are shown in Fig. 3-28 and Fig. 3-29, respectively.

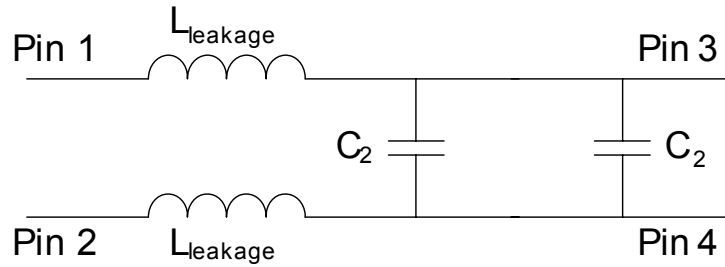


Fig. 3-28: Equivalent circuit of measurement 3

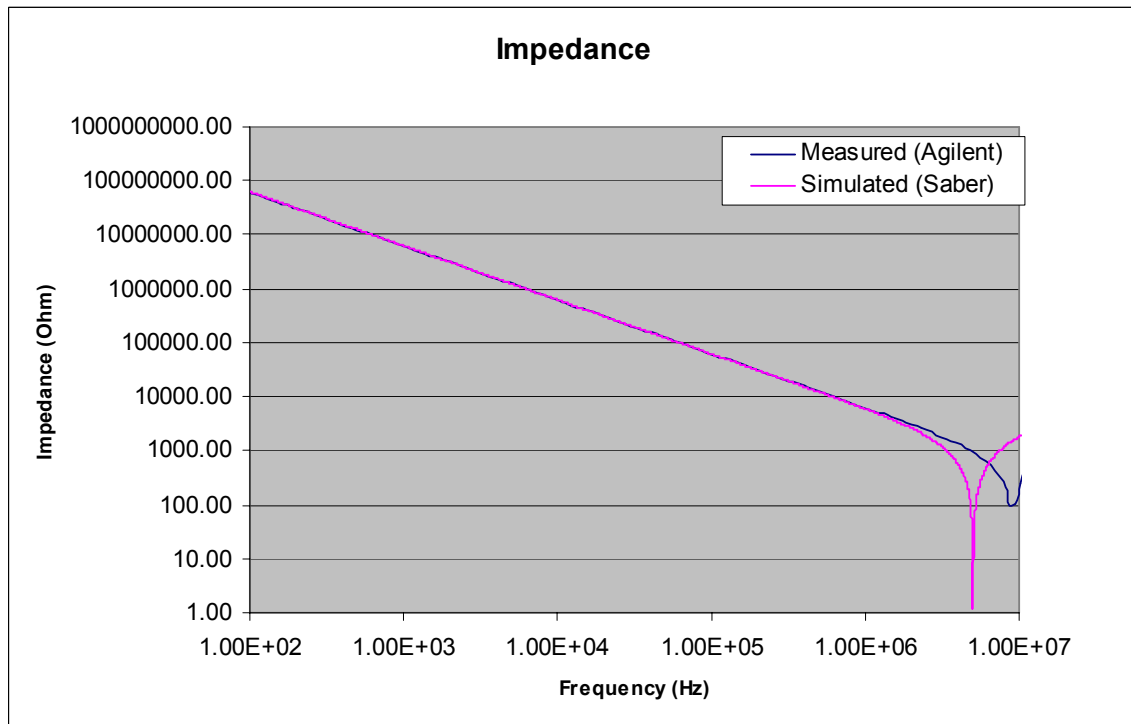


Fig. 3-29: Impedance for measurement 3

The behavior of the result is capacitive through almost the entirety of the frequency range. The parasitic parameters C_2 could be derived by following:

$$C_2 \approx \frac{1}{2} \frac{1}{2\pi f |Z|} \Bigg|_{f=\text{medium frequency}} = \frac{1}{4\pi \times 10^6 \times 6220} \Bigg|_{f=1\text{MHz}} = 12.8 \text{ pF} \quad (3-13)$$

Almost all simulated values for the model match with the measurement; only Test 3 is faintly different at high frequency due to the behavior of the leakage at that frequency. The final equivalent model, including all the parameters's, value is shown in Fig. 3-30. It

is important to mention that the total leakage is higher than previously assumed, which should help the DM noise.

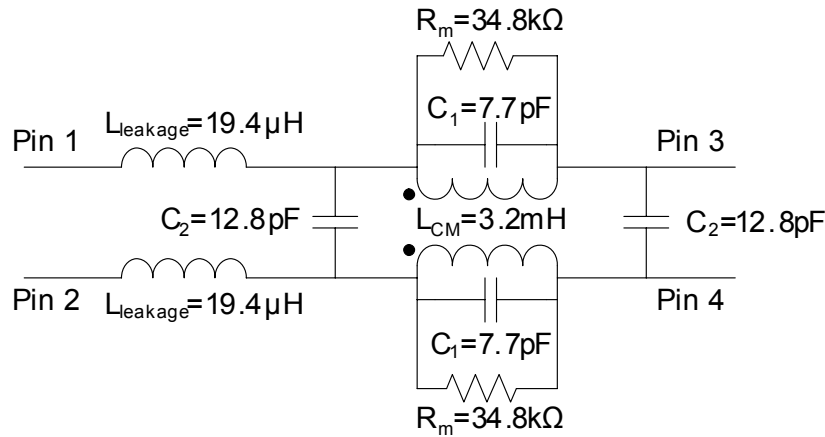


Fig. 3-30: Equivalent circuit of CM inductor with parasitics value

B. CM and DM Capacitor

The model used to represent the low and high frequency behavior of the capacitors is simply a RLC circuit in series. The parameters are either calculated to fit the impedance measurement, or curve matching from the impedance analyzer could be used. The model and impedance for the CM capacitor are shown in Fig. 3-31 and Fig. 3-32, respectively. The DM circuit and impedance are shown in Fig. 3-33 and Fig. 3-34.

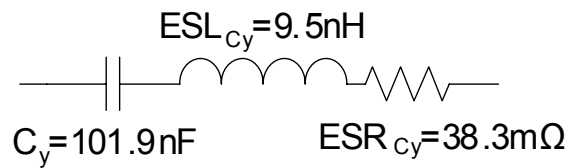


Fig. 3-31: Equivalent model for the 100nF CM capacitor

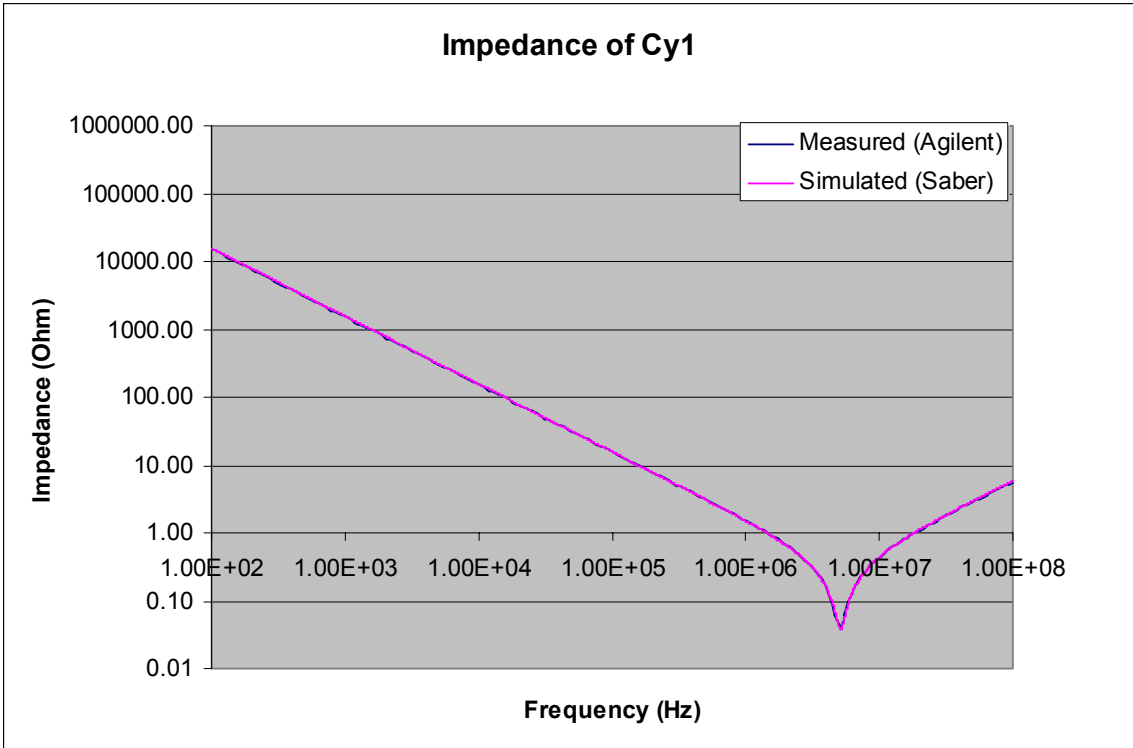


Fig. 3-32: Impedance of the 100nF CM capacitor

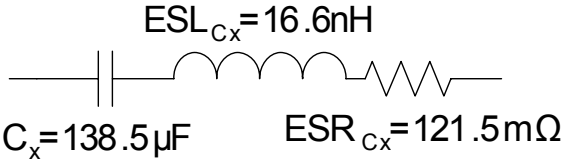


Fig. 3-33: Equivalent model for the 150µF DM capacitor

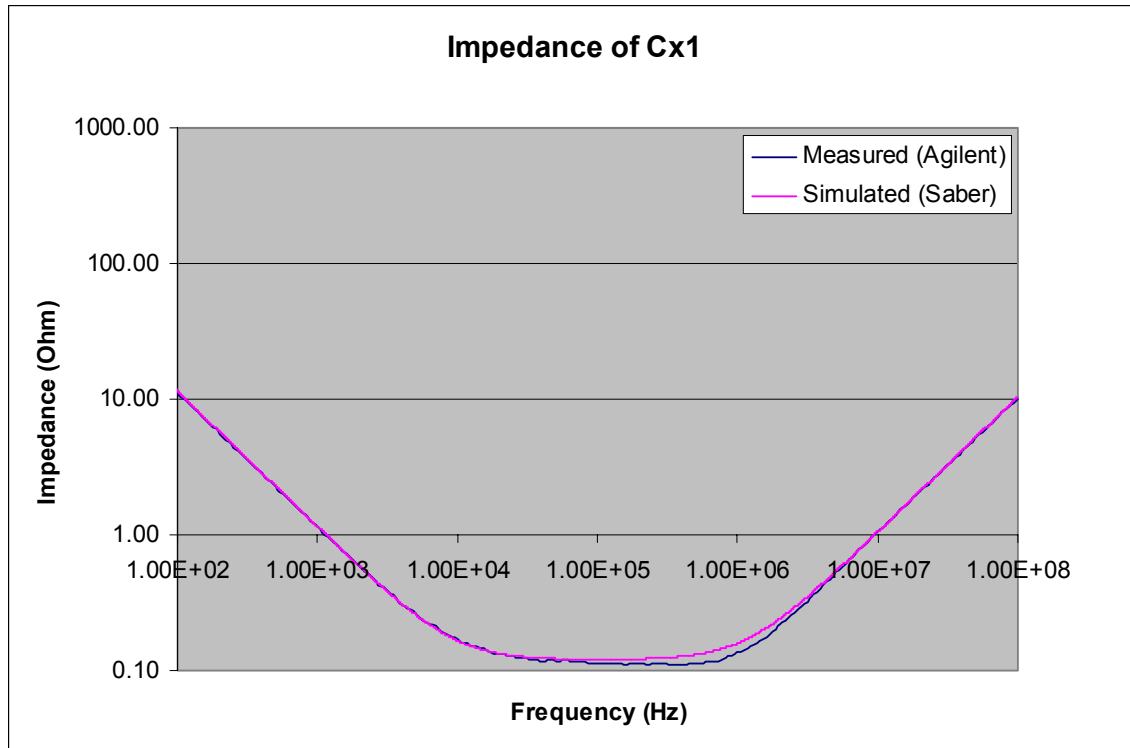


Fig. 3-34: Impedance of the 150 μ F DM capacitor

It is clear that the equivalent circuit models both low and high frequency compoment and could be used to model the entire filter.

C. Filter

If the coupling between components is not taken into account, the entire filter can be modeled by combining together all the previous equivalent circuits. A good way to look at the integrity of this model is to compare the insertion gain from simulation software with the small-signal test of the filter. The definition of insertion gain is the voltage across a 50 Ω resistor when the filter is inserted, divided by the voltage across the 50 Ω resistor when no filter is used, as shown in Fig. 3-35.

$$I.G = \frac{V_{50\Omega_w/ \text{filter}}}{V_{50\Omega_w/o \text{ filter}}} \quad (3-14)$$

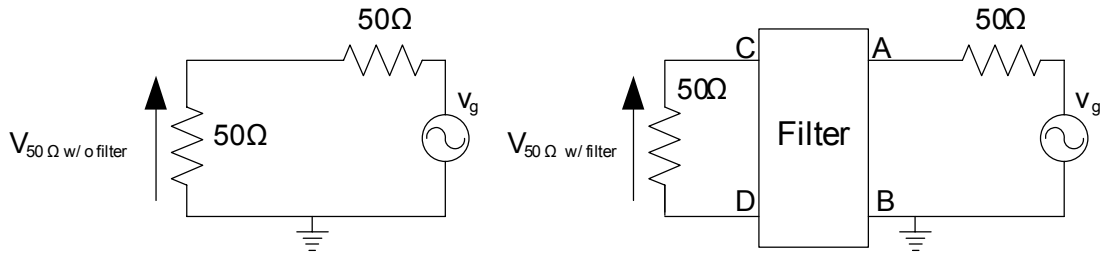


Fig. 3-35: Insertion gain definition

Furthermore, some manipulation and extra equipment are needed to measure the CM or DM insertion gain. For instance, in order to measure the CM insertion gain, filter inputs 1 and 2 need to be connected together while outputs 3 and 4 are also connected. Therefore, the filter is added by connecting inputs 1 and 2 to A, outputs 3 and 4 to C and ground to B and D, as in Fig. 3-36. The DM on the other side is trickier since a transformer had to be used to isolate the filter since no ground is wanted in the measurement. The transformer used in the experiment is the FTB-1-6 model, which has an unbalanced input and balanced output and a bandwidth from 0.01 to 125 MHz. Therefore, the equivalent circuit used to measure the DM insertion gain is that given in Fig. 3-37.

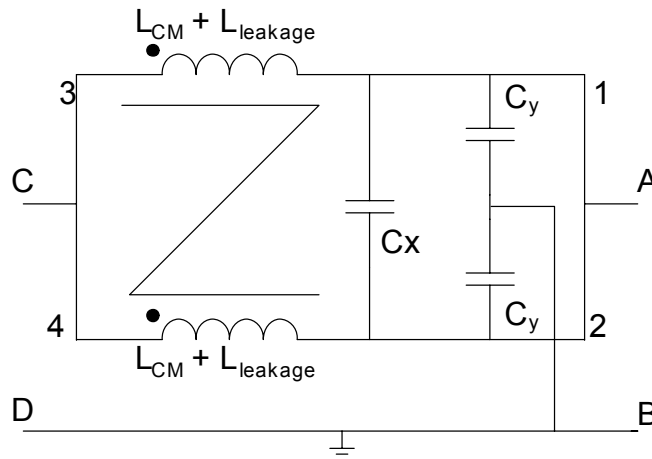


Fig. 3-36: CM insertion gain equivalent circuit

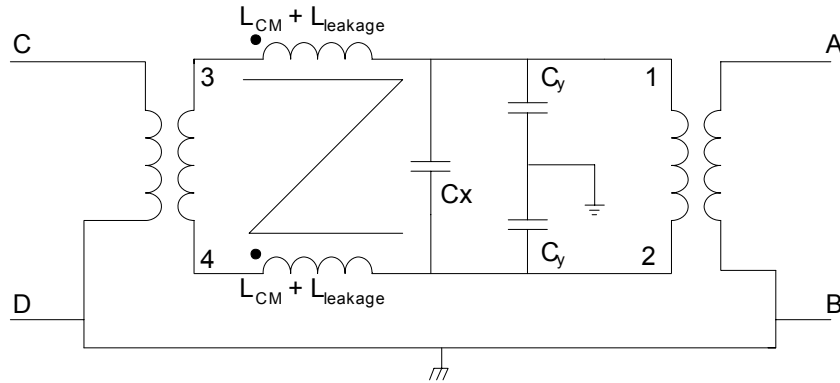


Fig. 3-37: DM insertion gain equivalent circuit

D. Insertion Gain Comparison for Both CM & DM

If the simulation models shown in Fig. 3-35, Fig. 3-36 and Fig. 3-37 are combined, the CM and DM insertion gain can be predicted. The goal is to compare the predicted value with the real measurement extracted with the Agilent 4395A network analyzer.

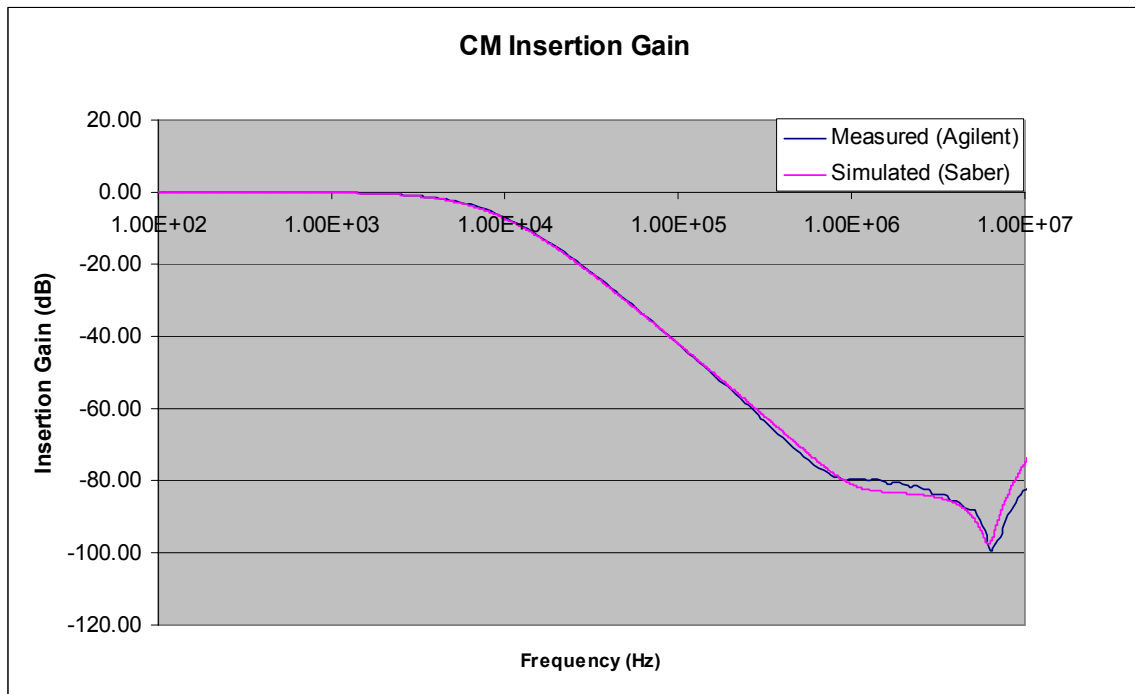


Fig. 3-38: Simulated and measured CM insertion gain

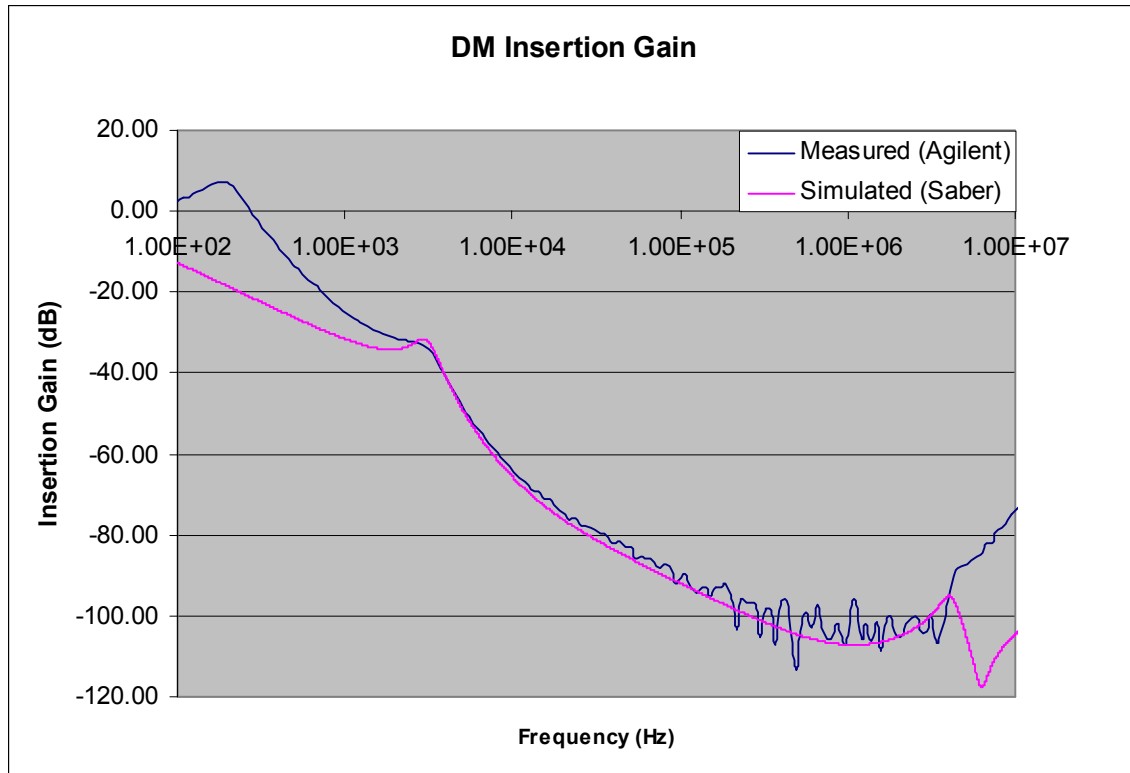


Fig. 3-39: Simulated and measured DM insertion gain

The simulated result is really close to the measured value for the CM; only some tiny discrepancies are noticed at high frequencies due to PCB connections. This could be easily adjusted by adding small inductances to model these connections. On the other hand, the DM matches only after 3 kHz due to the measurement transformer which has a starting frequency that is too high. For this research the frequency of interest is from 10 kHz to 10 MHz, so the transformer is sufficient.

VI. Baseline Filter Large Signal Measurement

Now that the predicted and measured small-signal insertion gains have been verified, the next step is to look at the large-signal test and identify the real EMI reduction from the filter. The CM and DM large-signal results are shown in Fig. 3-40 and Fig. 3-41, respectively.

Common Mode Noise

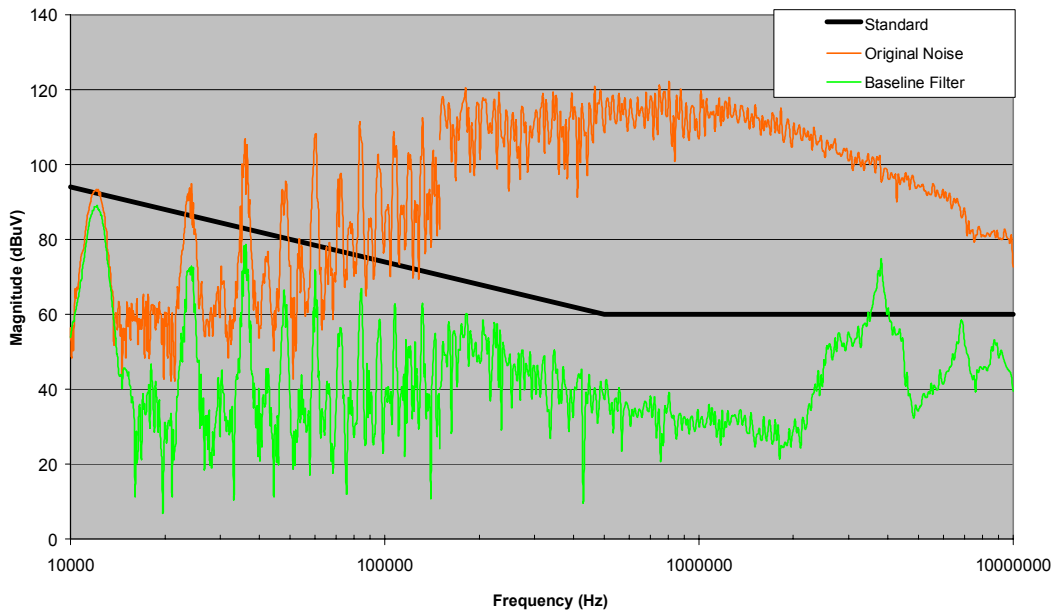


Fig. 3-40: Large signal CM EMI noise

Differential Mode Noise

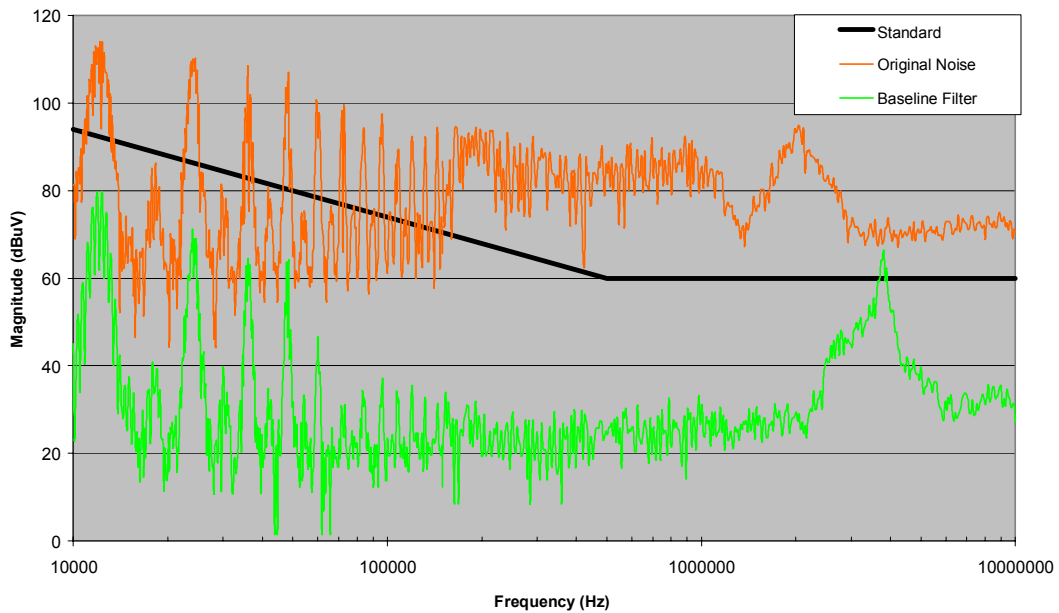


Fig. 3-41: Large signal DM EMI noise

It is clear that the filter contributes to reduction of both the low and high frequencies. The attenuated noise almost meets the basic EMI standard (given for 28 V) at all frequencies except at 3.8 MHz, where a resonance between the input impedance of the

drive and the EMI filter occurs. It is important to notice that the low-frequency attenuation of the DM is really high due to a higher leakage and higher attenuation slope; therefore the values of the DM capacitors will be adjusted.

From these measurements the real attenuation is derived by subtracting the attenuated noise from the original noise. The CM large-signal attenuation is pretty close to the insertion gain until 2 MHz, when the resonance occurs and spoils the result. On the other side, the DM large-signal attenuation is pretty far from the measured insertion gain, which could be due to the impedance of the real system. It is important to understand that the insertion gain is only given for a 50 Ω input and output impedance which is completely different from the real case. Modeling using this measurement is just a tool to understand the behavior between different filters, and won't accurately predict the real attenuation when the filter is added to the system.

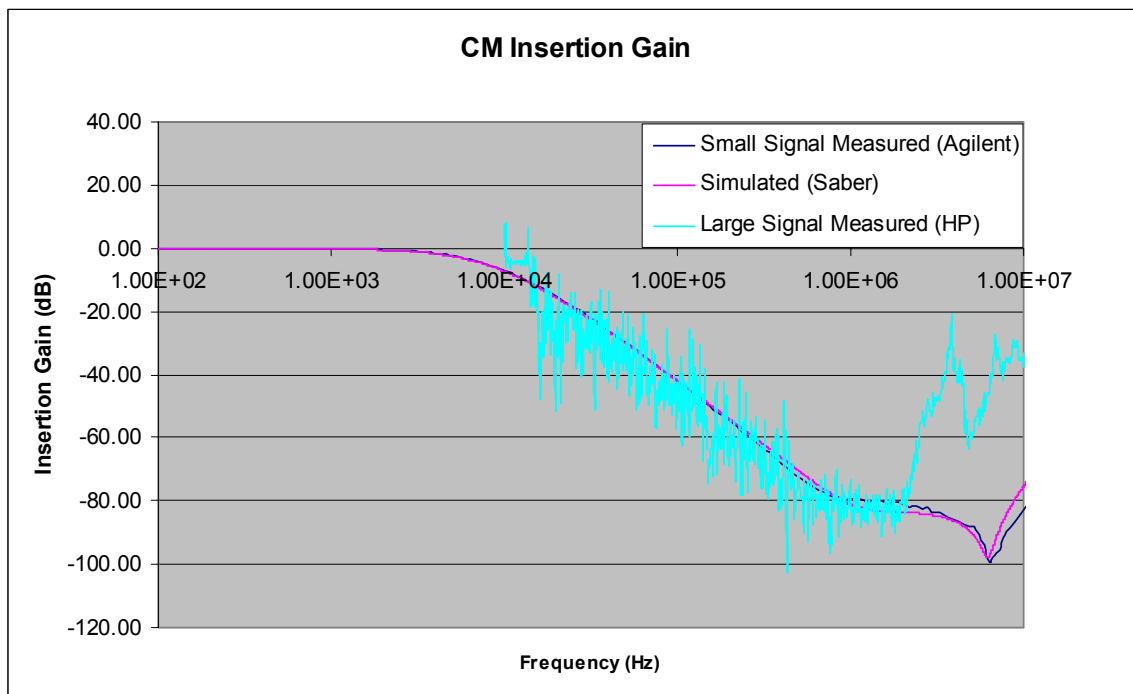


Fig. 3-42: Small and large signal CM EMI noise

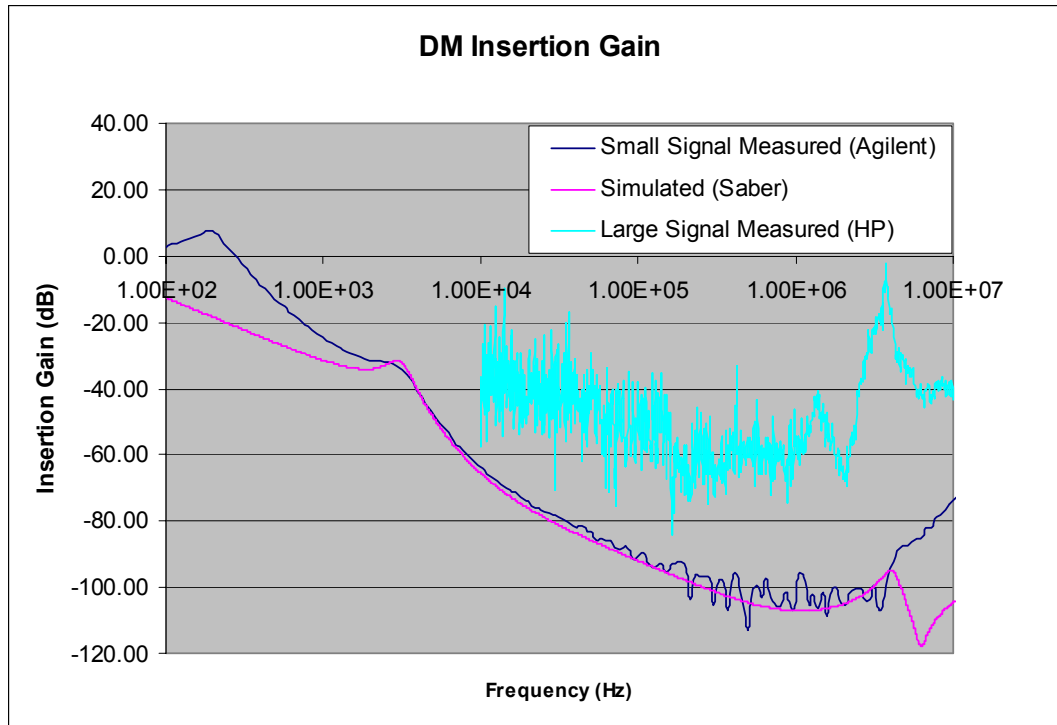


Fig. 3-43: Small and large signal DM EMI noise

VII. Baseline Filter Size

It is important to look at the size of the baseline filter since the goal is to minimize its size by improving or keeping the same performance. The current size as shown in picture Fig. 3-44 is pretty big at 197.5 cm³ as defined by a length of 9.5 cm, a width of 5.8 cm and a height of 3.7 cm. the length only take into account the distance between the two DM capacitor since the PCB board had to be change during experiments.



Fig. 3-44: Baseline filter picture

VIII. Summary

A simple procedure has been shown to derive the corner frequencies and components' values based on experimental original results. The filter is composed of basic high-frequency components and a preliminary design for the CM choke is employed. A simple circuit of the filter is obtained by modeling each component independently and reordering all of them. Finally, the large-signal tests have been measured and show good behavior over the entire frequency range of interest. If the standard relaxation due to the high voltage is considered the filter meets the standard for both CM and DM noise.

Unfortunately, the baseline filter is pretty large and appropriate techniques need to be applied to decrease its size. However, before optimizing the design, the filter topology and grounding need to be studied in detail.

Chapter 4 Filter Topology and Grounding Consideration

I. Introduction

This chapter describes in detail the different topologies available for a single-stage filter and the best solutions. Moreover, in order to perform the tests shown in this research, much care had to be taken with the grounding scheme. The second part of this chapter will give guidelines and illustrate some consequences if the grounding scheme is not applied properly.

II. Filter Topology Consideration

A baseline filter topology has been chosen by following the approach in [22]; however, so far no real explanation has been shown to justify the topology. It is common to use one- or two-stage low-pass-filter topologies, which leads to many cell possibilities by arranging the capacitors or inductors differently. The next section gives a general approach that could be used to choose the best suitable solution when the impedances are known.

A. Basic Approach to Choose Filter Structure

The fundamental rule to choosing a filter structure is to obtain the maximum impedance mismatch between the motor drive and the input of the filter and between the LISN and the output of the filter. The basic arrangements of the cells' topologies are given in Table 4-1, and differ depending on the source (MD) and load (LISN) impedance of the filter. We know from the baseline calculation that the CM inductance is high while the leakage is small and the DM capacitance is huge whereas the CM capacitance is limited and small. Therefore the 25 Ω equivalent CM impedance of the LISN could be considered low compared to the CM choke and the 100 Ω equivalent DM impedance of the LISN considered high judged against to the leakage inductance. As far as the input impedance of the drive, it hasn't been determined in this research but it is common for the CM to have high input impedance therefore topology "2" is preferred. The DM is

more complex since it has the DC link cap and other impedance that will affect the total impedance. Tests have been made and will be shown later that the “ π ” topology “1” is suitable for this research. Even though the attenuation from C_{X2} is more important, the extra capacitor C_{X1} helps to reduce the DM noise.

Table 4-1: Common cells topologies for EMI filter

Z_{load} Z_{source}	High	Low
High	<p>1</p>	<p>2</p>
Low	<p>3</p>	<p>4</p>

To verify the DM topology, the large-signal measurement of the EMI noise is compared between the “ π ” structure “1” and “LC” structures. Structures “2” and “3” are tested for large signals when only C_{X1} or C_{X2} is used.

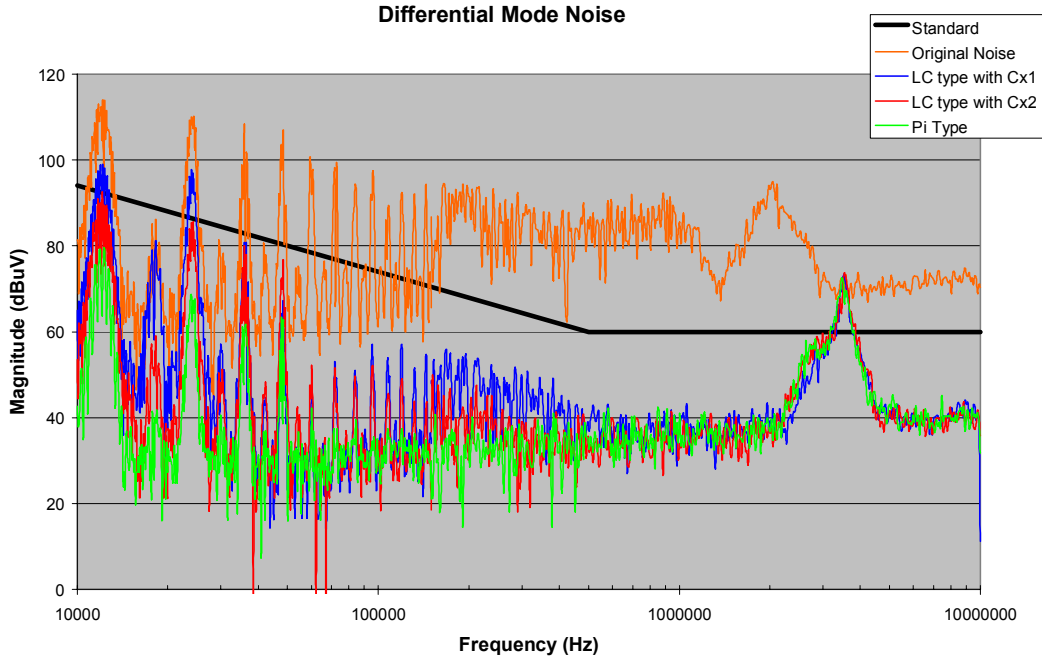


Fig. 4-1: DM topology comparison

It is obvious that the best result is when the “ π ” topology is used due to its better attenuation. Furthermore, we can see that the impact of using only C_{X1} or only C_{X2} is different as described above due to the impedance mismatch for the input or output of the filter. Here the attenuation of C_{X1} is smaller than of C_{X2} since C_{X1} is in parallel with the DC link cap of the MD. The EMI noise that occurs when only C_{X2} is used almost meets the standard at low frequencies; however, the value of the capacitance is at its limit and cannot be decreased while for the “ π ” structure a lot of margin is available. A trade off is therefore noticeable between using one large capacitor or two smaller one. On the other hand, the performances at high frequency for electrolytic capacitor are better for smaller capacitance and also the availability of planar ceramic capacitors for big capacitance is really rare. As a result the “ π ” topology is preferred.

B. Multi-Stage Filter Concerns

The use of a multi-stage filter for low frequencies to further increase the attenuation and reduce the size of the filter could be useful in certain applications; however, when following the MIL461E standard specifications, this is not so for frequencies of 10 kHz and higher, as the benefits of using other stages is very limited in this case and does not lead to a smaller filter size. The same analysis used to calculate the corner frequency

could be performed here by assuming a new attenuation slope depending on the two-stage filter topology. Finally, all of the components' values can be derived and compared to the single-stage filter. It is essential to remember that the constraints on the maximum CM capacitance still apply and the CM capacitance corresponds now to the sum of the stages. Therefore the real CM inductance reduction is small and not significant. To reflect this behavior, an example (cf. Table 4-2) is shown below for the given corner frequencies.

Generally when a two-stage filter is used, the corner frequency of the filter is pushed to higher frequencies due to the higher attenuation. For instance, in this case the corner frequency of the single-stage filter for the CM and DM noise is $f_{CM} = 3780$ Hz and $f_{DM} = 2090$ Hz, respectively, while for the two-stage filter then the corner frequency is $f_{CM} = 7000$ Hz and $f_{DM} = 5860$ Hz. The two stages filter assumes 80dB/dec attenuation for both modes. The theoretical attenuation of the differential mode should be 100dB/dec since an extra capacitor is used for impedance mismatch. However it has been observed that considering this high attenuation may lead to a design that doesn't meet the requirement, it is therefore preferable to keep some margins. The CM corner frequency is doubled while the DM corner frequency is almost tripled. However, to compare the gain, the components values have to be calculated and the maximum CM capacitance is still limited to 100 nF per line, which is 200 nF for the C_{CM} for a single-stage filter and only 50 nF per line or 100 nF for the C_{CM} for a two-stage filter. In this example the leakage is assumed to be 0.5% of the CM choke since it will be with a nano-crystalline core due to the high inductance.

Table 4-2: Components comparison between single and two stages filter

Single-Stage 40 dB/dec assume attenuation		Two-Stages 80 dB/dec assume attenuation	
f_{CM}	3780 Hz	f_{CM}	7000 Hz
f_{DM}	2090 Hz	f_{DM}	5860 Hz
If C_{CM}	200 nF	If C_{CM}	100 nF
L_{CM}	8.9 mH	L_{CM}	5.2 mH
Total Leakage	44.5 μ H	Total Leakage	26 μ H
C_{DM}	130 μ F	C_{DM}	29 μ F

The size reduction of the DM capacitor is tremendous going from 130 μF to 29 μF while the CM choke is reduced from 8.9 mH to 5.2 mH. But when comparing the sizes it is important to remember that two CM chokes and three DM capacitors are used for a two-stage filter (cf. Fig. 4-2), so the final size might not be reduced.

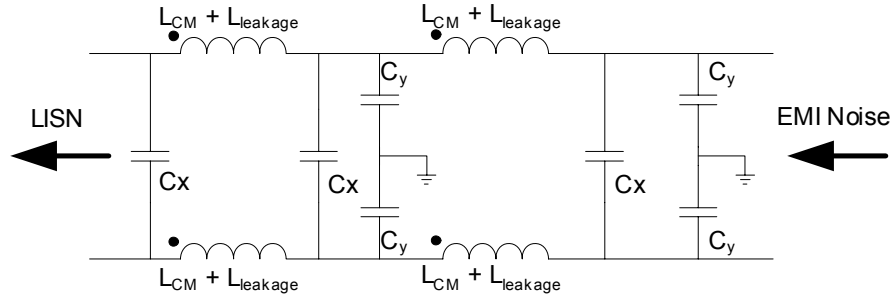


Fig. 4-2: Basic two stages EMI filter for the same frequency range

A multi-stage filter can target the entire frequency range as discussed above, but the stages could also be considered as separate filters, where one filter is used to attenuate the low frequencies while the other filter attenuates the high frequencies. An example of this technique is shown in the next section in which their grounding is studied. The implementation of the multi-stage filter is very delicate and appropriate care need to be applied especially for the grounding scheme. The next section shows that a bad grounding layout for a multi-stage filter could result in a higher final EMI noise.

III. Grounding Effect

Another important aspect of designing the multi-stage filter is the grounding of the filter. It is common knowledge that the CM noise propagates from the power circuit to ground. Changing the type of filter connection to ground, for instance by using wire or copper foil or the length of the actual connection, will alter the filter impedance to ground. The grounding path is studied in the next section for both single-stage and multi-stage filters. Based on analysis and experiments, simple methods are proposed to efficiently ground the EMI filter to maximize its performance [42].

A. Ground Impedance

For the simple “LC” filter shown in Fig. 4-3, the purpose of the C_Y capacitor is to bypass the high-frequency CM noise. However, the high-frequency performance of the

capacitors is a function of the grounding impedance. In real applications, the EMI filter is directly built into the MD so the CM ground inductance is small and doesn't affect the high-frequency behavior too much. On the other hand, if the design of the EMI filters occurs after the completion of the drive, appropriate measures need to be applied during the testing. In this research, studies are performed based on a commercial motor drive, so the EMI filter had to be interconnected between the MD and LISN.

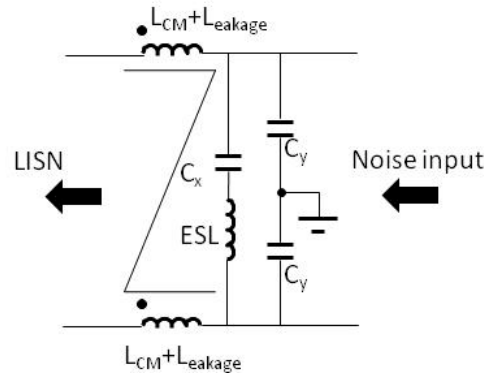


Fig. 4-3: One stage EMI filter “LC” type



Fig. 4-4: Filter interconnection with the drive

For a typical EMI filter PCB layout, the CM capacitors are directly soldered on the copper plane of the filter. The filter ground is then connected to the MD ground as shown in Fig. 4-4. The following experiments show that the length and the type of connection are important. Fig. 4-5 and Fig. 4-6 depict this phenomenon, in which measurements were made with the same filter only changing its type of connection to the ground plane.

Specifically, the yellow trace corresponds to the case where a 50 cm long wire is used to connect to ground, while for the case depicted by the green trace the filter was grounded using a copper foil of 15 cm. Finally, for the last two cases the filter is simultaneously grounded via a wire that is either long (50 cm) or short (15 cm), and is bolted down directly to the motor drive heatsink. For these cases the two connections used provided two parallel paths in which the CM noise could flow, which effectively reduced the equivalent inductance. An equivalent schematic is drawn in Fig. 4-7, while a photograph of the actual setup is shown in Fig. 4-8. However, we can see that the copper foil (one path) measurement is almost the same as the best case when two points are grounded which proves that best solution to ground the system is via copper foil. Even though copper foil alone is the best connection to reduce the CM inductance, the two-ground-point method is employed in this research for simplicity and to keep a systematic measurement. It is important to keep the high-frequency noise as small as possible so we are able to perceive the other parasitic effects.

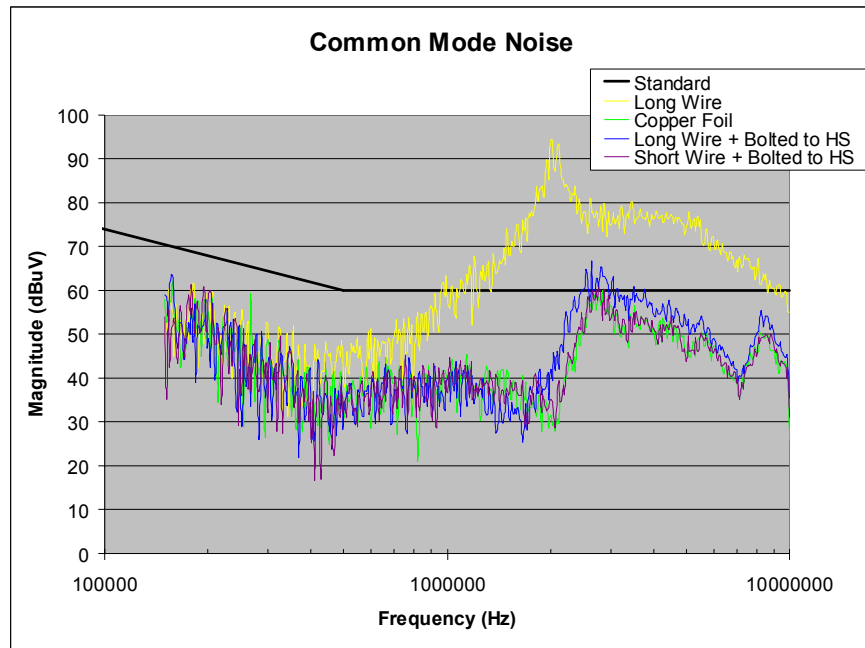


Fig. 4-5: Grounding impedance effect on CM noise

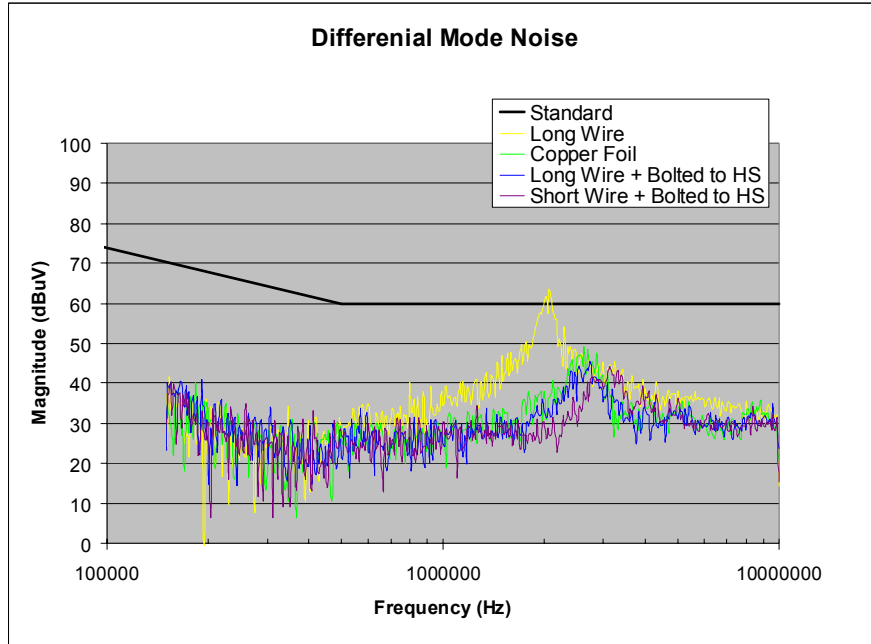


Fig. 4-6: Grounding impedance effect on DM noise

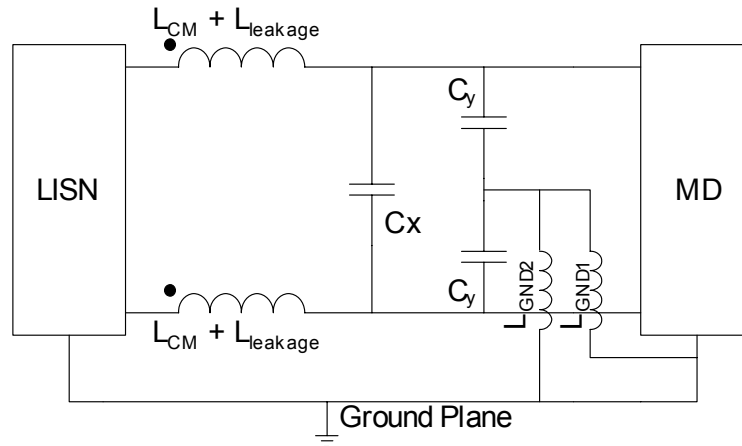


Fig. 4-7: Two points ground equivalent representation

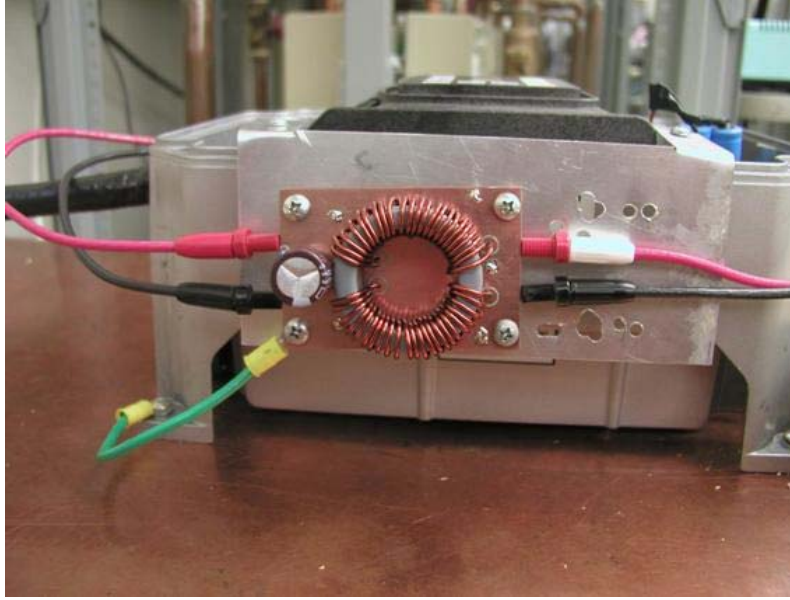


Fig. 4-8: Two points ground setup

Finally, it can be observed in Fig. 4-6 that the type of grounding also affected the DM noise measurements, which could be explained by the structural asymmetry of the filter and the transfer gain from CM to DM. It has been observed that when a “ π ” filter topology is used for the DM noise the asymmetry is reduced greatly and the impact of grounding on DM noise is limited as shown in Fig. 4-9 and Fig. 4-10. The “bad ground” case refers when a long grounding wire is used (50 cm) while the “good ground” case corresponds to the two point ground (bolted and 15 cm wire). The change in topology doesn’t affect the CM noise since the good and bad ground measurements are the same for both cases. However, the maximum amplitude at high frequency for the “LC” structure is either 53 dB μ V or 80 dB μ V depending on the grounding technique, so a 27 dB μ V is noticed between these cases whereas when a “ π ” filter topology is used, the difference is only 6 dB μ V (58 dB μ V compared to 64 dB μ V).

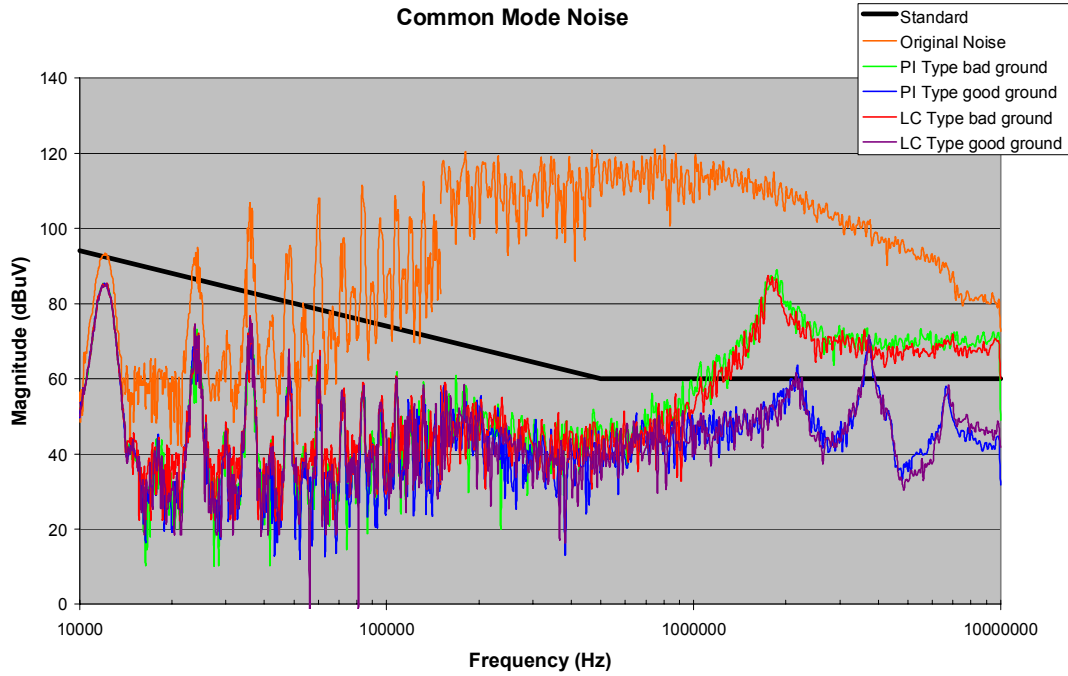


Fig. 4-9: Grounding impact when topology of DM filter is changed on CM noise

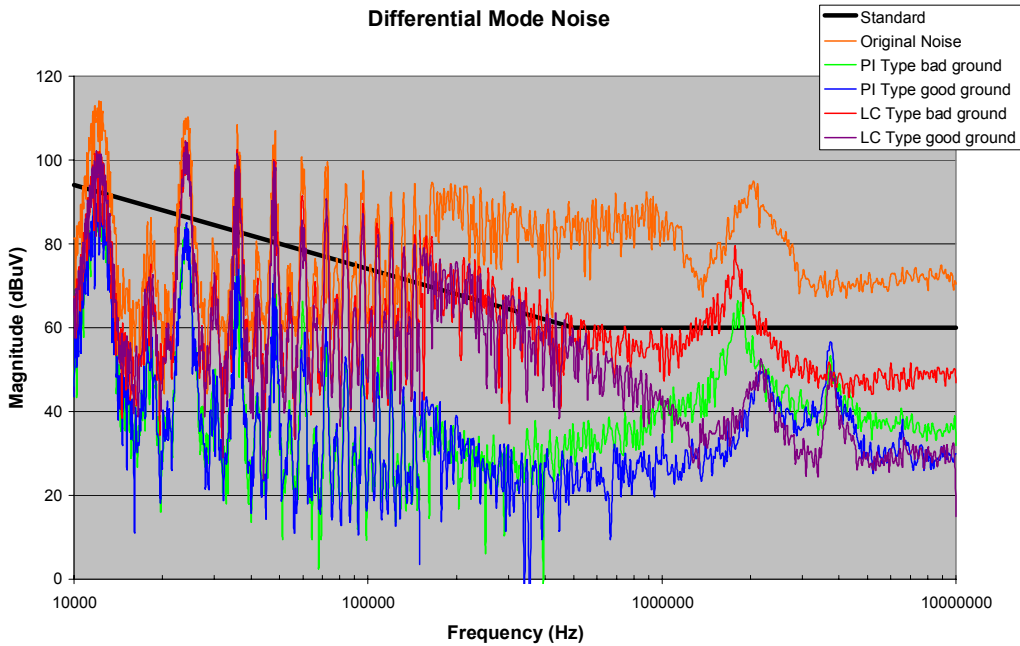


Fig. 4-10: Grounding impact when topology of DM filter is changed on DM noise

B. One Point vs. Multi-Point Ground for Multi-Stage Filter

When multi-stage filters are used, it is important to take into consideration the number of grounding points. In effect, choosing an inadequate grounding method could alter the

filter's performance and easily result in a higher final EMI noise. This is especially the case when a first stage is used to fulfill the low frequency noise requirements while a second stage is used for the high frequency. If the grounding method is not done appropriately, the high-frequency stage could be disturbed from the LF stage due to the high CM current.

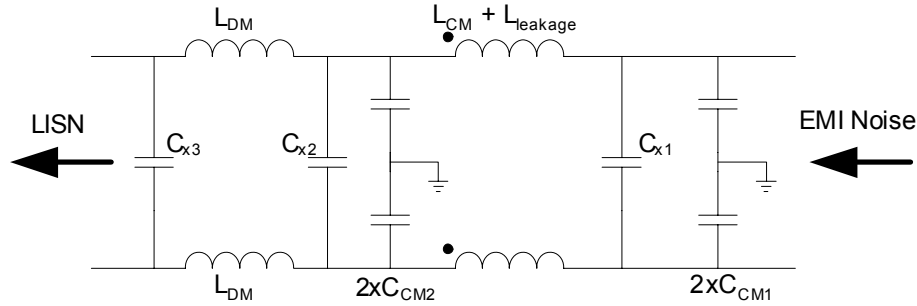


Fig. 4-11: Two stages EMI filter for separate frequency range

To analyze this behavior, the two-stage filter shown in Fig. 4-11 is used. The CM capacitors (C_{CM1} and C_{CM2}) and DM capacitors (C_1 , C_2 and C_3) are in the noise shunt's path and bypass the EMI noise due to their low impedance. Meanwhile the CM inductor (L_{CM1}), its leakage and DM inductors (L_{DM}) block the EMI noise since they are in series and have high impedance. The second CM stage uses the inductance of L_{DM} since the corner frequency of the HF stage is pretty high. The CM equivalent model is shown in Fig. 4-12 and models the CM noise voltage source V_{CM} , which is the sum of the CM parasitic capacitance C_s , while Z_s represents the other effects of parasitics in the CM noise source. Z_2 symbolizes the ground plane impedance between the two grounding point of the filter, while Z_3 is the impedance of the ground plane between the second stage and the LISN. Finally, the equivalent series inductor of the CM capacitors is assumed for further analysis. It should be noted that the current I_{CM3} is much bigger than I_{CM4} due to the first-stage attenuation of 40 dB/dec. If the effects of the grounding parasitics are neglected, and thus the connection is assumed to be ideal the voltage V_{CM2} is given by (4-2). A higher V_{CM2} leads to a higher CM noise measured on the LISN.

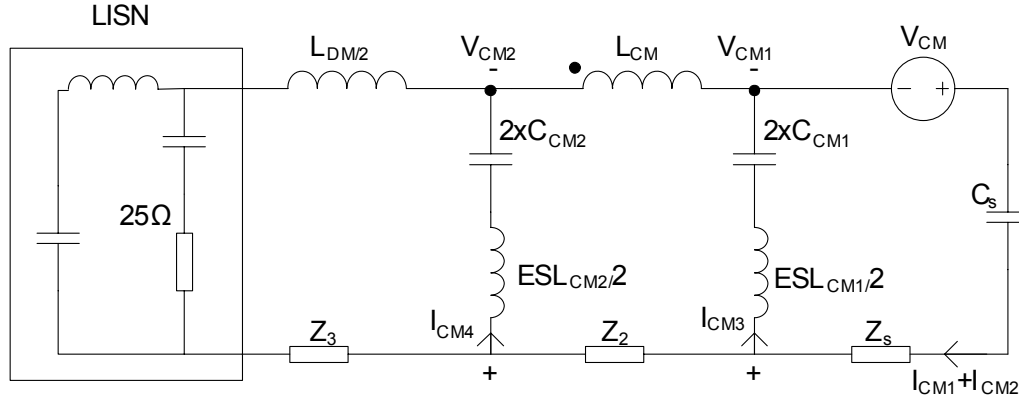


Fig. 4-12: Original CM equivalent model

$$I_{CM_LISN} = (I_{CM1} + I_{CM2}) - (I_{CM3} + I_{CM4}) \quad (4-1)$$

$$V_{CM2} = I_{CM4} \left(j\omega \frac{ESL_{CM2}}{2} + \frac{1}{j\omega 2C_{CM2}} \right) \quad (4-2)$$

1. One-Point Ground

There are two possible ground patterns for the filter in Fig. 4-11. As stated above, in a typical EMI filter PCB layout every CM capacitor is soldered directly to the copper plane of the board, which is then connected to the grounded chassis of the motor drive. This method is a one-point ground system where the two pairs of CM capacitors share the same grounding path shown in Fig. 4-13. In this figure L_{GND} is the inductance of the grounding path between the system ground and the ground plane of the filter's PCB. For this case both CM currents I_{CM3} and I_{CM4} flow through the inductance L_{GND} . The voltage drop across L_{GND} is pretty big due to the large CM current I_{CM3} , and it is given by (4-3). Therefore, the new the CM voltage V_{CM2} given by (4-4) is much larger than (4-2). From this analysis we can conclude that using a one-point ground, or shared grounding path, is not appropriate for a two-stage filter with a low-frequency and high-frequency stage. An appropriate grounding method could be to use a two-point ground, as analyzed on the next section.

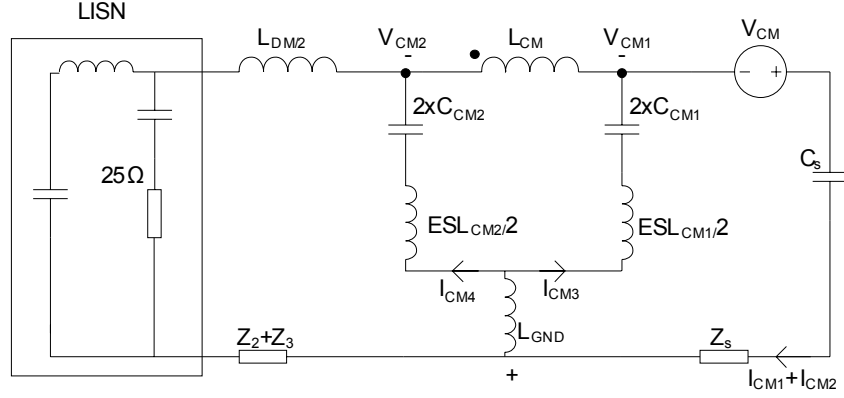


Fig. 4-13: One point ground equivalent CM model

$$V_{L_{GND}} = j\omega L_{GND}(I_{CM3} + I_{CM4}) \quad (4-3)$$

$$V_{CM2} = I_{CM4} \left(j\omega \frac{ESL_{CM2}}{2} + \frac{1}{j\omega 2C_{CM2}} \right) + V_{L_{GND}} \quad (4-4)$$

2. Two-Point Ground

To improve the CM filter's performance, the CM capacitors on each stage need to be grounded separately. The equivalent model shown in Fig. 4-14 takes into account the grounding path inductance L_{GND1} for the first LF filter and L_{GND2} for the second-stage HF filter. It is obvious in this case that the high CM current I_{CM3} no longer affects the second stage, and voltage drop V_{CM2} is given by (4-5). In this analysis the impedance Z_2 is neglected since it is much smaller than the CM inductor's impedance. Thus the CM voltage V_{CM2} is smaller than in (4-4), and the CM attenuation is increased. Other analyses were done in [42] and show that the mutual inductance between the two grounds is very important and should be kept as small as possible otherwise the result for the two-point ground could be very similar to the one-point ground.

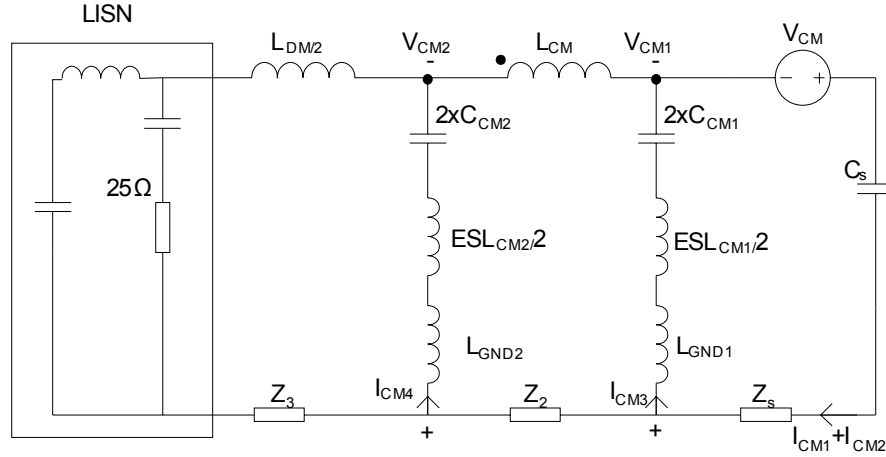


Fig. 4-14: Two point ground equivalent CM model

$$V_{CM2} = I_{CM4} \left(j\omega \left(\frac{ESL_{CM2}}{2} + L_{GND2} \right) + \frac{1}{j\omega 2C_{CM2}} \right) \quad (4-5)$$

3. Simulated and Experimental Results

To verify these conclusions, this section describes simulations and experimental measurements. The CM filters with one- and two-point grounds (Fig. 4-15) were simulated using Saber simulation software, and the insertion gain for different cases is recorded in Fig. 4-16. The blue curve represents the simulation for the one-point ground circuit when the ground impedance L_{GND} is changed from 0 to 500 nH in six steps. It is obvious that when the impedance is considered ideal (0 nH) the insertion gain is optimal; however, as soon as some small ground inductance is considered, a big jump is noticeable. The two-point ground result is shown as the pink curve when the ground inductance of the first stage is kept constant (100 nH) and the ground inductance of the second stage changed from 0 to 500 nH. Obviously, the pink curve cannot beat the one-point ground when ideal ground is used; however, for any other case it is much better. The simulation result supports the theoretical analysis.

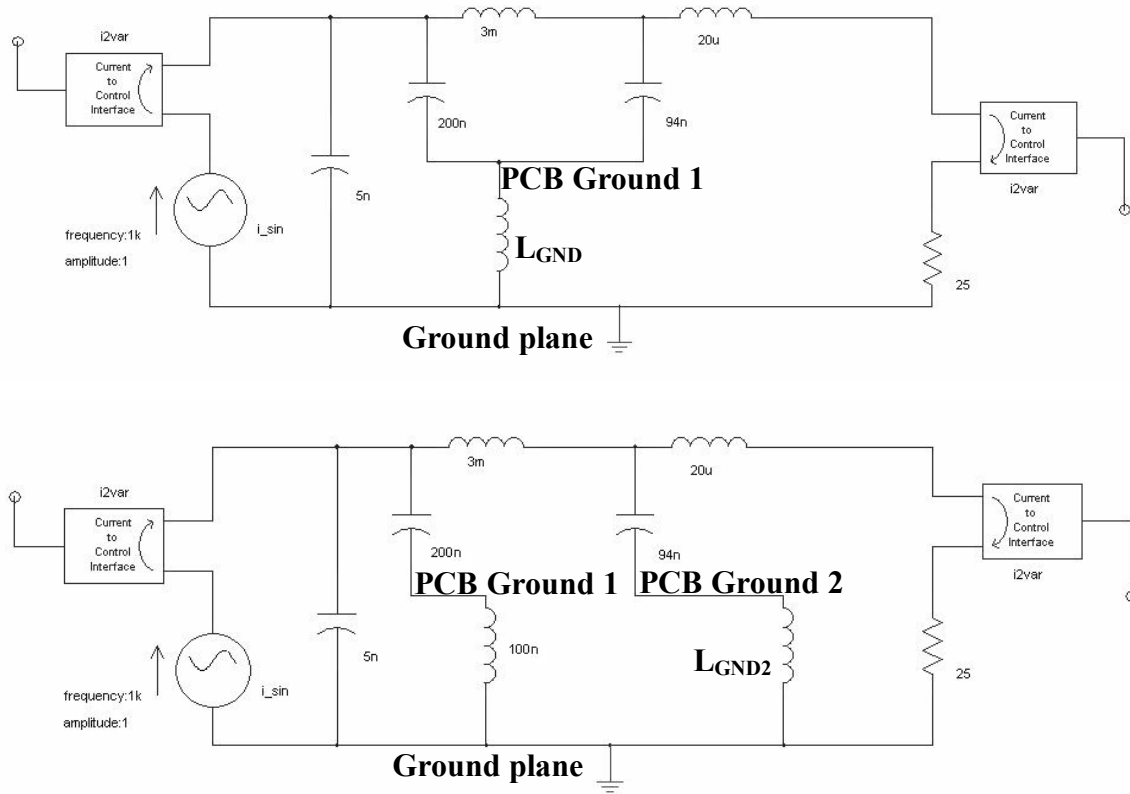


Fig. 4-15: One (top) and two (bottom) point ground CM filter used in simulation software (Saber)

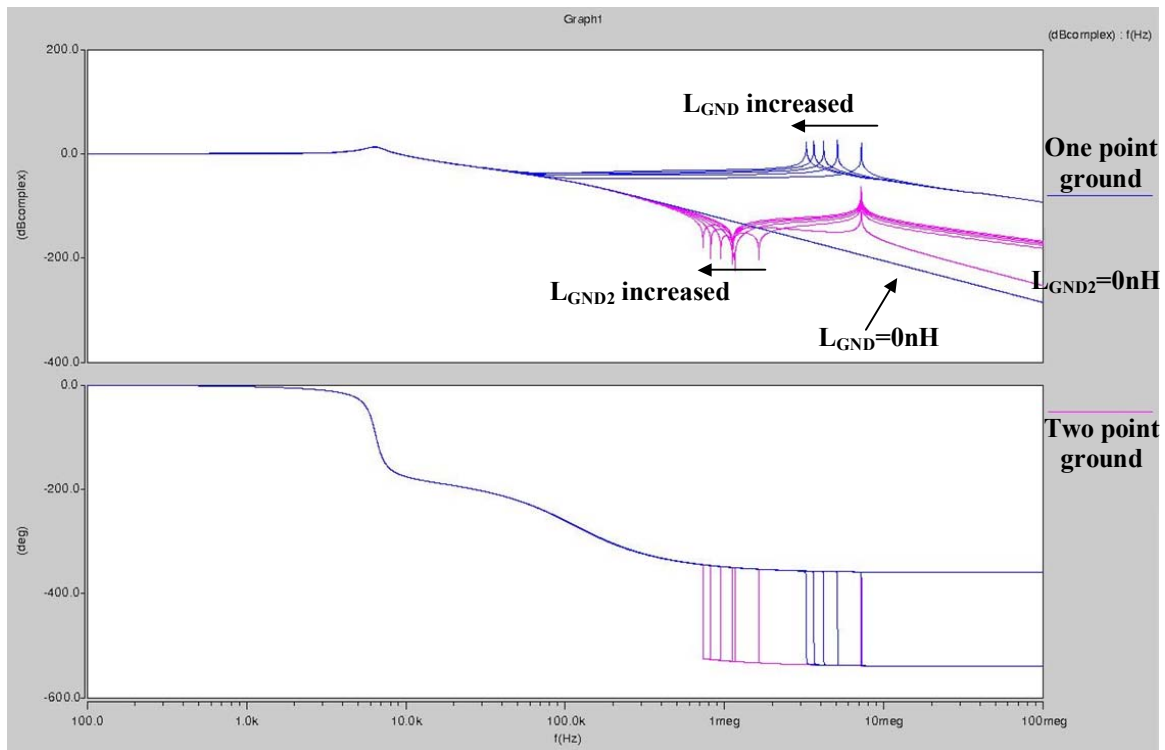


Fig. 4-16: One and two point ground simulation results

Finally, an experiment is carried out with large signals to conclude the analysis. The PCB layout and picture of the multi-stage filter with one-point ground is shown in Fig. 4-17 and **Error! Reference source not found.**, respectively, while the two-point ground layouts are illustrated in Fig. 4-19 and **Error! Reference source not found.**. The experiment setup could be materialized as shown in Fig. 4-21 and Fig. 4-22 for both one-point and two-point ground, while the actual setup is pictured in Fig. 4-23.

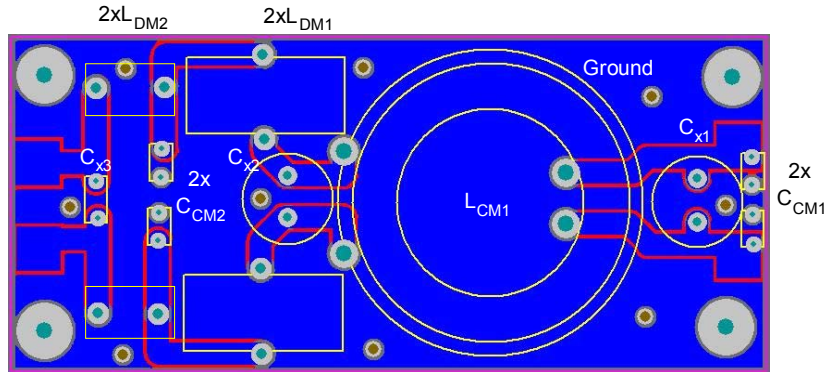


Fig. 4-17: EMI filter PCP layout with one point ground



Fig. 4-18: EMI filter layout with one point ground

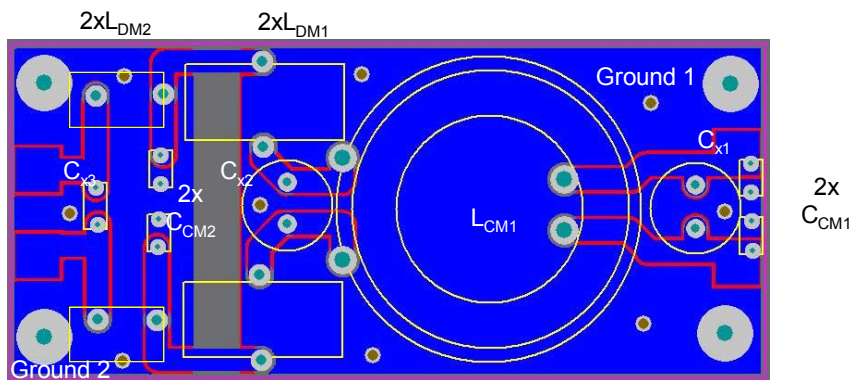


Fig. 4-19: EMI filter PCP layout with two points ground

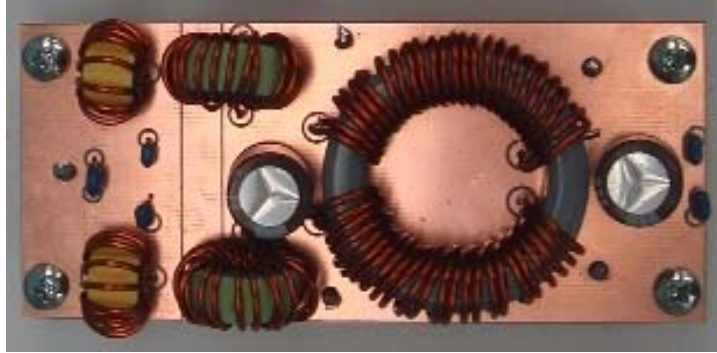


Fig. 4-20: EMI filter layout with two point ground

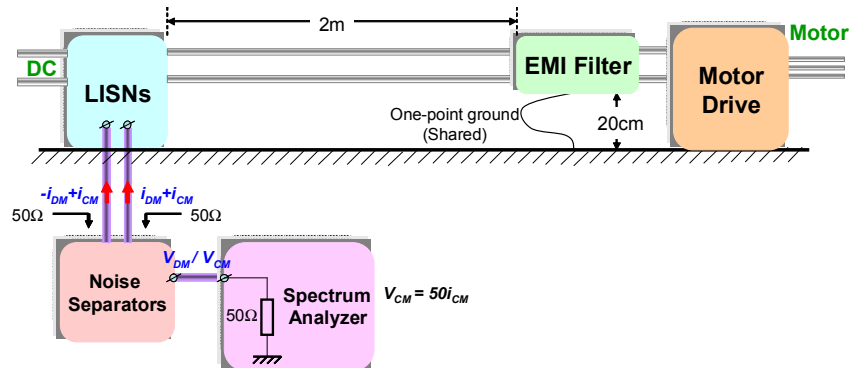


Fig. 4-21: EMI measurement setup representation: one point ground

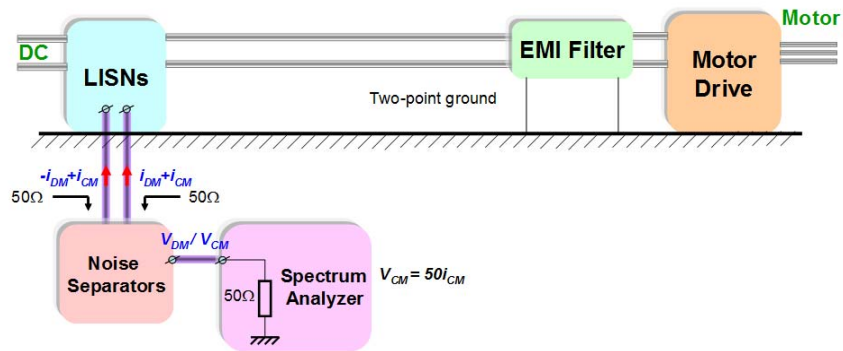


Fig. 4-22: EMI measurement setup representation: two point ground

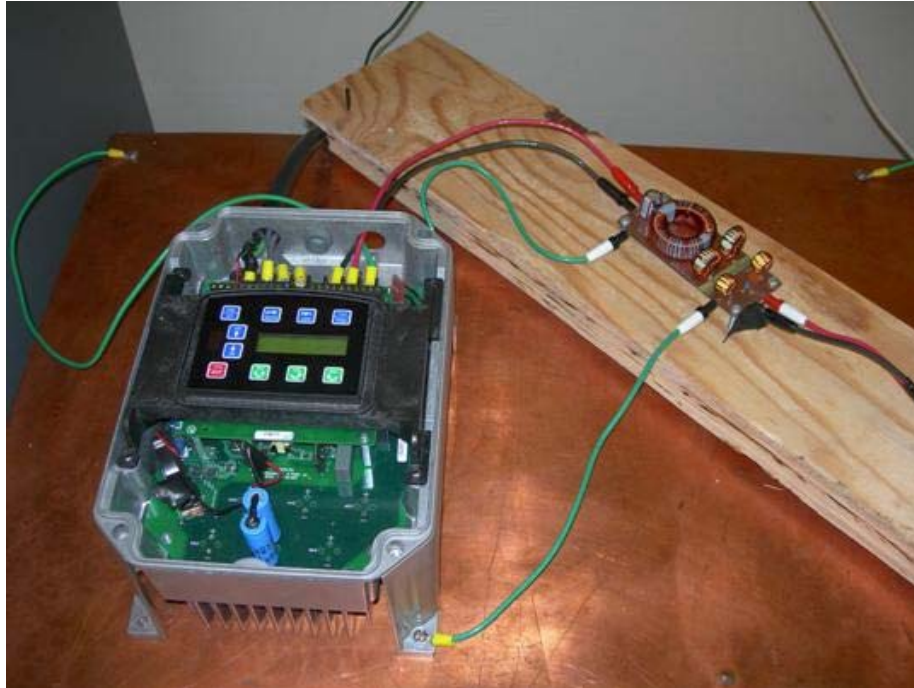


Fig. 4-23: Picture of EMI measurement setup: two point ground

The EMI noise measurements are shown in Fig. 4-24 and Fig. 4-25, and clearly prove that when the one-point ground method is used, the high-frequency CM noise is much higher than when the two-point ground is used. In the one-point ground setup, the high-frequency spike is almost 38 dB μ V higher. This concludes the analysis on the grounding connection. Thanks to these guidelines, proper measurement could be done in the next section to show the behavior of parasitic at high frequency.

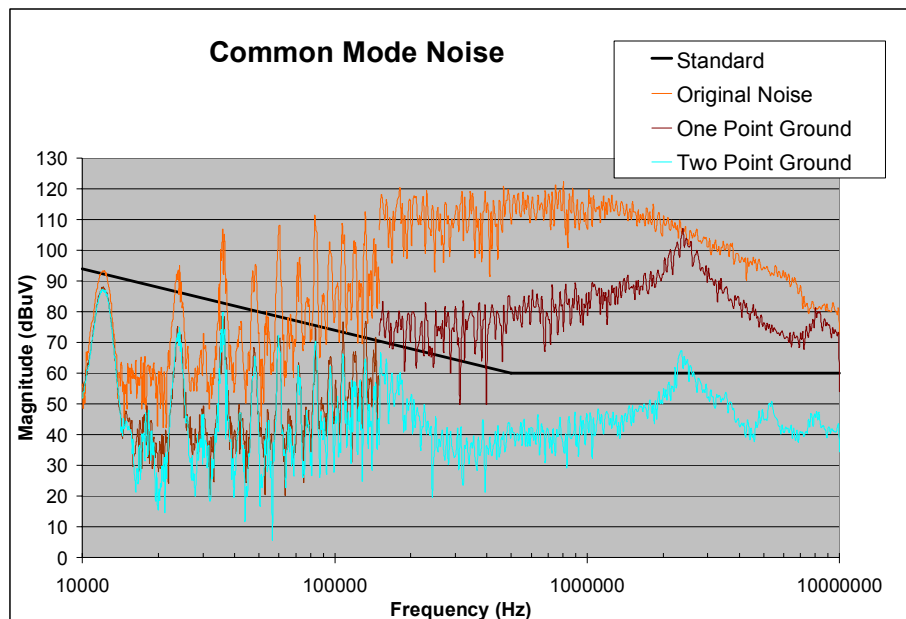


Fig. 4-24: Comparing effects of grounding methods on CM noise for a multi-stage filter

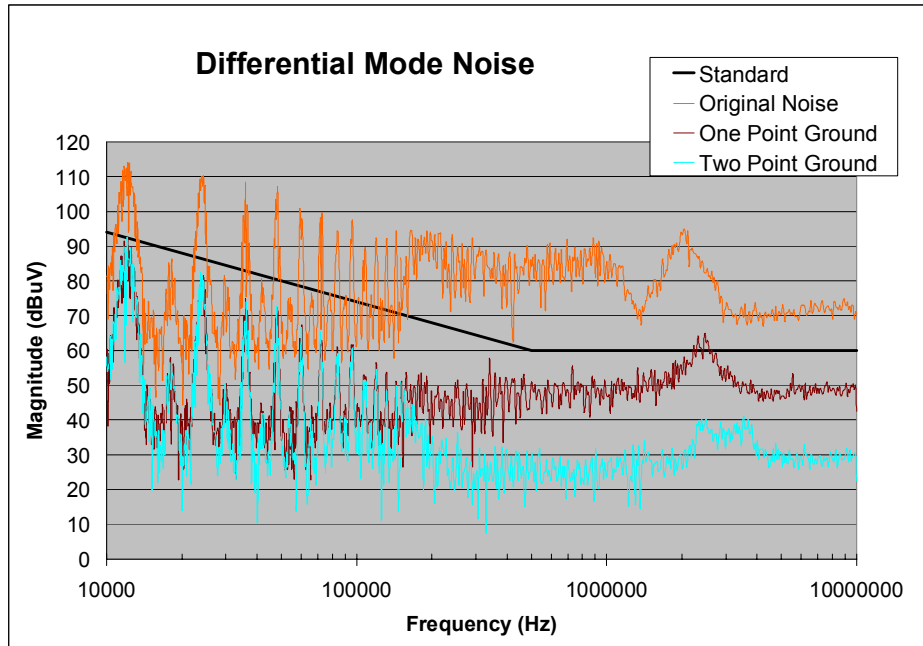


Fig. 4-25: Comparing effects of grounding methods on DM noise for a multi-stage filter

IV. Summary

Many important guidelines have been articulated in this section. As stated above, when choosing the filter topology it is vital to consider the impedance connected at the input and output side of the filter to create the maximum impedance mismatch to emphasize the filter's performance. Even though this research didn't result in a good model for the converter input impedance, the best filter structure was easily picked after some trial and error. However, it could be useful to develop a real model to show the impedance of the motor drive. This idea is mentioned in the future work at the end of this paper. Finally, the importance of the grounding scheme has been verified by experiments and proves that the grounding inductance and the grounding patterns of CM capacitors are very important to improving the CM filter's performance. A bad grounding method leads to a higher noise and the inability to understand the other parameters' effects on the filter.

Chapter 5 Approaches to Minimizing Size and Improving Performance of EMI Filter

I. Introduction

Now that the baseline design, topology and guidelines for grounding the system have been revised, it is essential to look at the optimization of the EMI filter and especially at the size reduction of the CM choke to achieve a high-density EMI filter. The first part of this section deals with the material technology available that could help to reduce the volume of the filter, such as the nanocrystalline core. Later on, the key parameters of the CM choke, such as the leakage, the EPC and the saturation, are calculated, analyzed and pushed to their limits. The multi-layer winding technique is then analyzed and tested with a large signal to prove its integrity and benefit. Moreover, a new structure is proposed to integrate a CM and DM inductor in the same core to increase the total DM inductance and reduce the total volume. Lastly, a small study on capacitors is performed to determine the effect of voltage rating and the benefit of a ceramic capacitor for DM mode for use with large signals.

II. CM Choke Core Material

The type of material used for the CM choke is very important. It will set the maximum saturation flux density, the number of turns needed to achieve the given CM inductance, and its behavior depending on the temperature.

It is usual to use a toroidal ferrite-type material, which is cheap and performs well from low to high frequencies. On the other hand, ferrite material has a small saturation flux density (≈ 0.4 T) which is dependant on the temperature, as shown in Fig. 5-1. When the core reaches a temperature of 100 °C the saturation is almost halved, and achieves 0.24 T instead of the 0.42 T seen at 20 °C. The change in saturation flux density could lead to the saturation of the core when the temperature increases. This is an important constraint, since the design will have to be made with the minimum saturation and keep

some margin therefore the size of the choke won't be optimized. A fan could be added in the design but would increase the total volume.

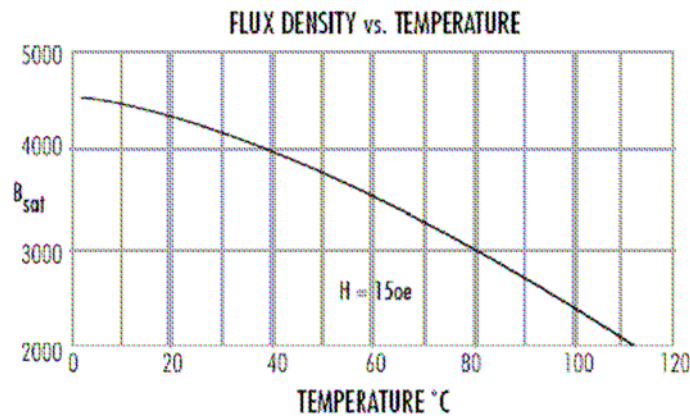


Fig. 5-1: Flux density in function of temperature for ferrite core

The ferrite “J” type material is often used and has a permeability of 5000. Nevertheless, when a really high CM inductance and small size is needed, the ferrite technology is lacking. A better material choice will be the nanocrystalline core, which has a initial permeability of >70,000 with a saturation flux density three times higher than ferrite (1.3T) that is almost independent of the temperature. Furthermore, its curie temperature is much higher than ferrite (570°C compared to 150°C for ferrite). A thorough comparison of the ferrite and nanocrystalline core appears in Fig. 5-2 [43] [44]. In this research the FINEMET FT-3KM cores from Metglas are used.

		FT-1KM	FT-3KM	Mn-Zn ferrite
Initial permeability at 100 kHz μ_r	20° C	16,000	17,000	5,300
	100° C	16,300	18,000	7,000
Impeadance permeability at 100 kHz μ_{rz}	20° C	25,700	26,900	5,300
	100° C	26,300	27,100	7,000
Saturation magnetic flux density B_s^* (T)	20° C	1.35	1.23	0.44
	100° C	1.30	1.20	0.27
Residual magnetic flux density B_r^* (T)	20° C	0.81	0.62	0.10
	100° C	0.73	0.59	0.06
Corecive Force H_c^* (A/m)	20° C	1.3	2.5	8.0
	100° C	1.4	2.7	4.9
Curie temperature T_c (°C)		570	570	150
Saturation magnetostriction λ_s (x10 ⁻⁶)		+2.3	-0.0	-1.1
Electrical resistivity ρ ($\mu\Omega \cdot m$)		1.1	1.2	1.0X10 ⁵
Density d (kg/m ³)		7.4X10 ³	7.3X10 ³	4.85X10 ³

Fig. 5-2: Comparison between nano-crystalline and ferrite core

The nano-crystalline core therefore seems to be the best suitable technology; however, some precautions need to be taken when designing the other parameters of the filter. First, since the permeability of the nano-crystalline material is much higher, the number of turns required to obtain the same CM inductance is lower than for ferrite. The size of

the CM filter is consequently decreased greatly. On the other hand, the leakage inductance provided by the CM choke is reduced. As estimated in [45], the leakage is proportional to the number of turns, and is almost independent of core permeability for relative permeabilities (μ_r) higher than 5000. To compensate for this lack, it is preferable to add a small DM inductor. The size of the filter may not increase, since a higher total DM inductance will decrease the required DM capacitance. A tradeoff occurs between the reduction of the DM capacitor and the addition of an extra inductor.



Fig. 5-3: CM choke representation using ferrite and nano-crystalline core

Table 5-1: CM choke's design parameters

Parameters	Ferrite 3	Nano 1	Nano 2	Nano 3
Current Density (A/cm^2)	800	800	800	800
Wire Gauge #	18	18	18	18
# of Turns per side	36	11	14	24
L_{CM} (mH) @5kHz	4.6	3.8	3.7	19.3
Leakage (μH) @5kHz	53.7	4.1	5.0	18.3

Table 5-1 show the design parameters of 4 CM chokes; one composed of a ferrite core and three composed of nano-crystalline cores. The leakage provided for the 36-turn ferrite core (4.6 mH inductance) is ten times larger than the first two nano-crystalline cores for almost the same inductance. As for the size, as shown in Fig. 5-3, the size of Nano 2 is reduced significantly. The Nano 3 core will be discussed in the next section.

The second important point to notice is the behavior of the nano-crystalline core at mid-range frequencies (between 10 kHz and 250 kHz), where, as shown in Fig. 5-4, its permeability drops very quickly compared to the “J” type ferrite, charted in Fig. 5-5. Another difference is that the permeability of the nano-crystalline material is independent of temperature, as shown in Fig. 5-4, while the permeability of ferrite cores is very

dependent on temperature [38]. Fortunately, more tests have confirmed that increasing the number of turns slightly will compensate for its drop in permeability and will make the nano-crystalline core behave perfectly over the entire frequency range, like the “Nano 3” choke previously discussed.

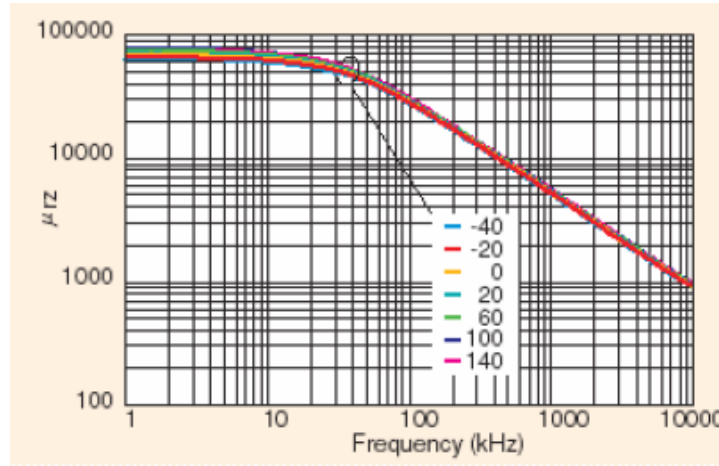


Fig. 5-4: Temperature (degree) dependence on permeability for nano-crystalline core

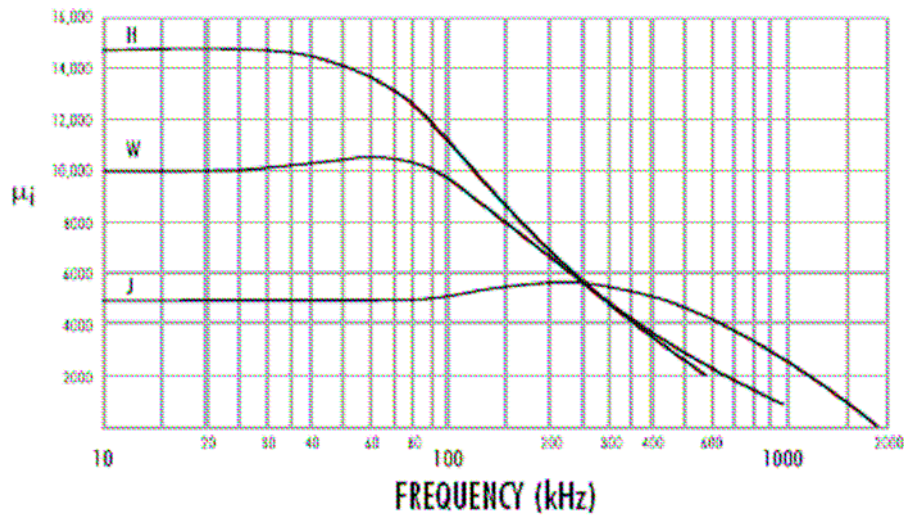


Fig. 5-5: Permeability behavior for ferrite core

Fig. 5-6 shows the small-signal measurement of the CM inductance of these four cores. The drop in permeability for medium-range frequencies is obvious for nano-crystalline cores, while the disparity in leakage is shown in Fig. 5-7

Inductance CM Choke

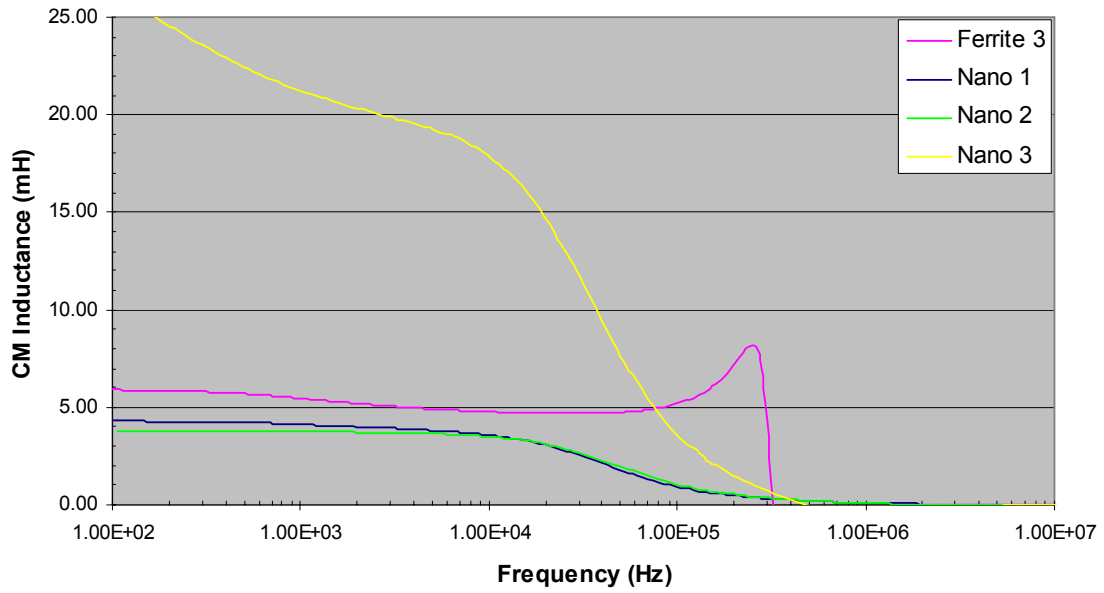


Fig. 5-6: CM Choke inductance

Leakage CM Choke

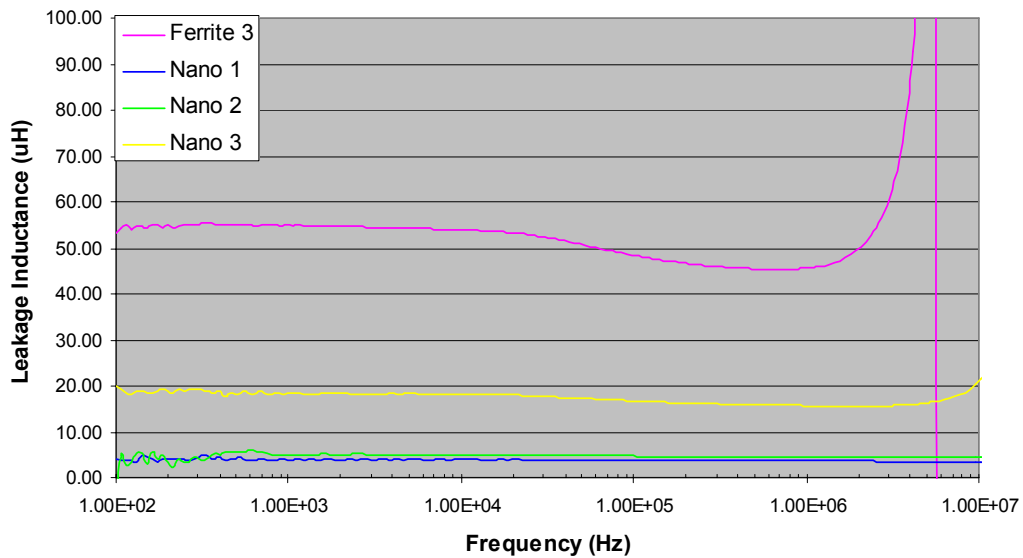


Fig. 5-7: Leakage inductance of CM Choke

Finally, the large-signal tests are carried out to check the integrity of the small-signal measurements. Fig. 5-8 illustrates the drop in permeability for the nano-crystalline core in

blue “Nano 1” and the same core with more turns, which is in yellow to counteract the bad performance “Nano 3”. Fig. 5-9 on the other hand, proves that the DM noise is greatly affected by the lack of leakage and the incapacity to meet the standard at low frequencies.

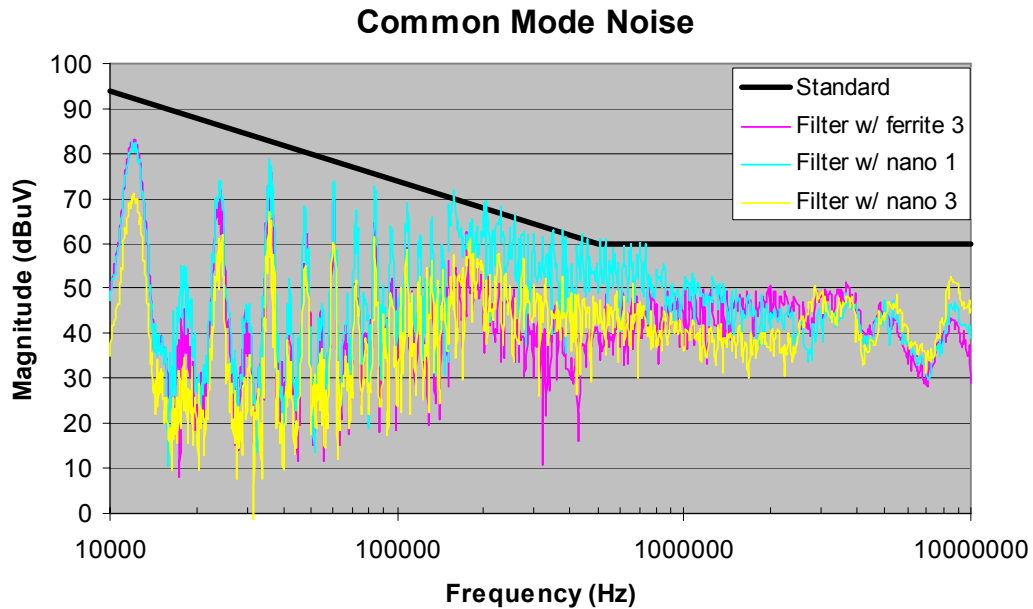


Fig. 5-8: CM comparison for 3 cores

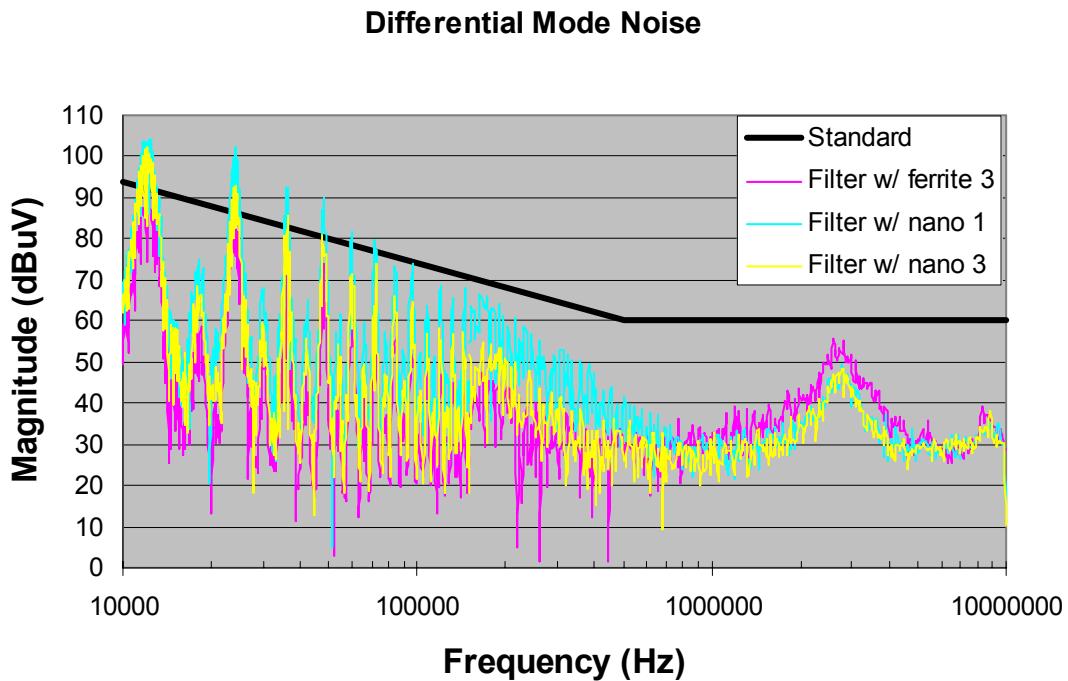


Fig. 5-9: DM comparison for 3 cores

Even though some drawbacks have been found for the nano-crystalline technology, it is considered to be the best solution in this research due to its high number of benefits in decreasing the size of the filter. Furthermore, an integrated structure that incorporates both CM and DM inductance is presented in the next section and provide a really good solution to increase the DM inductance.

III. CM Choke Parameters

A. Key Relations between CM Choke Parameters' Designs

Now that the structure of the CM choke has been defined, its design parameters need to be studied. This section will try to show the impact that each of them have on each other and the consequences for size and performance.

We can first classify the input parameters of the core material, current density and winding structure that the user will choose depending on the purpose and goal of the filter. These input parameters will affect either the output parameters, such as the CM choke size or performance, or will affect the internal parameters like the number of turns, saturation, thermal, EPC and leakage. The entire representation of the correlations between parameters is shown in Fig. 5-10.

The core material is obviously the main element of the CM choke. It will directly affect some important parameters, such as the effective permeability and saturation flux density. The core material chosen will then influence the final performance, size and internal parameters like saturation and leakage.

The current density is used to define the wire gauge of the winding depending on the input current. Increasing its value will evidently reduce the size of the wire and the total size of the choke, but will also make the core hotter and change the performance. Some tradeoffs need to be considered during the design process, which will depend on the desired running temperature, cooling method and size.

Changing the winding structure, as well as the current density, is a good way to decrease the size of the CM choke by, for example, using a multi-layer winding. However, using this kind of technique will have many impacts on the performance. For instance, the total leakage, due to its dependency on the winding angle, will be bigger and

the EPC will increase considerably. Finally, since the wires are stacked on each other, the thermal dissipation will be worse and the temperature will increase.

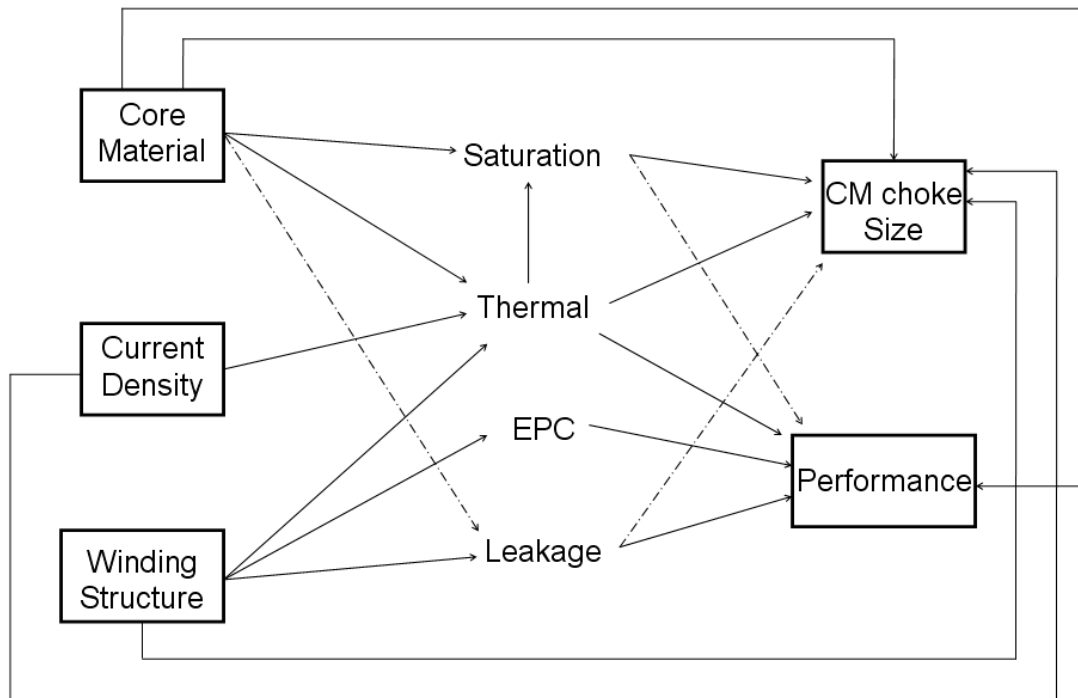


Fig. 5-10: Correlation between CM choke parameters

Now that the relations between the core parameters have been briefly explained, the calculations and effects of internal parameters can be discussed.

B. Parameters Calculation and Concerns

i) Leakage

The DM inductance is commonly achieved by using the leakage inductance from the CM choke. However, in some cases, it could be preferable to include an extra DM inductance to reduce the DM capacitor and consequently the total size of the filter.

Reference [45] shows that the leakage can be calculated, and derives formula in (5-1).

$$L_{DM} = \mu_{DM_effective} \frac{0.4\pi N^2 A_e}{l_e \sqrt{\left[\frac{\theta}{360} + \frac{\sin(\theta/2)}{\pi} \right]}} 10^{-8} \text{ in Henry} \quad (5-1)$$

It is important to mention that the leakage is directly proportional to the number of turns and inversely proportional to the winding angle. Furthermore, it is vital to note that the leakage is independent of the permeability of the material if the effective permeability is above 5000μ , which is the case for the ferrite and nano-crystalline core studied.

ii) EPC

As we know, the impedance of an inductor varies along with the frequency and becomes capacitive at high frequencies due to the parasitics' capacitance. Unfortunately, the CM attenuation of the EMI filter will be altered by the total EPC and won't work as expected at high frequencies. Thus it is important to minimize these parasitics' capacitances, which correspond to the turn-to-core and turn-to-turn capacitances. The following formulas are detailed in [46] which approximate these equivalent capacitances.

$$C_{turn-turn} = \epsilon_0 l_t \left[\frac{\epsilon_r \theta^*}{\ln \frac{D_o}{D_c}} + \cot(\theta^*/2) - \cot(\pi/12) \right]$$

Where (5-2)

$$\theta^* = \cos^{-1} \left(1 - \frac{\ln \frac{D_o}{D_c}}{\epsilon_r} \right)$$

Finally, after simplification and assuming (5-2), the total equivalent capacitor could be calculated with (5-3) for a single-layer core when $n > 9$. The paper also presents different formulas when dealing with multi-layer windings.

$$C_{turn-core} = 2 \times C_{turn-turn} \quad (5-3)$$

$$EPC = C1 \cong 1.366 \times C_{turn-turn}$$

From these equations we see that the EPC is independent of the number of turns as long as the number of turns is higher than 10. We have discussed that using multiple layers

will increase the stray capacitances, and thus deteriorate the high-frequency behavior. Future experiments will show that the EMI noise is slightly worse for multi-layer windings, but the size gain is so important that it will be preferred.

Many papers [47]-[48] introduce techniques to cancel or reduce the effect of the parasitics' capacitance. The technique used in [47] will be briefly discussed and tested for small and large signals.

This technique involves adding other capacitors to the middle point of each winding, which cancels the parasitic effect. To achieve this, the bifilar winding method is proposed in [47] to keep the coupling coefficient of two half-windings high enough. The equivalent drawing of the bifilar winding is shown in Fig. 5-11, while a real representation is observed in Fig. 5-12. The EPC cancellation capacitor that needs to be added is approximately four times the EPC but need to be adjusted.

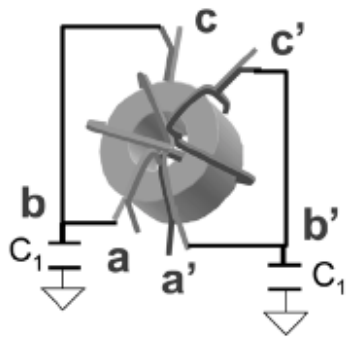


Fig. 5-11: Bifilar winding drawing

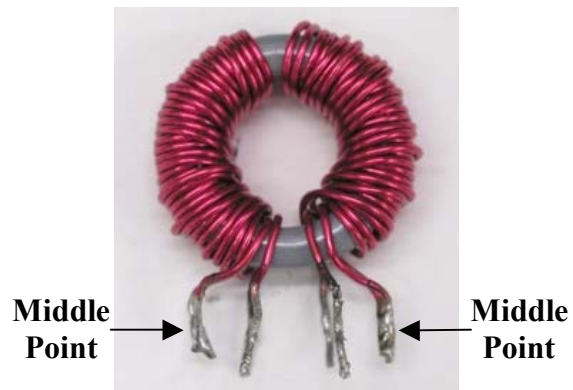


Fig. 5-12: CM choke using bifilar winding

iii) Winding Structure

Another improvement that can be pursued for these CM chokes is the winding method. As seen in Fig. 5-13, the window area of the baseline CM choke “Ferrite 1” is quite empty and hence more turns could be applied. As known, when designing the same inductance the use of multi-layer windings permits the use of much smaller cores, and especially so when thinner wire is used. The wire diameter is generally assumed with the current density during the design process. It will impact the steady state temperature and therefore the required core technology. As an example Fig. 5-13 shows the CM size improvement when the current density is double and the multi-layers technique is used while Fig. 5-14 show the reduction when applied in filters. The total footprint is almost

reduced by three times while the performance is good enough to meet the EMI standard. Unfortunately, the reduction is quickly stopped by thermal and saturation constraints as shown in the next sub-section. Moreover, the use of multi-layer windings changes the parasitics of the inductors and hence their behavior at high frequency. Specifically, the effective parallel capacitance (EPC) increases significantly in this case, since the distance between each winding is smaller, making the EPC bigger. Nevertheless, as seen on the next section the EPC has been confirmed to affect the small signal measurement while the large signal may behave differently.



Fig. 5-13: CM chokes comparison after multi-layers winding and higher current density

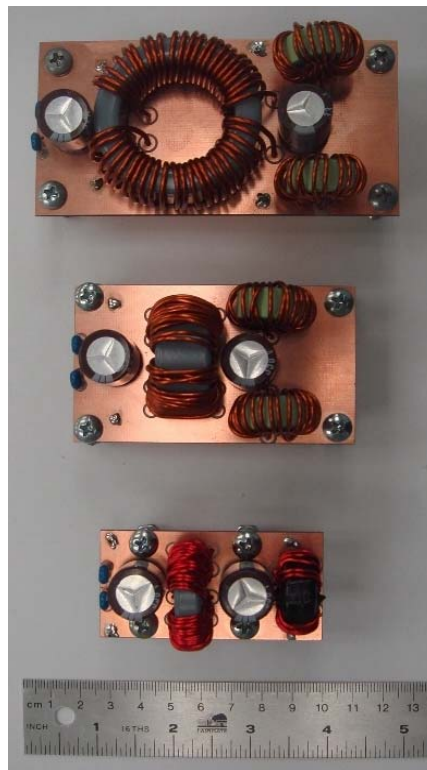


Fig. 5-14: Filter reduction when CM choke is improved

Table 5-2: CM choke's parameters

Parameters	Ferrite 1	Ferrite 2	Ferrite 3
Current Density (A/cm ²)	400	500	800
Wire Gauge #	14	16	18
# of Turns per side	23	24	36
L _{CM} (mH) @5kHz	3.1	3.7	4.6
Leakage (μH) @5kHz	36.1	30.3	53.7
EPC (pF)	11.8	30.7	51.6

Table 5-2 summarizes the parameters of these three inductors; however it should be noticed that the cores, number of turns and wire gauge are all different. All parameters have been extracted with the impedance analyzer Agilent 4294A.

iv) Temperature and Saturation

It is common to not take into account the saturation when designing the CM choke. This statement is normally true for most cases when margin are applied in the design like for the baseline filter. However, when optimization is the goal, the saturation problem becomes quickly an issue and generally turns out to be the limit of the design. The saturation of the choke may happen from both, the saturation due to the CM noise current or the saturation caused by the DM current and the leakage of the core [49].

Both equations (5-4) and (5-5) need to be calculated and compared to the saturation flux density given by the material at the running temperature. It is therefore important, to calculate the temperature rise of the CM choke for the current condition.

$$B_{CM} = \frac{L_{CM} \times I_{CM}}{N_{/side} \times A_c} \text{ in } T \quad (5-4)$$

$$B_{DM} = \frac{L_{leakage} \times I_{DM}}{N_{/side} \times A_c} \text{ in } T \quad (5-5)$$

The temperature rise of the CM choke is caused by two factors: the core and the winding loss.

The core loss is generally derived from the Steinmetz empirical equation and it is usually given by the core manufacturer. From [38], the core loss is given by (5-6) while the coefficient will depend on the material type and frequency of operation.

$$P_{core} = a \times f^c \times B^d \times V_{core} \text{ in } mW \quad (5-6)$$

The winding loss is mostly due to the line current and the copper winding resistance (5-7).

$$P_{winding} = \frac{\rho \times N \times Mlt}{A_w} I_{rms}^2 \text{ in } W \quad (5-7)$$

When the lost are known, the rising temperature will be calculated using the sum of the two and (5-8).

$$T_{rise} = \varepsilon \times \left(\frac{P_{core} + P_{winding}}{A_{core\ surface}} \right)^{0.833} \text{ in } ^\circ C \quad (5-8)$$

Where ε is the correction coefficient that will need to be estimated with experiment.

The previous formulas have been used to evaluate the predicted temperature rise and the measured value after reaching steady temperature. An error of 10% was noticed which could have been reduced by increasing the number of measurements to get a better correction coefficient for this case. All tests are shown in the next section.

C. Parameters Effect on Small and Large Signals Measurements

i) Leakage, EPC, Winding Structure effects

In order to look at the impact of parameters four CM chokes have been made with the same core reference and keeping the same number of turns. The winding structure is then changed which will impact the leakage and EPC. The ferrite core use for this experiment is the ZJ42908TC which has a permeability of $5000\mu \pm 20\%$. It is important to emphasize the big tolerance which would impact the CM inductance in the later cases. For all cases the number of turns is kept constant (30 Turns) and the gauge wire is AWG #20.

The four cases are described as follow:

- Case 1: Single layer, 30 turns
- Case 2: Double layers, 15 turns per layer
- Case 3: Single layer, bifilar method 30 turns total
- Case 4: Double layers, bifilar method 14 turns for the first layer and 16 turns for the second layer

It is obvious that the winding angle is therefore much smaller when double layers are used (case 2 & 4), as shown in Fig. 5-15. After measuring each parameters with the impedance analyzer they could be summarize in Table 5-3. The CM inductance should be the same for each case since the number of turns is keep the same, however due to the permeability tolerance the value is a bit off for some cases. The EPC behavior follows the equations previously given since the double layer method lead to an EPC three times higher than single layer. The bifilar cases are not taking into account here since other phenomenon could appear and would have to be calculated. The leakage follows also the theoretical calculation since the cores with the smallest winding angle (2 & 4) have the highest leakage. In order to check the impact on large signals case 1 and 4 are selected since they have the largest difference in EPC and leakage. Moreover case 4 will be used to test the EPC cancellation technique.

Table 5-3: Choke parameters for 4 Cases

Cases	Resonance (MHz)	Inductance (mH)	EPC (pF)	Total Leakage (μH)
1	1240	3.2	5.1	32
2	670	3.6	15.7	46
3	814	2.8	13.6	34
4	718	3.0	16.4	54

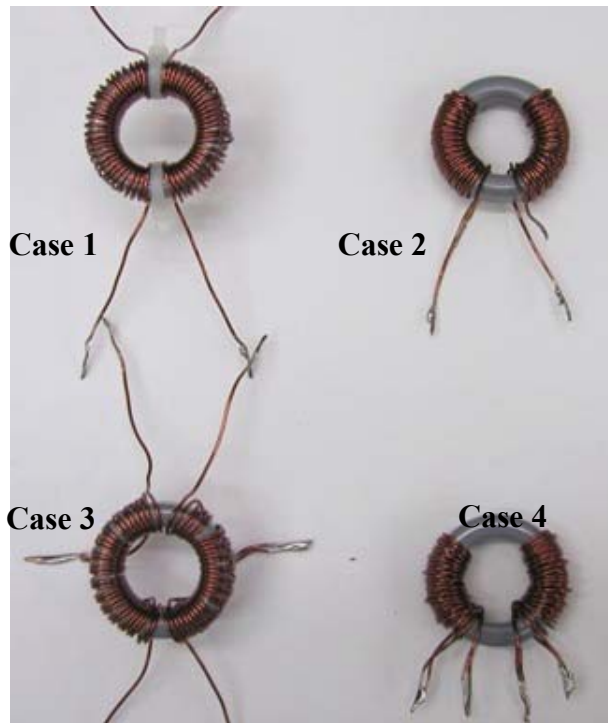


Fig. 5-15: 4 CM chokes used for experiment

First of all the CM insertion gain is measured for cases 1 and 4 where each choke have been placed in the same EMI filter. It could be notice that the insertion gain is almost 10 dB lower between 1 MHz to 100 MHz for case 1 which can be explained by the EPC effect since case 1 has the smallest EPC. The next step is therefore to check the large signal measurement.

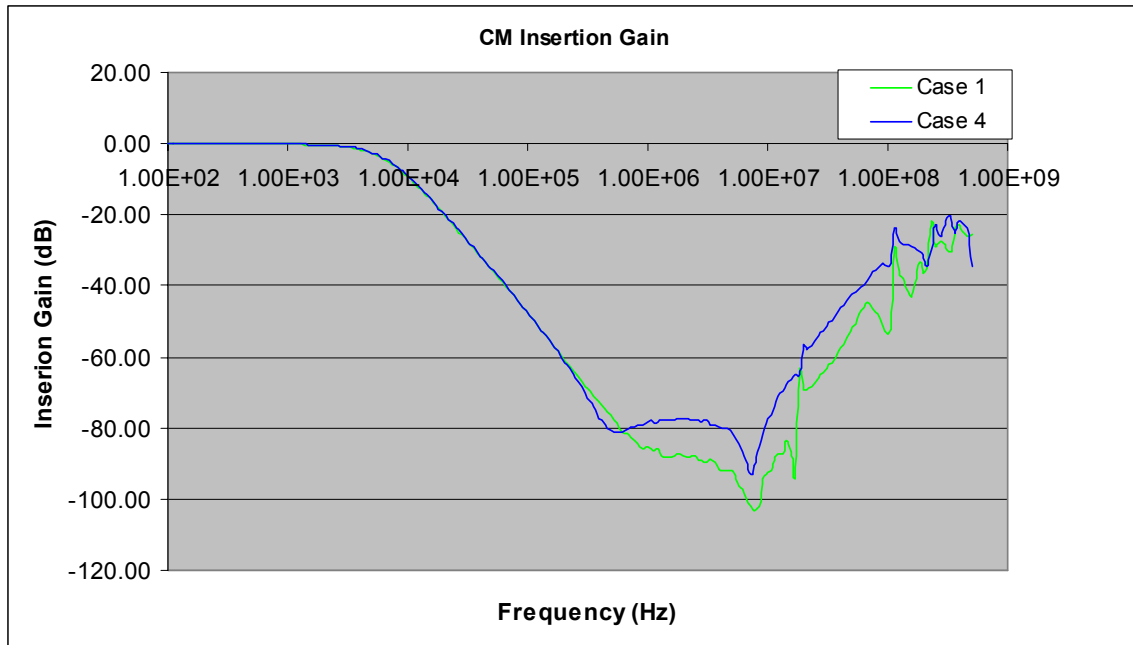


Fig. 5-16: CM insertion gain for case 1 and 2

The large signal tests are shown in Fig. 5-17 and Fig. 5-18 for the CM and DM respectively. It is important to notice in Fig. 5-17 that the smallest EPC in this case doesn't really bring a much better result compared to the insertion gain. The noise is slightly lower at 1 MHz however for higher frequency no differences are noticeable. That could be explained by other effects that take place such as a resonance between the input impedance of the filter and motor drive. The interaction is so high that it could overcome the small difference due to EPC. Finally, in Fig. 5-18 the consequence of leakage is noticeable until 300 kHz, therefore to maximize the leakage inductance and decrease the size the multilayer winding technique is preferred.

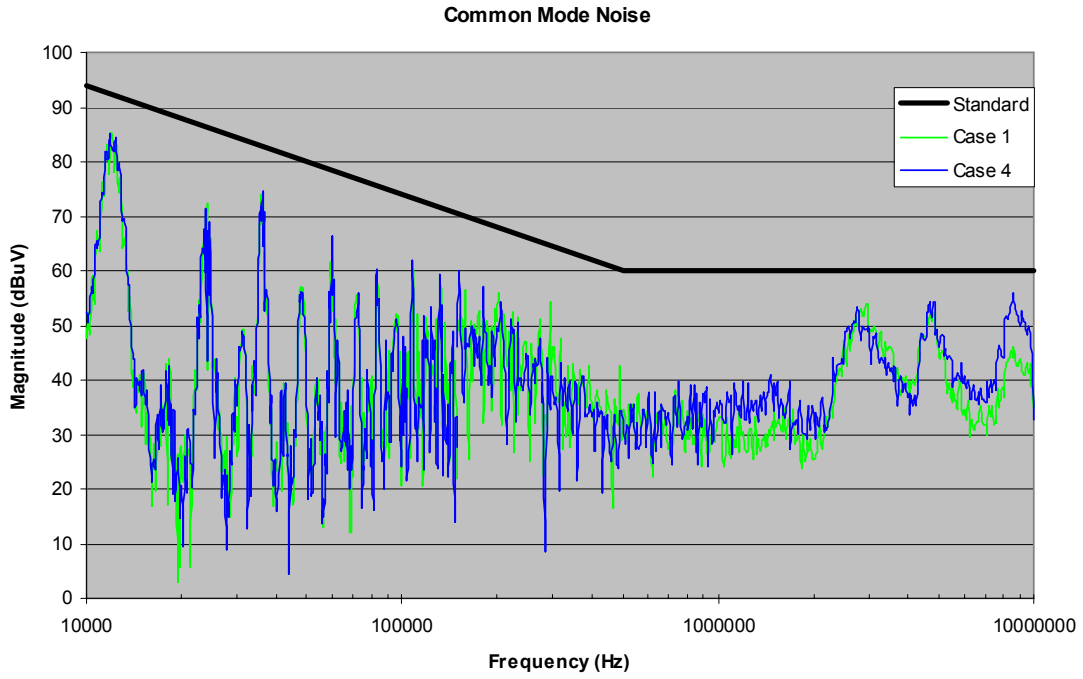


Fig. 5-17: CM noise comparison for case 1 & 4

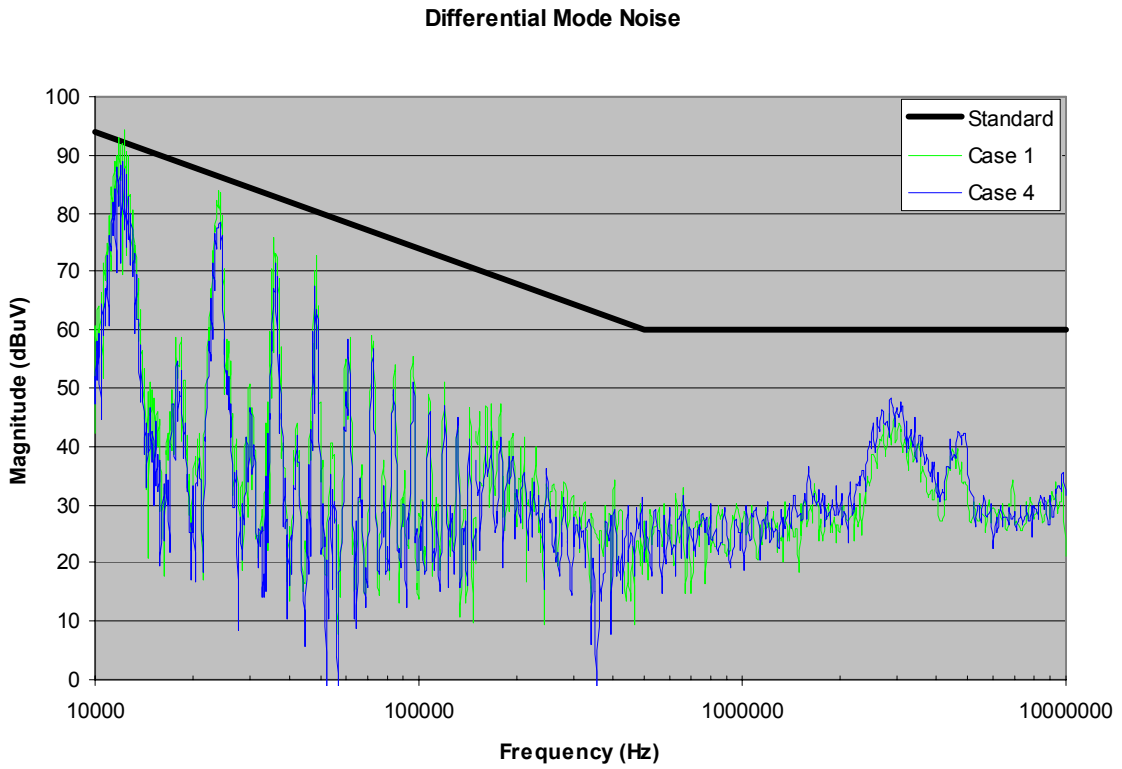


Fig. 5-18: DM noise comparison for case 1 & 4

The final concept that needs to be verified is the EPC cancellation. To check its integrity small signal measurements (CM insertion gain) are made until the appropriate EPC cancellation capacitor is found and then tested in large signal. After multiple tries and error, it turns out that 51 pF was the optimal value for the version studied.

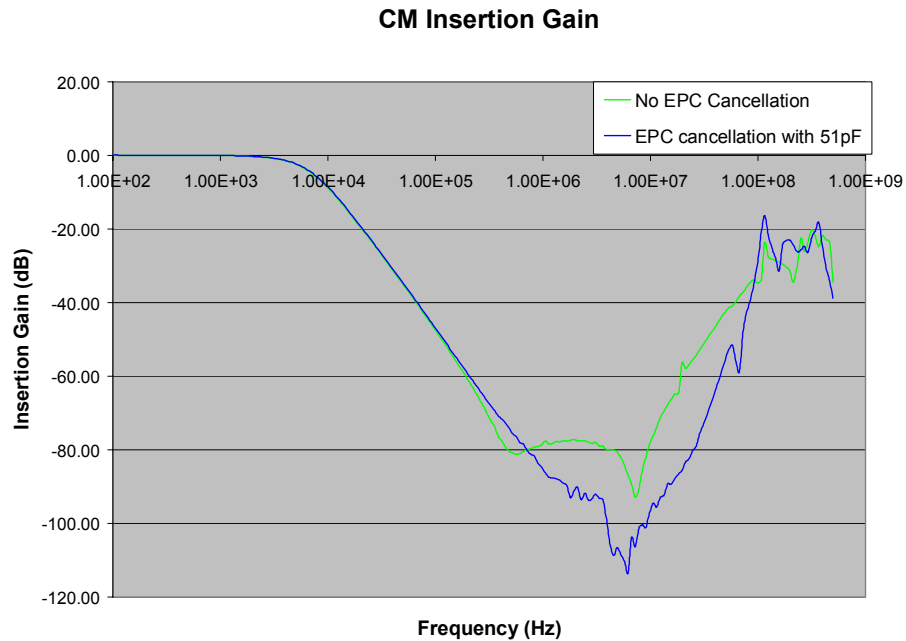


Fig. 5-19: EPC cancellation small signal measurement

The CM insertion gain could be seen in Fig. 5-19 with and without EPC cancellation. It is obvious that the concept of EPC cancellation works in small signal. However, as shown in Fig. 5-20, the power test illustrates the complete opposite where the noise with EPC cancellation is slightly worst. A possible answer to this phenomenon could be explained by a coupling coefficient too small between each half winding. Another reason could be between the relation of small and large signal, it has been shown that the large signal doesn't really follow the small signal perfectly, in other word here we could cancel EPC in small signal but add EPC in large signal. Therefore possible future tasks could be to study the effect of EPC in details and the understanding between small and large signal discrepancy.

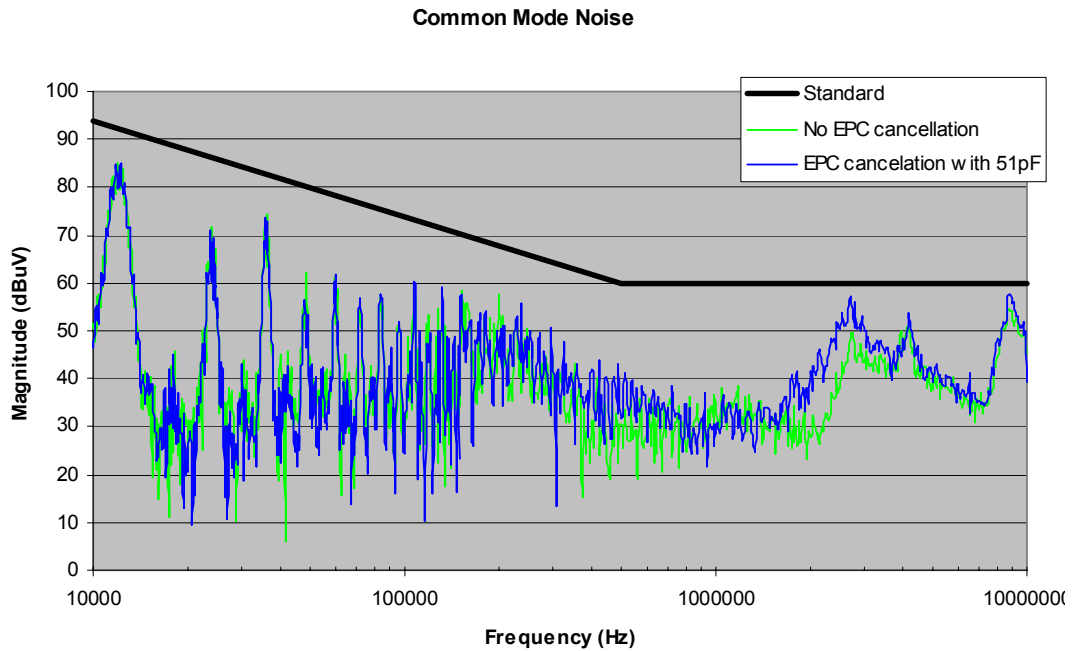


Fig. 5-20: EPC cancellation large signal measurement

ii) Temperature and Saturation

The final measurement and tests will deal with the saturation effect due to the temperature rise of the CM choke due to the loss of winding. The ferrite and nanocrystalline core have been placed in EMI filter and run for different line current operating conditions (6.6 and 8.3 A). When a current of 6.6 A is applied, the temperature raised from 33 °C to a steady 81 °C in 20-30 minutes for both core as shown in Fig. 5-21 and Fig. 5-22 while at 8.3 A the temperature raised from 33 °C to a steady 101 °C Fig. 5-23 and Fig. 5-24. To observe the effect of temperature both time domain and frequency domain have been recorded.

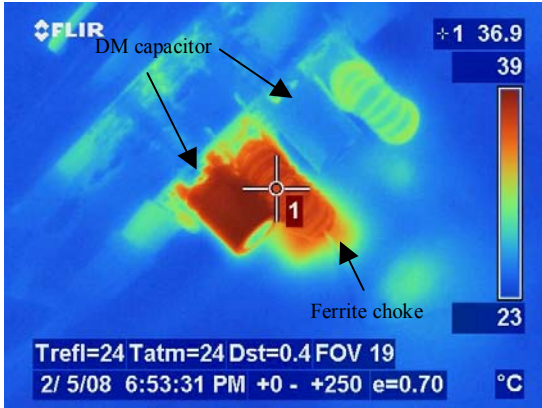


Fig. 5-21: Initial thermal measurement with a 6.6A line current

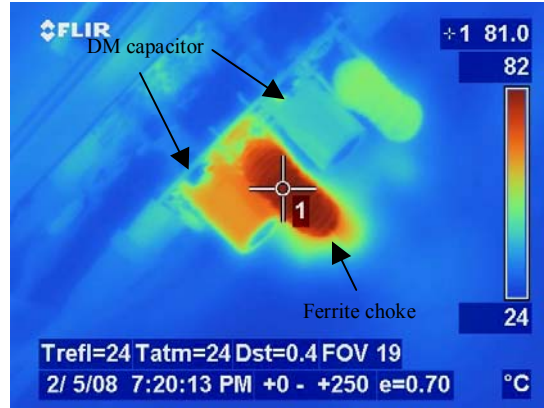


Fig. 5-22: Steady thermal measurement with a 6.6A line current

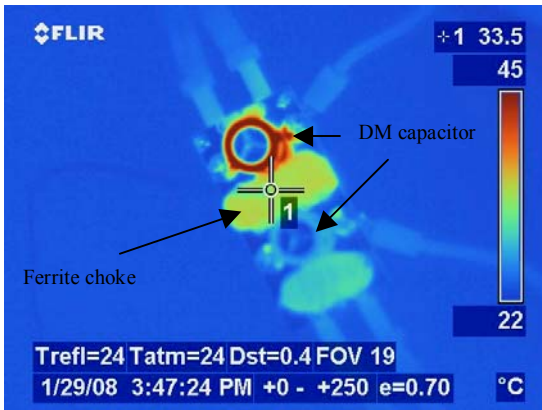


Fig. 5-23: Initial thermal measurement with a 8.3A line current

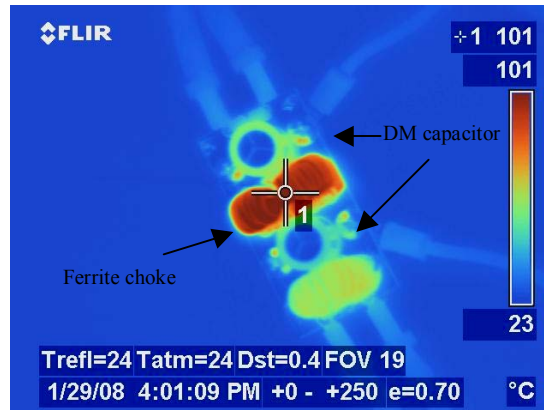


Fig. 5-24: Steady thermal measurement with a 8.3A line current

As shown in the time domain Fig. 5-25 to Fig. 5-28 the CM output current is measured for different temperatures and operating conditions. As noticed the value of the output current is different for both cases since “nano 3” core is used and has a much higher inductance compared to the ferrite. It could be notice in Fig. 5-25 and Fig. 5-26 that when a line current of 6.6 A is used, no big difference could be perceived when the temperature increase. However when the current increase to 8.3A, it could be notice in Fig. 5-27 that the time domain measurement for the ferrite core is completely different and the magnitude increase by almost three when temperature increase. On the other side, the nano-crystalline core doesn't change (cf. Fig. 5-28).

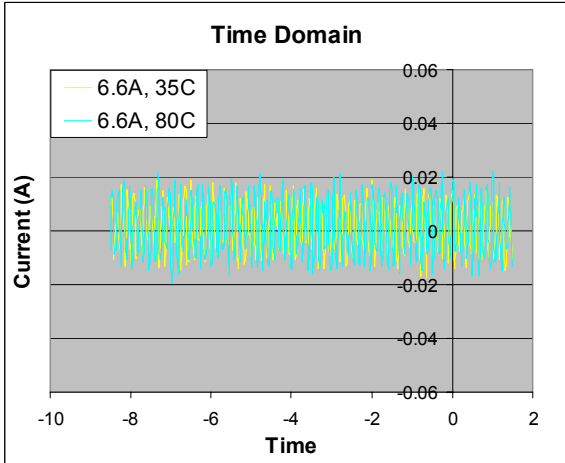


Fig. 5-25: Time domain representation of the CM output current (after filter) for 6.6A line current for ferrite core

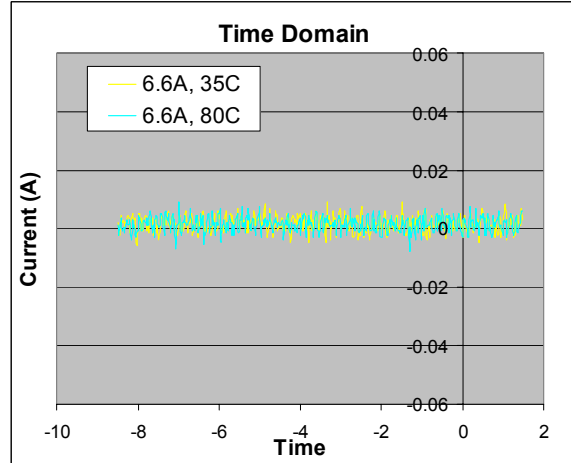


Fig. 5-26: Time domain representation of the CM output current (after filter) for 6.6A line current for nano-crystalline core

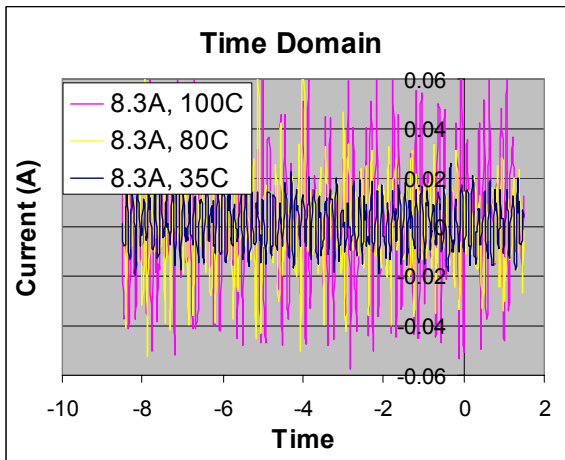


Fig. 5-27: Time domain representation of the CM output current (after filter) for 8.3A line current for ferrite core

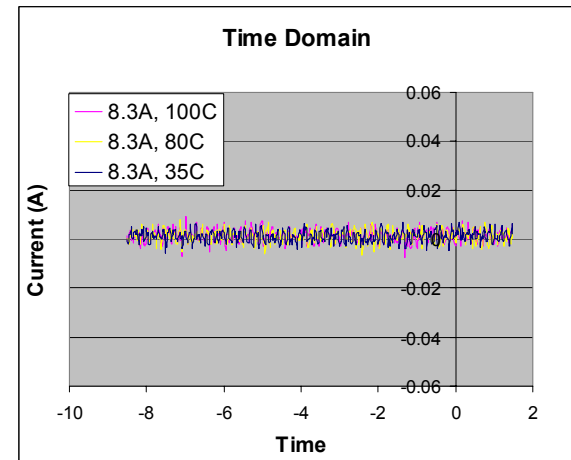


Fig. 5-28: Time domain representation of the CM output current (after filter) for 8.3A line current for nano-crystalline core

DM flux density is calculated for the four cases and summarized in Table 5-4. The ferrite is designed really close to the saturation limit since its optimization constraint is saturation. On the other hand the nano-crystalline constraint is not the saturation but the temperature since the case that is used to protect the core can't handle a temperature higher than 120 °C.

For the case when a current of 6.6 A is used neither core saturate since the core temperature reach 80 °C and both flux densities are below the limit. Nonetheless, for the 8.3A case the ferrite core is working properly at low temperature since the core saturation

flux density is above 0.4T but as soon as it reached 80 °C the core saturation density drop below 0.3T and the core saturate (cf. Table 5-5).

Table 5-4: DM flux density for two line current cases

Core Type	Line current = 6.6A	Line current = 8.3A
Ferrite	$B_{DM} = \frac{19E^{-6} \times 6.6}{24 \times 22.2E^{-6}} = 0.235T$	$B_{DM} = \frac{19E^{-6} \times 8.3}{24 \times 22.2E^{-6}} = 0.295T$
Nano-crystalline	$B_{DM} = \frac{54E^{-6} \times 6.6}{36 \times 37.0E^{-6}} = 0.267T$	$B_{DM} = \frac{54E^{-6} \times 8.3}{36 \times 37.0E^{-6}} = 0.336T$

Table 5-5: Core saturation flux density in function of temperature

Core Type	30 °C	80 °C	100 °C
Ferrite	0.41 T	0.3 T	0.24 T
Nano-crystalline	1.23 T	1.21 T	1.20 T

Common Mode Noise with Ferrite Core

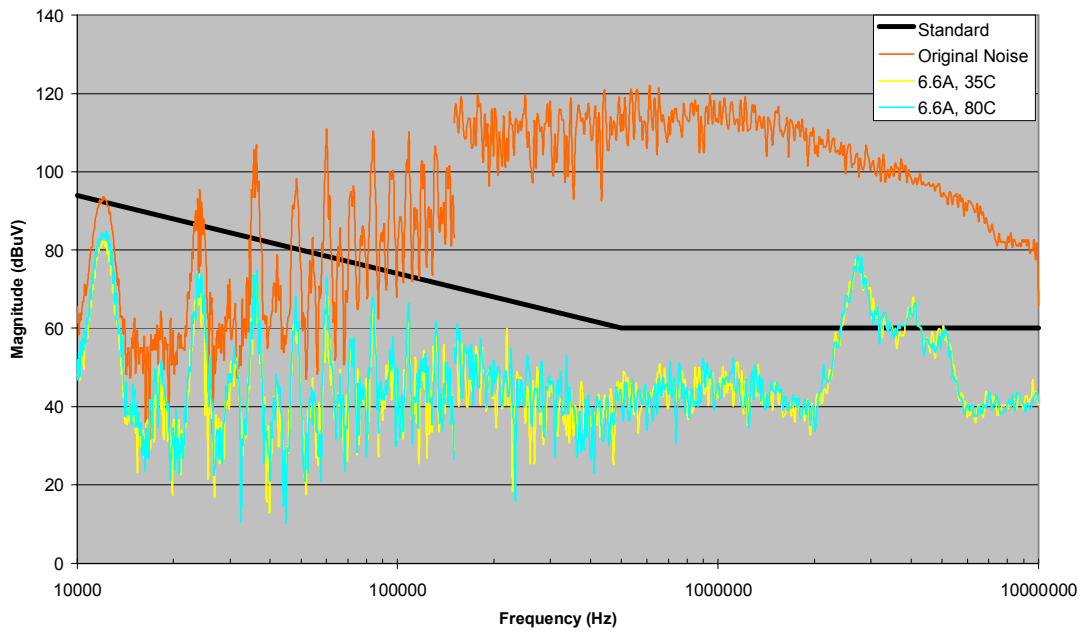


Fig. 5-29: Temperature effect on CM noise for 6.6A line current and ferrite core

Common Mode Noise with Ferrite Core

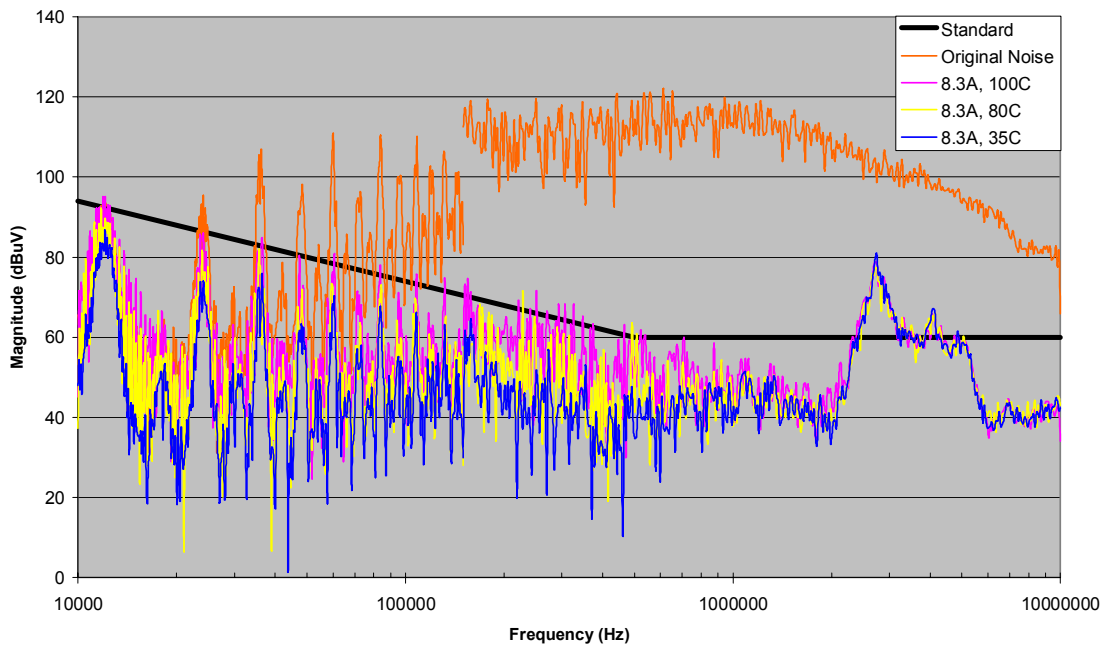


Fig. 5-30: Temperature effect on CM noise for 8.3A line current and ferrite core

Common Mode Noise with Nano-Crystalline Core

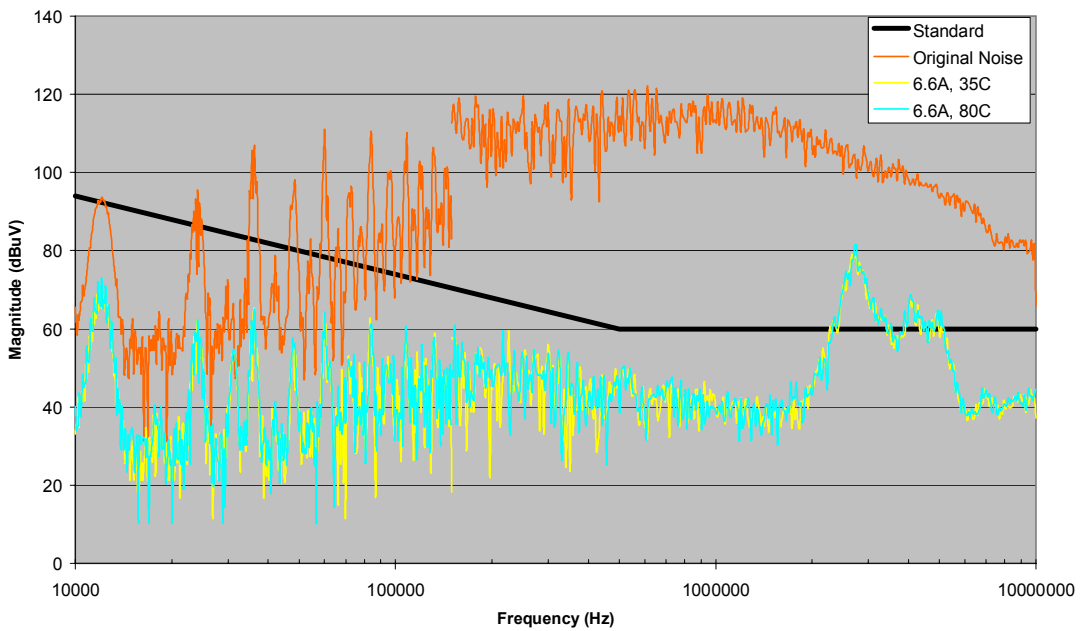


Fig. 5-31: Temperature effect on CM noise for 6.6A line current and nano-crystalline core

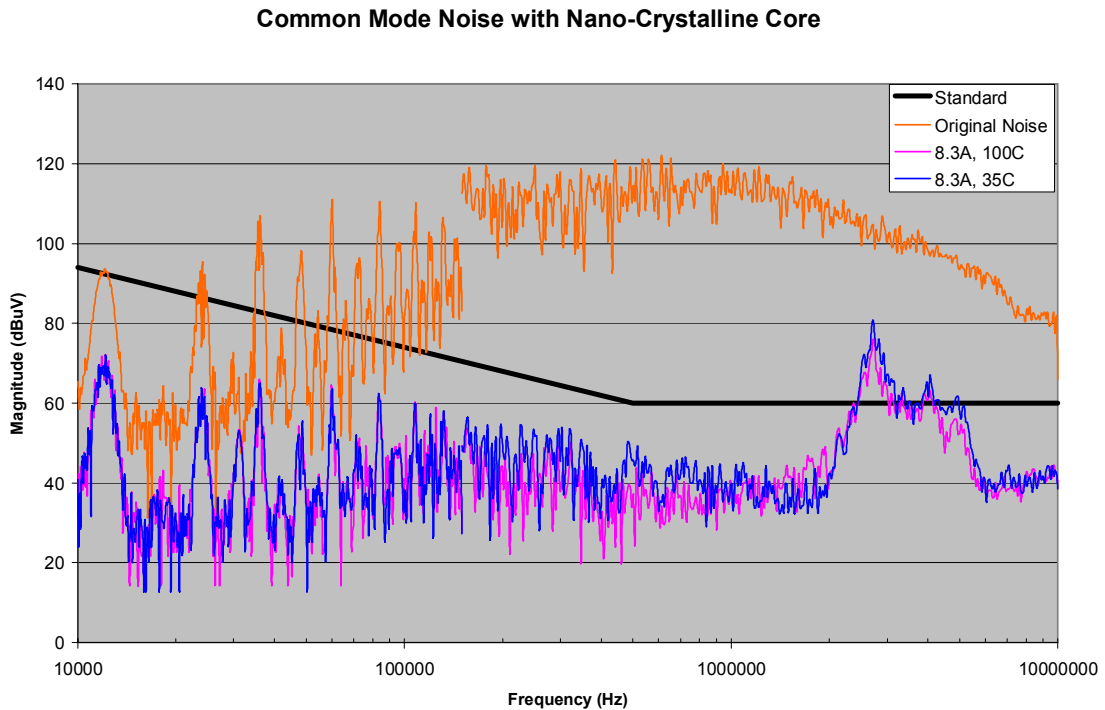


Fig. 5-32: Temperature effect on CM noise for 8.3A line current and nano-crystalline core

To finalize the experiment, the noise is measured in frequency domain for the previous cases. The ferrite core behaves normally and meets the low frequency standard for both low and high temperature when the line current is 6.6A (cf. Fig. 5-29). However for a higher current, and an increased in temperature the CM noise rise of 10 to 15 dB at low frequency and exceed the limit (cf. Fig. 5-30). The nano-crystalline core in the other side doesn't saturate for any cases as shown in Fig. 5-31 and Fig. 5-32.

IV. Integrated CM and DM Inductor

As already mentioned, the EMI filter size reduction is mainly possible by looking at the tradeoffs existent between components and the application where the filter is used. The two main obstacles in a small EMI filter are the CM choke and the DM capacitor that could be of significant size. To reduce the size of the DM capacitor is generally possible by reducing the required DM capacitance and therefore increasing the total DM inductance. However, since the leakage from the CM choke cannot be increased arbitrarily, it is a common practice to add DM inductances in series with the CM choke,

at the expense of an increased total volume of the filter. A possible solution is the integration of the CM and DM inductor. Some research have been developed on integration method however no real technique allow size reduction and improve performance. Reference [25] integrates the DM and CM suppression function with only one ferrite core and one powder core. But the winding structure is asymmetrical. The asymmetrical structure may lead to unbalanced leakage inductance, which will impact the performance of the EMI filter at high frequency range. Another technique integrates one high permeability core and two low permeability cores [26]. Although the inductor volume can be reduced by this approach, the number of components does not decrease compared to the discrete structure.

This research proposes a new approach for the DM and CM chokes integration. Compared with the previous works, both inductor volume and DM inductance are optimized and the winding angle for each side is symmetrical. Two versions of the integration method are built which integrate a low permeability Kool Mu core with either ferrite or nano-crystalline core. Theoretical analysis is firstly carried out follow by small and large signal measurement. The experimental results verified the performance, symmetry and thermal behavior of the integrated structure.

A. Structure Analysis

As stated above two integrated versions have been developed, one integrating a ferrite and Kool Mu core and the other one integrating a nano-crystalline and Kool Mu core. The following analysis focus on the first integration however since their structures are similar the same investigation could be made for the second version.

Fig. 5-33 shows the layout and winding of the integrated EMI choke. It consists of a high permeability core and a low permeability core. For comparison, Fig. 5-34 shows the common discrete version EMI chokes which include one high permeability core and two low permeability cores. In the proposed structure, the low permeability core is fixed within the window of the high permeability core. For the phase AB, the two cores share the same winding while for the other phase CD, the wire is wound in the shape of “∞” while it crosses both cores.

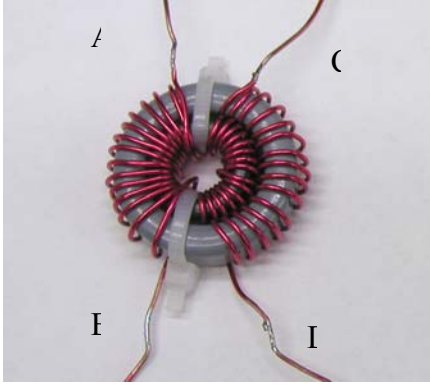


Fig. 5-33: Integrated EMI choke

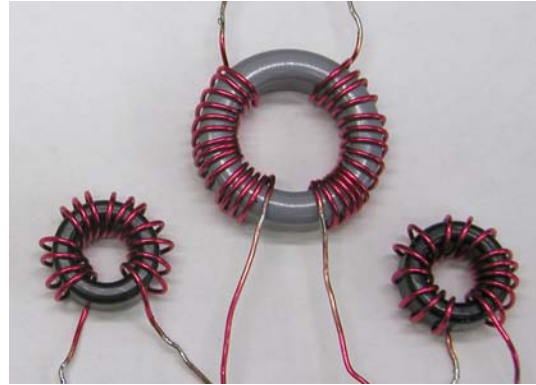


Fig. 5-34: Discrete EMI choke

Fig. 5-35 shows the cross-sectional diagram and the flux direction of the integrated choke. As can be seen, the magnetic fields in the inner core will be canceled by each other while there is CM current going through the two phases (5-12). The integrated choke will then behave the same as a single core common mode choke (5-11). And the CM inductance is given by equation (5-9) where N is the number of turns for each phase, R_l is the magnetic reluctance of the outer core.

$$L_{CM} = \frac{N^2 A_l}{1000^2} = \frac{N^2}{\frac{l}{\mu_0 \mu_r A}} = \frac{N^2}{R_l} \quad (5-9)$$

Similarly, when the DM current goes through the two phases, the flux in the outer core will be canceled except the leakage (5-13), while the magnetic fields generated in the inner core are in the same direction (5-14). Therefore it can achieve higher DM inductance with fewer cores compared with the discrete version shown in Fig. 1 (b). The DM inductance can be given by (5-10) where $L_{total\ leakage}$ is the total leakage inductance of the outer choke, R_2 is the magnetic reluctance of the inner core. The equivalent circuit of the integrated choke can be shown in Fig. 5-36. Although the DM inductors of the discrete version could be also implemented by only one low permeability core, the proposed integration structure still excels since it can fully utilize the window space of the CM choke and reduce the length of the copper wire.

$$L_{DM} = L_{total\ leakage} + \frac{(2N)^2}{R_2} \quad (5-10)$$

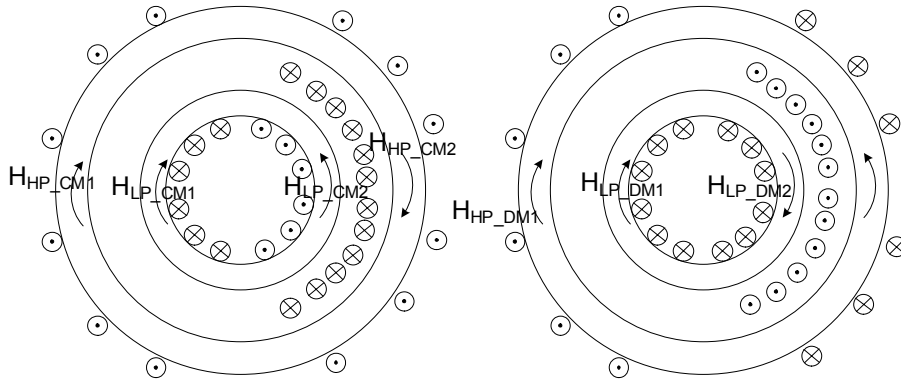


Fig. 5-35: Magnetic field intensity for CM current (left) and DM current (right) in integrated choke

For the high permeability core:

$$\sum \phi_{CM} = \phi_{CM1} + \phi_{CM2} = 2\phi_{CM} \quad \text{with } \phi_{CM1} = \phi_{CM2} \quad (5-11)$$

$$\sum \phi_{DM} = \phi_{DM1} - \phi_{DM2} = 0 \quad \text{with } \phi_{DM1} = \phi_{DM2} \quad (5-12)$$

And for the low permeability core:

$$\sum \phi_{CM} = \phi_{CM1} - \phi_{CM2} = 0 \quad \text{with } \phi_{CM1} = \phi_{CM2} \quad (5-13)$$

$$\sum \phi_{DM} = \phi_{DM1} + \phi_{DM2} = 2\phi_{DM} \quad \text{with } \phi_{DM1} = \phi_{DM2} \quad (5-14)$$

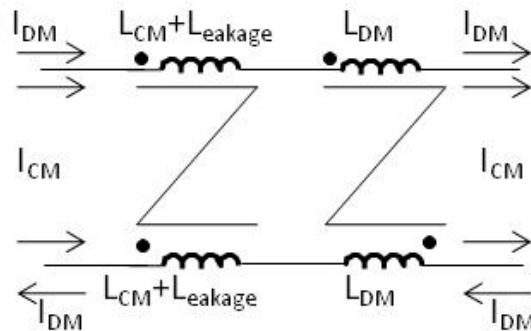


Fig. 5-36: Equivalent circuit for the new structure

The same integrated structure has also been tried using a nano-crystalline core to compensate for its small leakage. Fig. 5-37 show an experimental result of the structure. Compared to the ferrite version, the Kool Mu core cannot be integrated inside the outer core since the open window of nano crystalline core is really small due to the protective case. Therefore, it has been chosen to integrate them side by side. Even though the size reduction is smaller than the previous case, the copper needed is less, its behavior in large signal is better since more turns could be implemented and more DM inductance is providing. It will be use in the last version of the filter to meet the standard and compare with the baseline design.

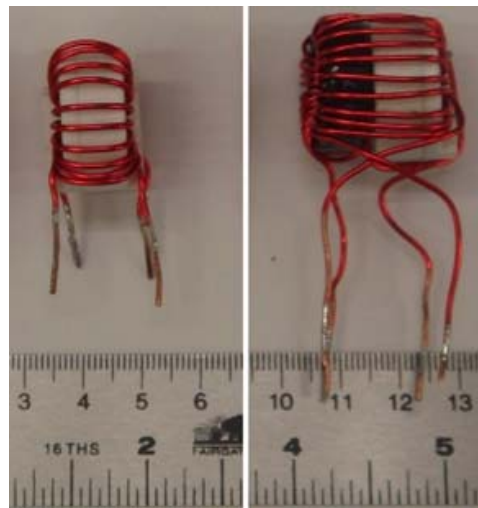


Fig. 5-37: Integrated EMI choke with nano crystalline core and Kool Mu

B. Measurements Verification

In order to verify the design concept, an integrated choke and the corresponding discrete chokes are built for test and comparison. Ferrite core and Kool Mu core are used as the high permeability core and low permeability core respectively. Table I shows the structure specification at 10 kHz. As can be seen, both the wire length and the volume are reduced for the integrated choke. The DM inductance of the integrated choke increased a lot compared to the discrete version. The CM inductance also shows small difference, which is due to the permeability variation from core to core. Fig. 5-38 and Fig. 5-39 show the impedance measurement results. The DM impedance of the integrated choke shows higher value up to 16 MHz while the CM impedance has similar performance. The small measurement results agree with the analysis in the previous section.

Table 5-6: Structures specification at 10 kHz

	Number of Turns	Wire length	Volume	CM inductance	DM inductance
Integrated Choke	15	117 cm	5.7 cm ³	700 μH	48.2 μH
Discrete Chokes	15	140 cm	9.5 cm ³	732 μH	28.7 μH

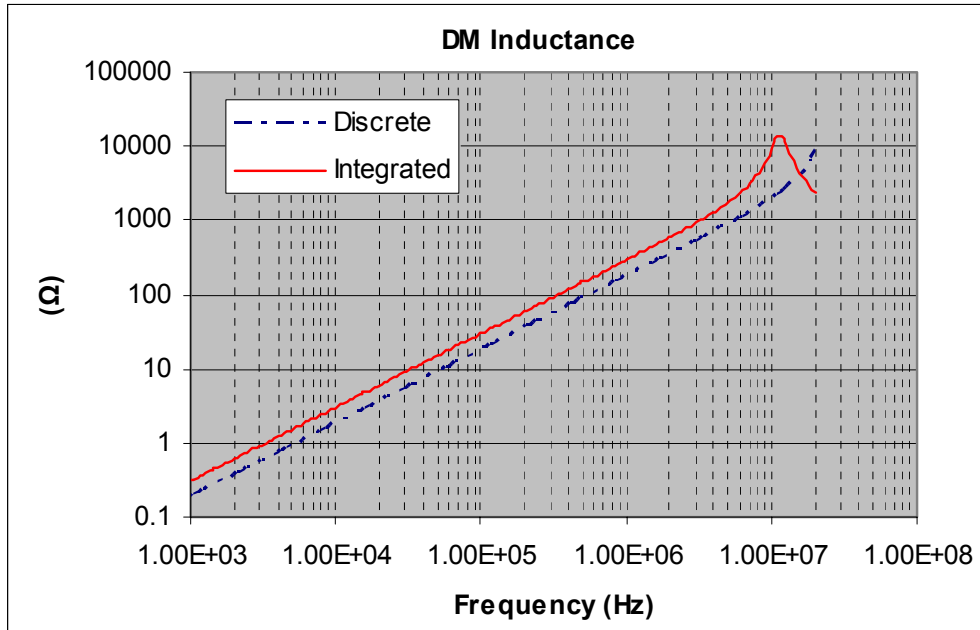


Fig. 5-38: DM inductance of both structures

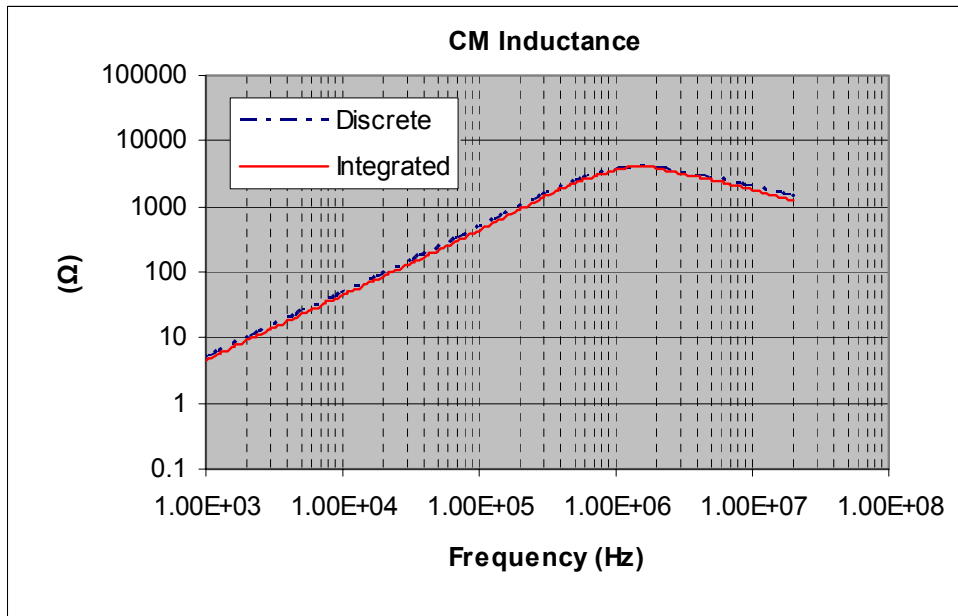


Fig. 5-39: CM inductance of both structures

Another concern for the integrated choke is the impedance balance. Unbalance impedance can cause the coupling between the CM noise and DM noise, which will impact the performance of the EMI filter [50]. A 4-port network analyzer is used to measure the transfer gain between CM and DM of the integrated choke. The measurement results are shown in Fig. 5-40 and Fig. 5-41. As can be seen, the transfer gain between CM and DM is less than -75 dB in the whole measurement range which certifies that the structure is well balanced. By definition if either noise are not 75 dB higher than the other one, no effect will be perceive.

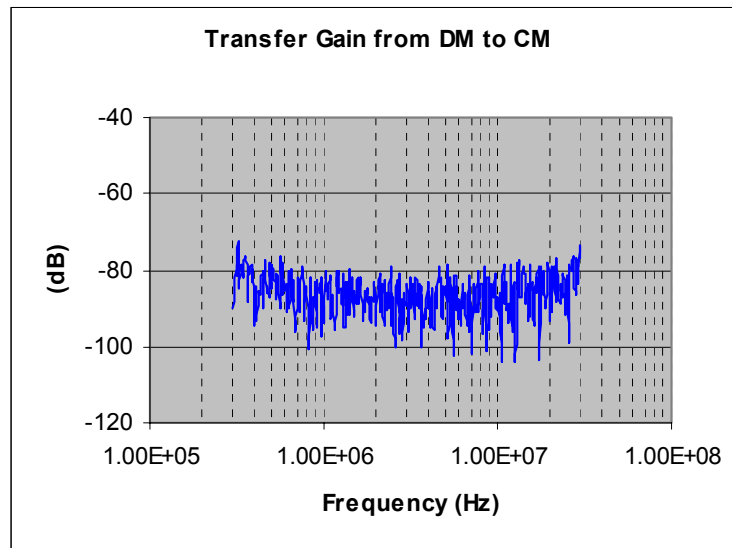


Fig. 5-40: Transfer gain from DM to CM for integrated structure

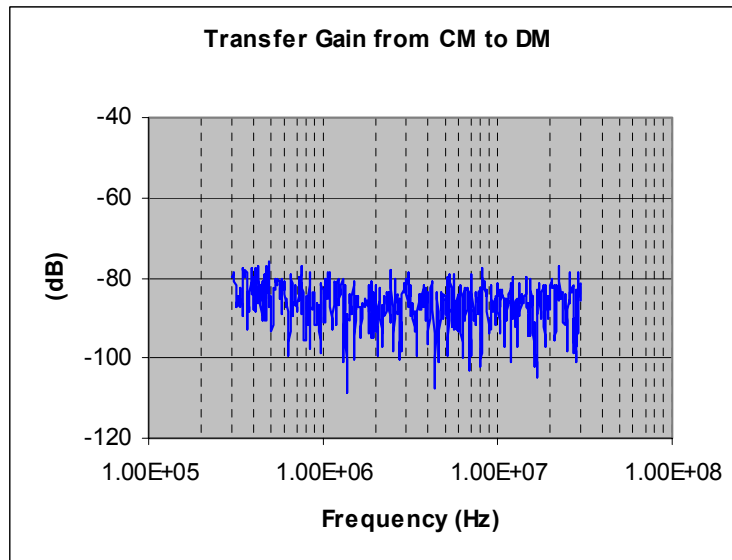


Fig. 5-41: Transfer gain from CM to DM for integrated structure

Both structures are implemented into the same EMI filter and run in power test. The experimental results Fig. 5-42 show that in the frequency range from 10 kHz to 500 kHz the EMI filter with integrated choke shows 8-15 dB improvement for the DM noise compared to the EMI filter with discrete chokes, which is due to the higher DM inductance. In higher frequency range, the two EMI filters have similar DM attenuation. Fig. 5-43 also indicates that the integrated structure will not impact the CM performance.

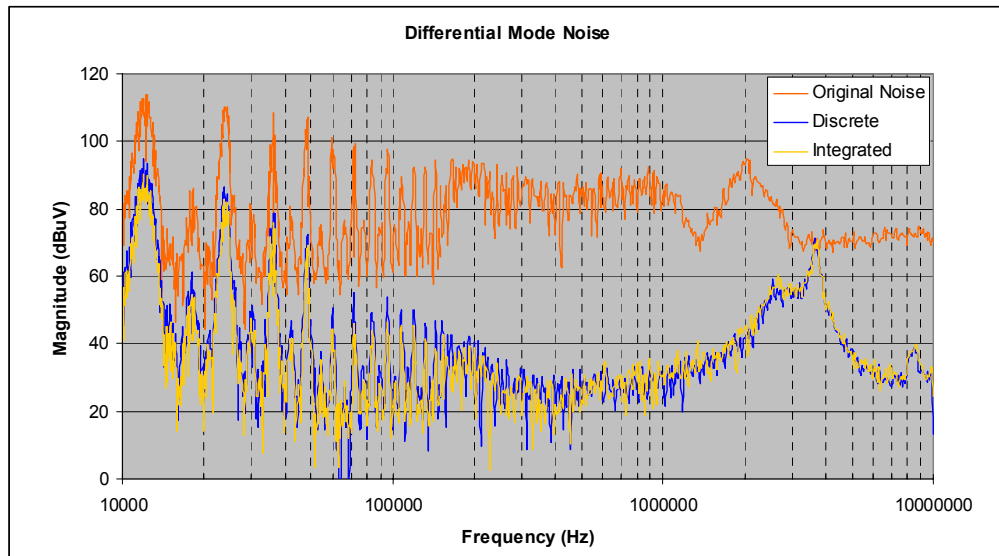


Fig. 5-42: DM noise measurement for both structures

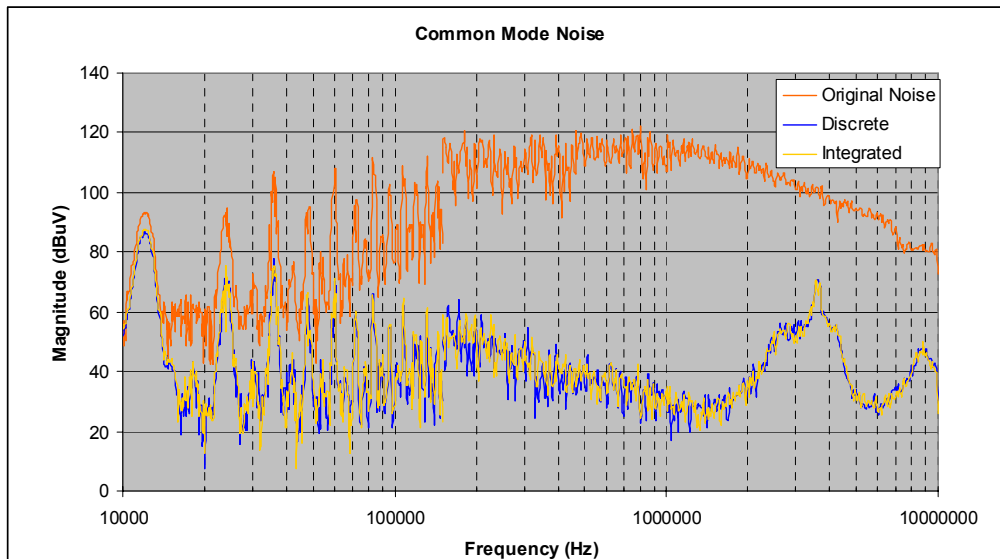


Fig. 5-43: CM noise measurement for both structures

Finally, Fig. 5-44 and Fig. 5-45 show the steady state temperature measured by the thermal camera. The DM capacitor close to the motor drive is the hottest component in both cases. The temperature of the hot spot in the integrated choke is only about 2-3°C higher than the one in the discrete chokes. More detail results and analysis will be included in the final paper.

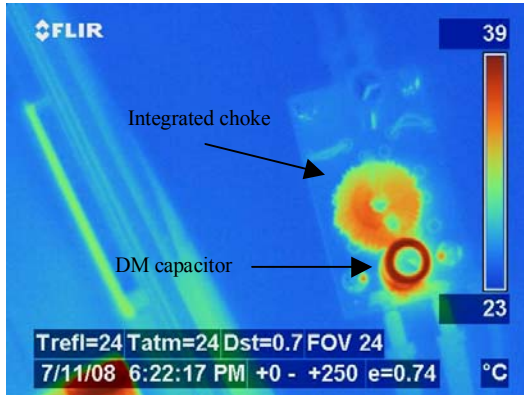


Fig. 5-44: Thermal measurement for the EMI filter with integrated choke

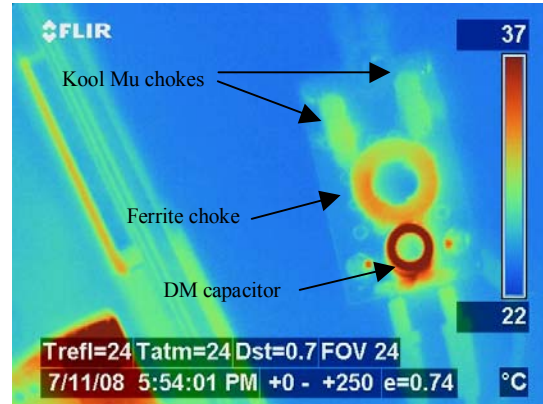


Fig. 5-45: Thermal measurement for the EMI filter with discrete chokes

C. Conclusion

A novel approach for the CM and DM chokes integration has been presented. The proposed structure features low volume, reduced copper wire length and good impedance balance. A prototype is built and the design concept is verified by both small signal measurement and large signal test. When compared to the discrete version, the integrated choke shows a 40 percent volume reduction and a 16 percent copper wire reduction without degrading EMI performance or causing thermal issues.

V. Capacitor Impact on Size and Performance

During the design stage it is important to choose the appropriate components in order to avoid trouble shooting during the verification stage. It has been already discussed that capacitor with high frequency behavior such as ceramic capacitor is recommended. Furthermore, the high capacitance requirement leads to the use of a high dielectric constant such as the “X7R” technology.

When the capacitance value is known, it is important to take into account that the capacitance typically fall off due to either an increased in temperature or voltage. And the

industry standard for ceramic capacitors is that the capacitance value of an “X7R” dielectric is based on the reading at 25 °C at 1.0 V_{RMS} at 1 kHz. Moreover, the higher the dielectric constant of the dielectric, the more the capacitance value drops off. Therefore for “X7R” dielectric material a large margin need to be considered to compensate for this drop. The curve in Fig. 5-46 provided by a manufacturer shows the typical capacitance at a certain voltage for an “X7R” material “BX” material not considered here. It could be noticed for example that at 300V the capacitance change is -70% which will greatly affect the EMI noise measurement.

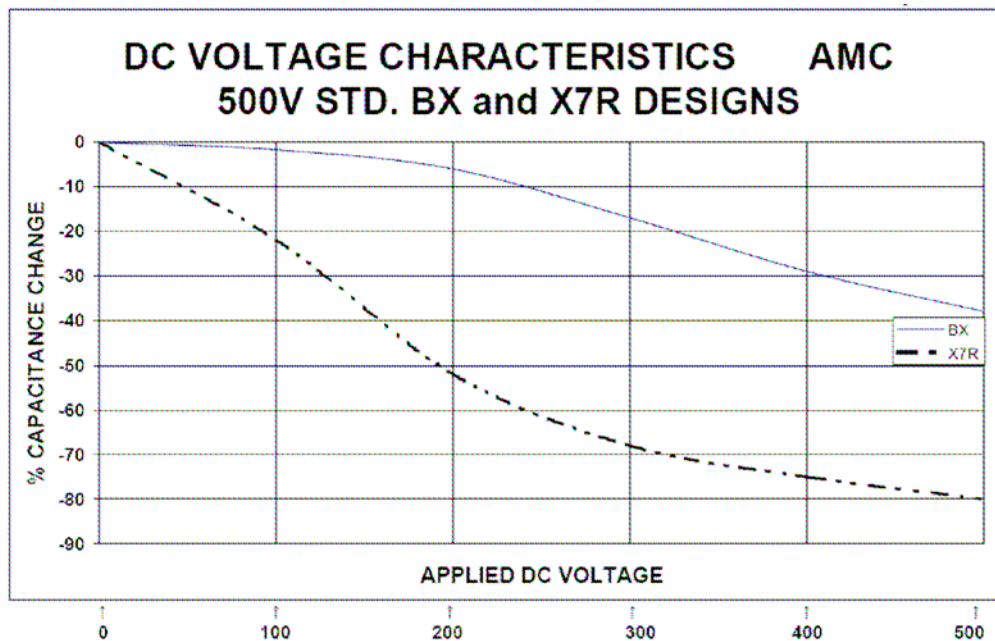


Fig. 5-46: “X7R” capacitance behavior in function of DC voltage

To check the integrity of this fact two tests have been done one comparing two “X7R” CM capacitor that have different voltage rating and the other one evaluating the performance between electrolytic and ceramic DM capacitor for the same rated capacitance.

As shown on the small signal measurements of the impedance and insertion gain on Fig. 5-47 and Fig. 5-48 respectively, no real difference could be notice except some difference in equivalent series inductor that affect the resonance point. However, on the power test of Fig. 5-49 a big disparity up to 20dB is visible at low and high frequency.

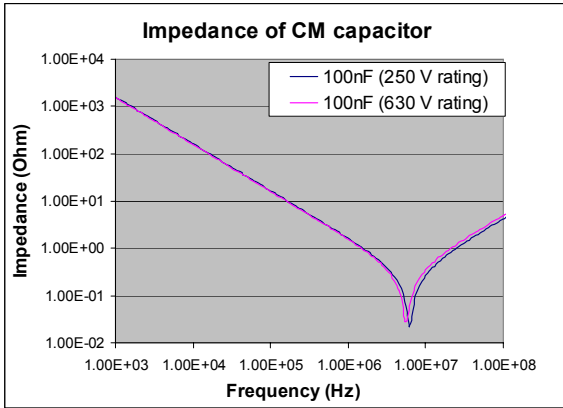


Fig. 5-47: Impedance comparison for 100 nF ceramic capacitor and different voltage rating

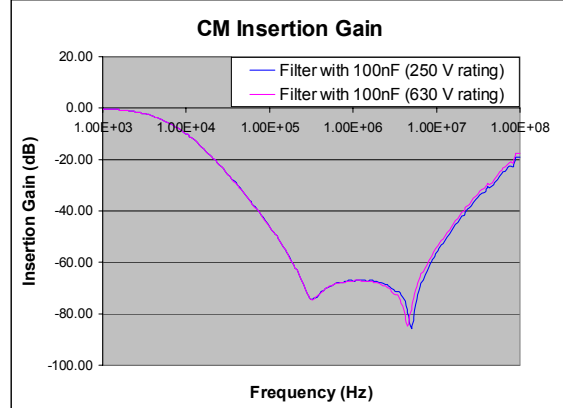


Fig. 5-48: CM Insertion gain comparison of filter with 100 nF ceramic capacitor and different voltage rating

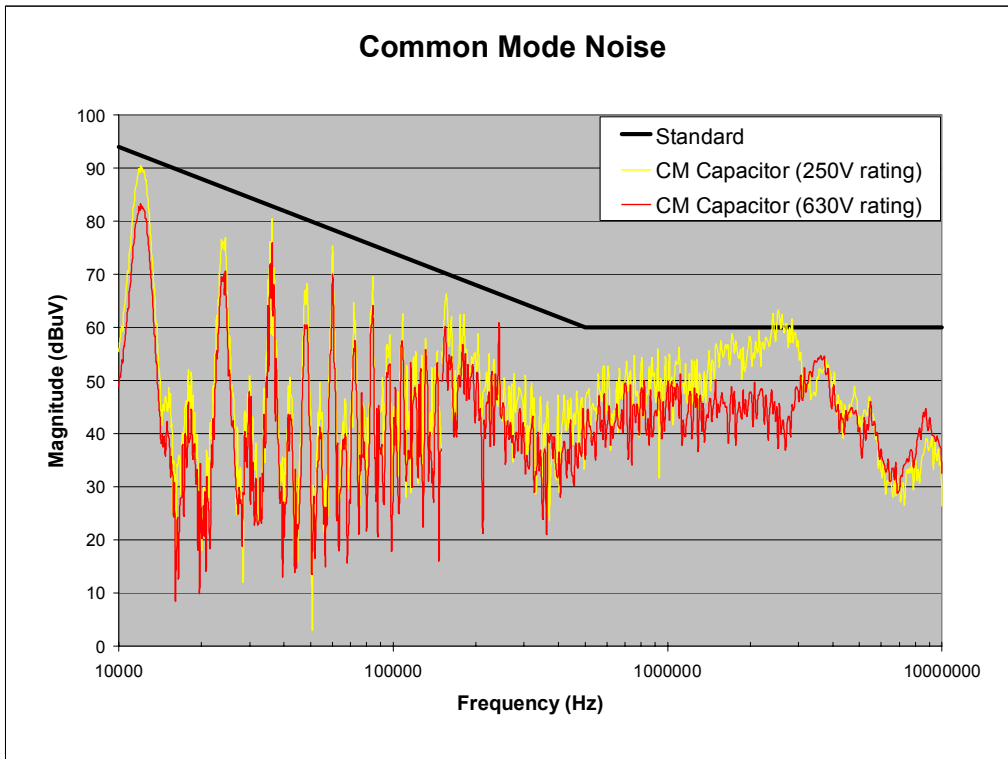


Fig. 5-49: CM noise measurement of filter with 100 nF ceramic capacitor and different voltage rating

The final example illustrates the importance of the huge capacitance drop of “X7R” ceramic capacitor by comparing a filter with two 33 μ F DM capacitor using either electrolytic or ceramic capacitor. The electrolytic capacitor has a voltage rating of 350 V while the ceramic capacitor voltage rating is 500 V. The impedance of both capacitors is shown again in Fig. 5-50 while the important difference in DM insertion gain is in

evidence Fig. 5-51. From the small signal point of view the ceramic capacitor is much better than electrolytic. On the other hand, on the large signal measurement of Fig. 5-52 it is clear that the noise is much higher in low frequency when the ceramic capacitor is used. A 20 dB difference is observed at 12 kHz.

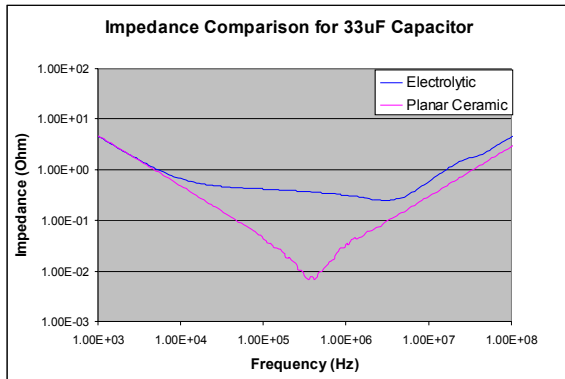


Fig. 5-50: Impedance of 33 μ F electrolytic and ceramic DM capacitor

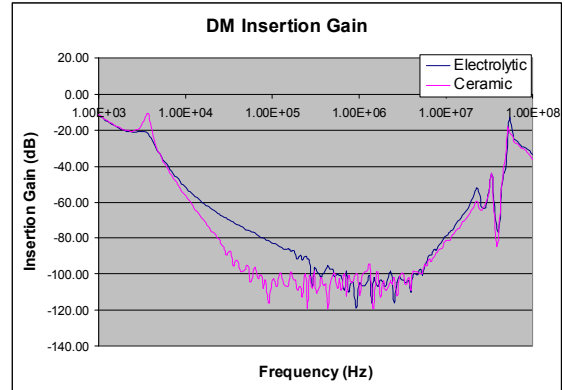


Fig. 5-51: DM Insertion gain comparison of filter with 33 μ F electrolytic and ceramic capacitor

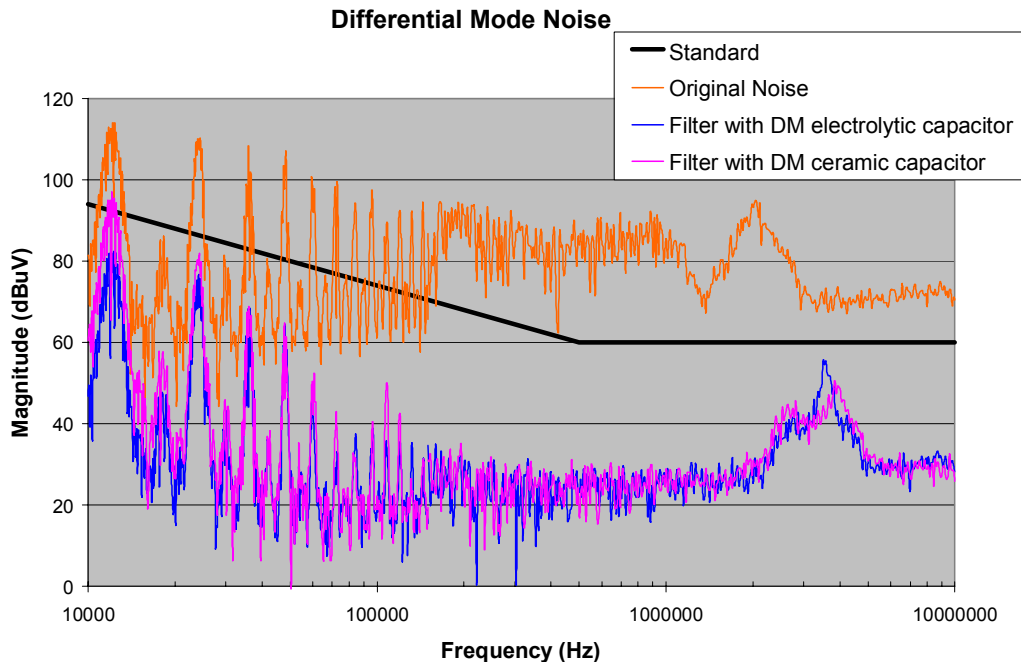


Fig. 5-52: DM noise of EMI filter with electrolytic or ceramic capacitor

Ceramic capacitors improve the performances of CM and DM filters however their capacitance drop need to be taken into account in the design stage. It won't generally be an issue for CM capacitors since their capacitance value are small and finding a higher voltage rating won't impact the size too much. In contrary the DM capacitor have really high inductance and voltage requirement so if margin is considered to compensate for the capacitance drop then the size of the capacitor will be huge. It might also be difficult to

find capacitors with high capacitance and high voltage rating. In this case 500 V was the maximum voltage rating the manufacturer could provide for 33 μF .

VI. Final Design Approach and Latest Filter Version

To minimize the total size of EMI filter, it is a necessity to choose the correct filter components and use them close to their limits (electrical, thermal, mechanical). However, knowing the filter application and environment is also very important during the design stage since the running conditions, temperature and norms will impact the design process. The best filter topology for one application may not be the best for other applications. For example in aerospace application the use of electrolytic capacitor is not allowed and multi-layer ceramic capacitors need to be used. Therefore the DM capacitor becomes the major constraint and the filter volume increase. It could be then a good approach to change the filter topology to multi-stage DM filter to reduce the required DM capacitance.

In this study the best appropriate technology for the CM choke appears to be the nanocrystalline core due to the big CM inductance requirement and the expected high core temperature that would have saturated ferrite material. Its poor performances in the middle range frequency could be easily compensated by increasing the number of turns slightly which will make the LF CM noise even lower. Multi-layer windings have been proven to be a reliable method to decrease the volume of the CM choke. Even though an increase of EPC is expected, its impact on the noise is negligible compared to the huge benefits in size. In this case with the stringent standard starting at 10 kHz and the possibility to use electrolytic technology for DM capacitor, it is not a profit to use multi-stage filter that could bring to other drawbacks such as grounding or coupling. Finally, the novel integrated technology using ferrite material have been proven to reduce the size considerably, however in this case it might not bring a smaller volume due to the high CM inductance. It is therefore better to use the second integrated approach (nanocrystalline core and kool μ) which has a larger volume but achieve much higher CM and DM inductance. The final procedure to design a high-density EMI filter for the previous application is summarized in the following flow chart.

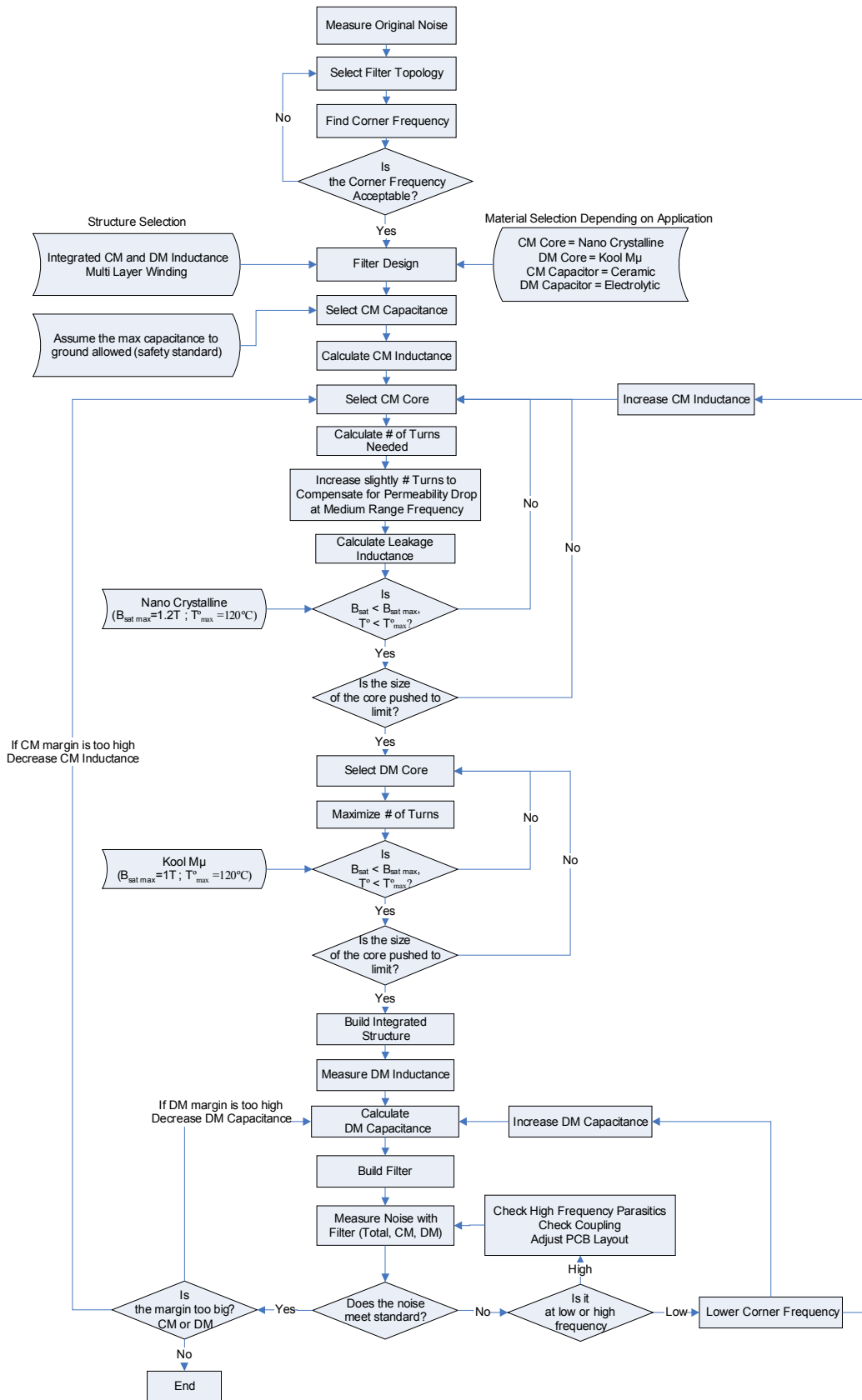


Fig. 5-53: Flow chart of the design procedure of an EMI filter

The final filter has the same topology as the baseline filter, only the components value and structure of the choke is different. Table 5-7 regroups the components specifications between the baseline filter and the final version. The filter has a length of 6.8 cm, width of 3.2 cm, and height of 3.0 cm which leads to a total volume of 65.3 cm³. The total volume compared to the baseline filter is approximately reduced by three.

Table 5-7: Baseline and final filter specifications

	Baseline Filter	Final Version
CM Choke	≈3 mH @ 5 kHz	≈20 mH @ 5 kHz
DM Inductance	40 μH	116 μH
CM Capacitance (C _y)	2x100 nF	2x100 nF
DM Capacitance (C _{x1} , C _{x2})	2x150 μF	2x33 μF



Fig. 5-54: Picture of final version of filter

The final filter version of Fig. 5-54 leads to the small and large signal measurements showed in Fig. 5-55, Fig. 5-56 and Fig. 5-57, Fig. 5-58 respectively which also show the baseline measurement as comparison. It is clear that the CM results are much better due to the nano crystalline core that has a much higher inductance at low frequency. The DM filter has been compensated by decreasing the C_x's capacitor and increasing the total DM inductance by adding an extra Kool Mu core which is integrated to the CM choke. It is obvious that the DM result is almost similar to the baseline design but with a lower volume.

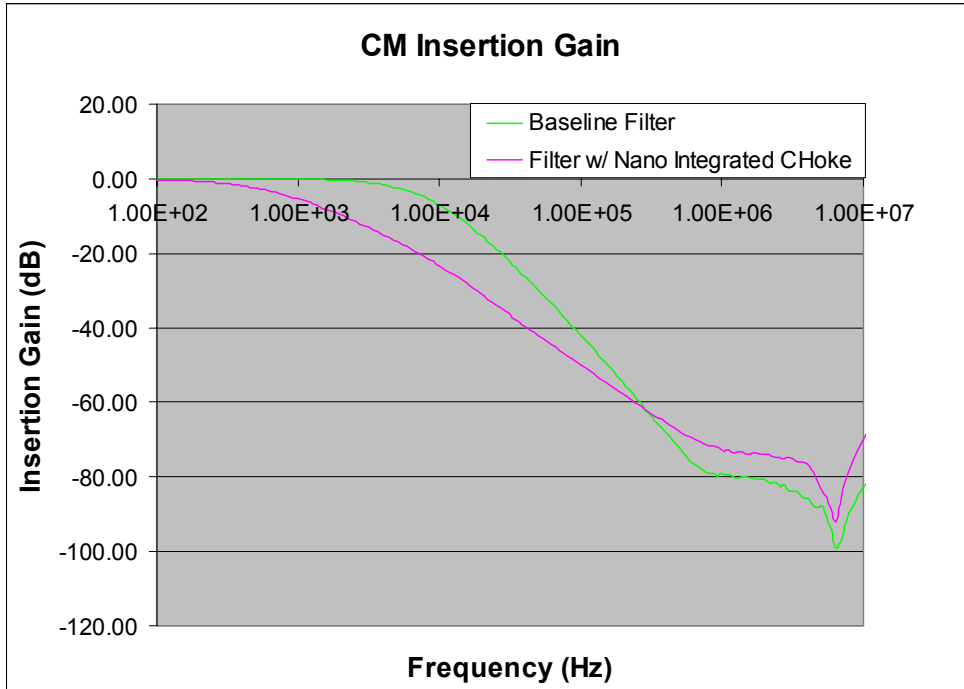


Fig. 5-55: CM insertion gain for baseline and final version of filter

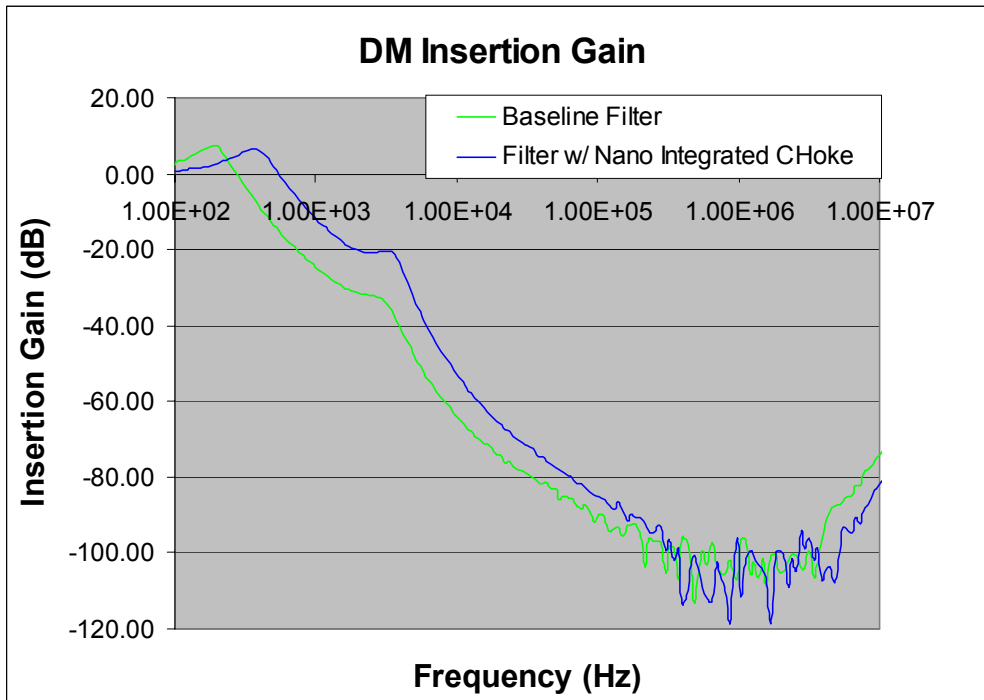


Fig. 5-56: DM insertion gain for baseline and final version of filter

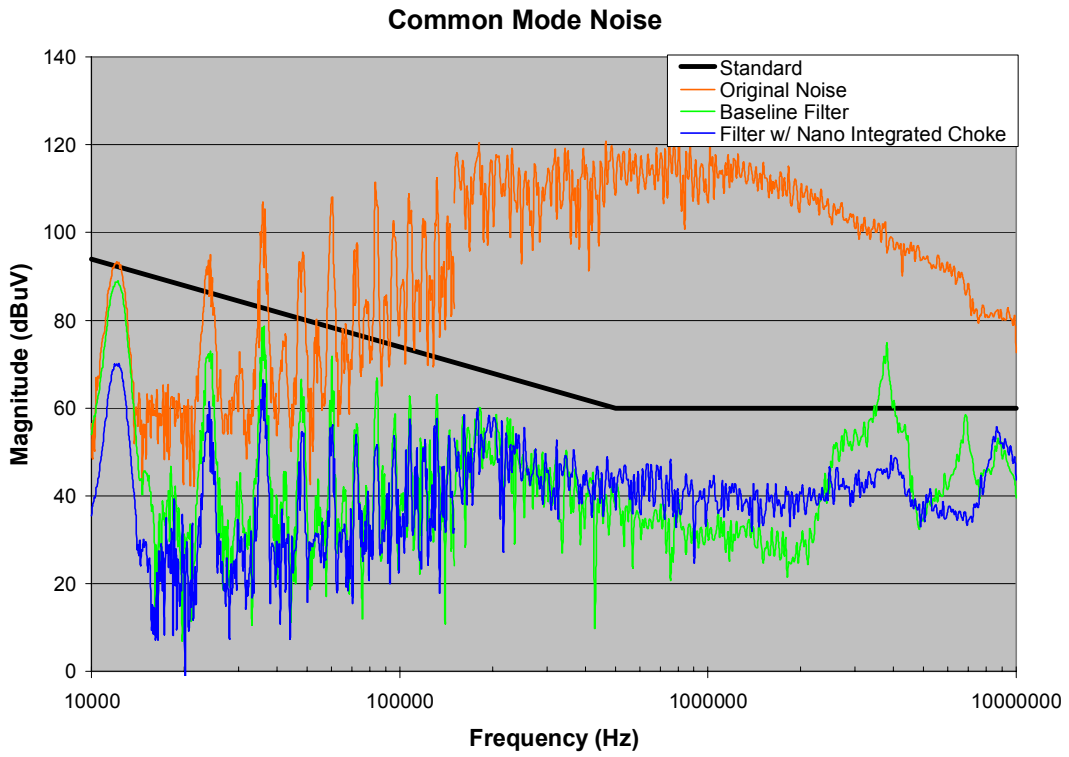


Fig. 5-57: CM noise for baseline and final version of filter

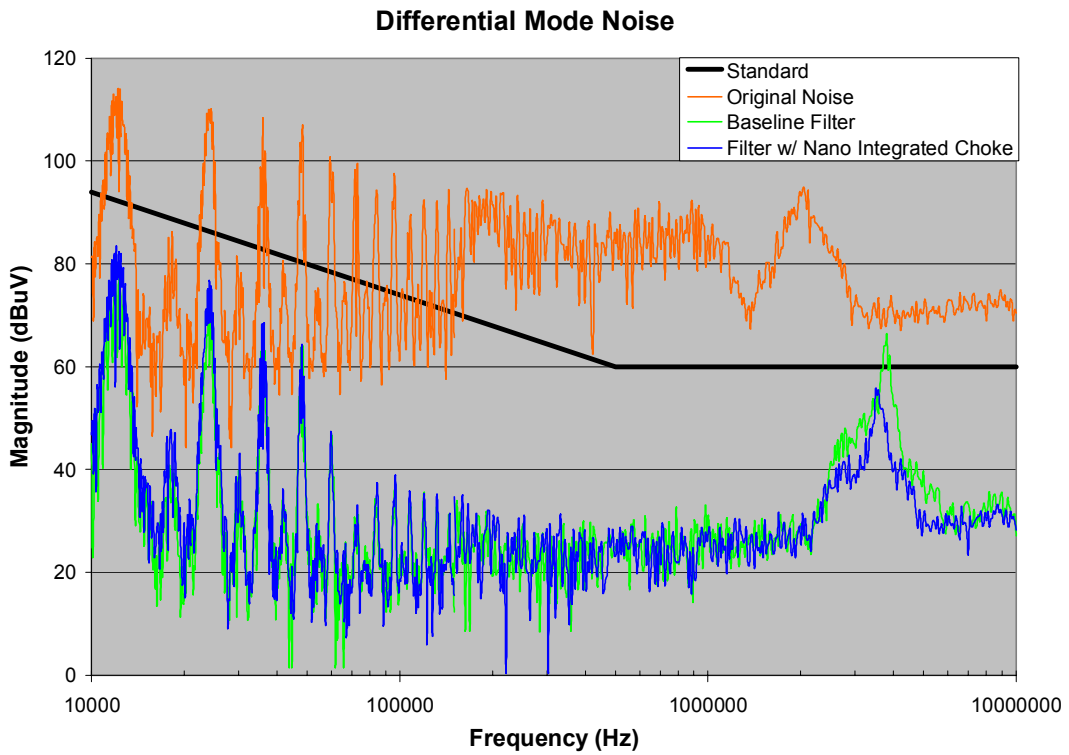


Fig. 5-58: DM noise for baseline and final version of filter

Chapter 6 Summary and Conclusions

The creation of a baseline design has been done successfully following the multiples approaches found in diverse EMI research. It has been used as a starting prototype to understand and analyze EMI problems in large signals measurements. Its main contribution is on the grounding scheme guidelines that have been derived from the tremendous number of tests done. Finally, optimization solution have been suggested and studied to achieve a smaller filter size. Consequently, the final size of the filter has been reduced by three and its performances improved. It has been made possible by the combination of new material technologies and the novel integrated structure proposed in this research. Even though, some other works on discrete integration have been made in the past, this new approach improves the total performances, reduce the size and keep the choke perfectly balance for both modes.

Unfortunately, the strategy to design the discrete EMI filter is proposed based on experimental measurements and tries and errors. As a result, a lot of time has been spent after the design stage to test different topologies and search for the best one. To improve this strategy a complete modeling of the system, including the input impedance of the motor drive could be done in the future. It will lead to design the filter appropriately and maximize the impedance mismatch theory between the filter and the motor drive. Fewer margins will be therefore considered during the design process since the real attenuation of each mode will be known.

Another really interesting issue that could be analyzed in the future is the relation between small signal and large signal measurements. Many papers only considers small signals tests, however it has been shown that quite often power measurements doesn't reflect the small signal behavior. As an example the work done on EPC has shown an increase of the capacitance value when multi layers winding techniques is used which was impacting considerable the insertion gain. However this tremendous change wasn't impacting the large signals tests at all or very little. From the previous idea, it will also be possible to better understand why the EPC cancellation technique is not working in power tests and what could be the alternatives.

REFERENCES

- [1] C. R. Paul, "Introduction to Electromagnetic Compatibility," New York: Wiley, 1992.
- [2] IEC61000: Electromagnetic Compatibility, 2000
- [3] H. W. Ott, "Noise Reduction Techniques in Electronic Systems," New York: Wiley, 1988.
- [4] X. Huang, "Frequency Domain Conductive Electromagnetic Interference Modeling and Prediction with Parasitics Extraction for Inverters", PhD. Dissertation, Virginia Tech, 2004.
- [5] Q. Liu, "Modular Approach for Characterization and Modeling Conducted EMI Emissions in Power Converters", PhD. Dissertation, Virginia Tech, 2005.
- [6] A. L. Julian, G. Oriti and T. A. Lipo, "Elimination of Common-Mode Voltage in Three Phase Sinusoidal Power Converters," in *IEEE Trans.*, vol. 14, pp 982-989, Sept 1999.
- [7] S. Ogasawara, H. Ayano and H. Akagi, "Measurement and Reduction of EMI Radiated by a PWM Inverter-Fed AC Motor Drive System," in *IEEE Trans*, vol. 33, pp 1019-1026, July-Aug 1997.
- [8] G. Grandi, D. Casadei and U. Reggiani, "Analysis of Common and Differential Mode HF current Components in PWM Inverter-Fed AC Motors" in *PESC '98*, vol. 2, pp 1146-1151, May 1998
- [9] X. Pei, K. Zhang, Y. Kang and J. Chen, "Analytical Estimation of Common Mode Conducted EMI in PWM Inverter" in *INTELEC '04*, pp 569-574, Sept 2004.
- [10] S. Chen, "Generation and Suppression of Conducted EMI from Inverter-Fed Motor Drives" in *IEEE Ind. App. Conf.*, vol. 3, pp 1583-1589, Oct 1999.

- [11] M. Mutoh, M. Kanesaki, J. Nakashima and M. Ogata, "A New Method to Control Common Mode Currents Focusing on Common Mode Current Paths Produced in Motor Drive Systems" in *IAS '03*, vol. 1, pp 459-466, Oct 2003.
- [12] R. Chen, S. Wang, J. D. van Wyk, and W. G. Odendaal, "Integrated of EMI Filter for Distributed Power System (DPS) Front-end Converter," in *IEEE Trans*, pp. 296–300, Sept 1998.
- [13] S. Ogasawara, H. Ayano and H. Akagi, "An Active Circuit for Cancellation of Common-Mode Voltage Generated by a PWM Inverter," in *IEEE Trans*, vol. 13, pp. 835–841, Sept 1998.
- [14] S. Ogasawara and H. Akagi, "Suppression of Common Mode Voltage in a PWM Rectifier/Inverter System," in *IAS '01*, vol. 3, pp. 2015–2021, Oct 2001.
- [15] Y. C. Son and S. K. Sul, "A New Common-Mode EMI Filter for PWM Inverter," in *IEEE Trans.*, vol. 18, pp. 1309–1314, Nov 2003.
- [16] W. Chen, X. Yang and Z. Wang, "An Active EMI Filtering Technique for Improving Passive Filter Low Frequency Performance," in *IEEE Trans*, vol. 48, pp. 172–177, Feb 2006.
- [17] A. Carrubba, M. C. Di Piazza, G. Tinè and G. Vitale, "Design and Experimental Implementation Issues for Common Mode Compensation Devices in PWM Induction Motor Drives," in *ISIE '07*, pp. 588–593, June 2007.
- [18] S. Wang, Y. Maillet, F. Wang and D. Boroyevich, "Hybrid EMI Filter Design for Common Mode EMI Suppression in A Motor Drive System," in *IEEE Trans, PESC 2008*.
- [19] L. H. Kim, H. K. Yun, C. Y. Won, Y. R. Kim and G. S. Choi, "Output Filter Design for Conducted EMI Reduction of PWM Inverter-fed Induction Motor System," in *IEEE Proc. '01*, vol. 1, pp 252-258, Oct 2001.
- [20] C. Choochuan, "A Survey of Output Filter Topology to Minimize the Impact of PWM Inverter Waveforms on Three-Phase AC Induction Motors," in *IPEC '05*, pp 1-6, Dec 2005.

- [21] N. Hanigovszki, J. Landkildehus, G. Spiazzi and F. Blaabjerg, "An EMC Evaluation of the Use of Unshielded Motor Cables in AC Adjustable Speed Drive Applications," in *IEEE Trans.*, vol. 21, pp 273-281, Jan 2006.
- [22] F. Shih, D. Chen, Y. Wu, and Y. Chen, "A Procedure for Designing EMI Filters for AC Line Applications", in *IEEE Trans*, vol. 11, pp 170 - 181, Jan. 1996.
- [23] K. Gulez, N. Mutoh, F. Harashima, and K. Ohnishi, "An Approximation to EMI Noise Problem to Design an Appropriate EMI Filter for Induction Motor Control Systems", in *SICE Proc. '01*, pp 6 - 11, July 2001.
- [24] R. West, Magnetics®, Divison of Spang & Co., Butler and Pennsylvania "Common Mode Inductors for EMI Filters Require Careful Attention to Core Material Selection," in *PCIM magazine*, July 1995.
- [25] P. Boonma, V. Tarateeraseth, and W. Khan-ngern, "A New Technique of Integrated EMI Inductor Using Optimizing Inductor-volume Approach," in *IPEC'05*
- [26] L. Nan, and Y. Yugang, "A Common Mode and Differential Mode Integrated EMI Filter", in *IEEE Trans IP EMC'06*, vol. 1, pp 1 - 5, Aug 2006.
- [27] M. Nave, "A Novel Differential Mode Rejection Network for Conducted Emissions Diagnostics", in *IEEE National Symposium*, pp 223 - 227, May 1989
- [28] S. Wang, "Characterization and Cancellation of High-Frequency Parasitics for EMI Filters and Noise Separators in Power Electronics Applications", PhD. Dissertation, Virginia Tech, 2005.
- [29] S. Wang, F. Lee, and W. Odendaal, "Characterization, Evaluation, and Design of Noise Separator for Conducted EMI Noise Diagnosis", in *IEEE Trans*, vol. 20, pp 974 - 982, July 2005
- [30] RTCA, Inc., "Environmental Condition and Test Procedure for Airborne Equipment" in *DO-160D*, Dec 2004.
- [31] Department of Defense, "Requirement for the Control of Electromagnetic Interference Characteristics of Subsystems and Equipment" in *Military Standard 461E*, Aug 1999.

- [32] Department of Defense, "Aircraft Electric Power Characteristics" in *Military Standard 704F*, March 2004.
- [33] The Engineering Society for Advancing Mobility Land Sea Air and Space, "Aerospace Standard," in SAE AS 1831, Oct 1997.
- [34] ETS-LINDGREN®, "Model 91550 Series", in *Current Probes Manual, Feb 2005, Available:*
" <http://www.ets-lindgren.com/manuals/91550-1.pdf>"
- [35] G. L. Skibinski, R. J. Kerkman and D. Schlegel, "EMI Emissions of Modern PWM AC Drives," in *IEEE Ind. App. Magazine*, vol. 5, pp 47-80, Nov-Dec 1999.
- [36] M. Mutoh, M. Kanasaki, J. Nakashima and M. Ogata, "A New Method to Control Common Mode Currents Focusing on Common Mode Current Paths Produced in Motor Drive Systems" in *IAS '03*, vol. 1, pp 459-466, Oct 2003.
- [37] I. Cardirci, B. Saka and Y. Eristiren, "Practical EMI Filter Design Procedure for High Power High Frequency SMPS According to MIL-STD 461", in *IEE Proc. '05*, vol. 152, pp 775-782, July 2005.
- [38] Magnetics®, "High Permeability J Material", in *MAGNETICS Ferrite Core Design Manual and Catalog, Available:*
" http://www.mag-inc.com/pdf/Ferrites/2006_Materials_J.pdf"
- [39] Magnetics®, "Kool Mu Technical Bulletin", in *MAGNETICS Kool Mu Powder Cores Application Notes, Available:*
" <http://www.mag-inc.com/pdf/kmc-s1.pdf>"
- [40] AMC®, "Switch Mode Ceramic Capacitors", in *AMC data sheet, Available:*
" http://www.amccaps.com/products/smc/AMC_Switch-Mode_2005-11.pdf"
- [41] L. Dehong, and J. Jianguo, "High Frequency Model of Common Mode Inductor for EMI Analysis Based on Measurements," in *IEEE EMC 3rd International Symposium '02*, pp 462-465, May 2002.

- [42] S. Wang, Y. Maillet, F. Wang, R. Lai, R. Burgos and F. Luo, "Investigating EMI Filter's Grounding of EMI Filters in Power Electronics Systems," in *IEEE Trans, PESC 2008*.
- [43] A. Makino, T. Hatanai, Y. Naitoh and T. Bitoh, "Application of Nanocrystalline Soft Magnetic Fe-M-B Alloys 'NANOPERM®'," in *IEEE Trans*, vol. 33, pp 3793-3798, Sept 1997.
- [44] Metglas®, "FINEMET® Common Mode Choke Cores", in *Technical Bulletin, 2004, Available:*
"<http://www.metglas.com/downloads/finemet/FMCMC190804.pdf>"
- [45] M. Nave, "On Modeling the Common Mode Inductor", in *IEEE Trans*, pp 452 - 457, Aug 1991.
- [46] A. Massarini and M. K. Kazimierczuk, "Self-Capacitance of Inductors," in *IEEE Trans*, pp 671-676, July 1997.
- [47] S. Wang, F. C. Lee and J. D. V. Wyk, "Design of Inductor Winding Capacitance Cancellation for EMI Suppression," in *IEEE Trans*, vol. 21, pp 1825-1832, Nov 2006.
- [48] T. C. Neugebauer, and D. J. Perreault, "Parasitic Capacitance Cancellation in Filter Inductors," in *IEEE Trans*, vol. 21, pp 282-288, Jan 2006.
- [49] H. Hemphill and B. Wallertz, "Critical Core Parameters in the Design of Common Mode Supression Chokes," in *IEEE Trans*, pp 334-336, Dec 1995.
- [50] Shuo Wang, J. D. van Wyk, Fred C. Lee and W. G. Odendaal, "Transformation between Common Mode and Differential Mode due to Imperfect Balance of EMI Filters," proc. of 2005 CPES Power Electronics Conference, Blacksburg, VA, pp. 551 – 555, April 2005.